Experimental and Theoretical Investigation of Indium Phosphide Quantum Dot Growth Mechanisms

by

Lisi Xie

B.E. in Chemical Engineering, Tsinghua University, 2011
M.S. Chemical Engineering Practice, Massachusetts Institute of Technology, 2014

Submitted to the Department of Chemical Engineering
in Partial Fulfillment of the Requirements for the Degree of

Doctor of Philosophy in Chemical Engineering

at the

MASSACHUSETTS INSTITUTE OF TECHNOLOGY

September 2016

Author..... Signature redacted
Department of Chemical Engineering
August 29, 2016

Certified by..... Signature redacted .....
Klavs F. Jensen
Warren K. Lewis Professor of Chemical Engineering
Professor of Materials Science and Engineering
Thesis Supervisor

Certified by..... Signature redacted
Heather J. Kulik
Joseph R. Mares '24 Career Development Professor of Chemical Engineering
Thesis Supervisor

Accepted by..... Signature redacted .....
Daniel Blankschtein
Herman P. Meissner (1929) Professor of Chemical Engineering, Graduate Officer
Committee for Graduate Students

Experimental and Theoretical Investigation of Indium Phosphide Quantum Dot Growth Mechanisms

by

Lisi Xie

Submitted to the Department of Chemical Engineering
on August 29, 2016, in Partial Fulfillment of the
Requirement for the Degree of
Doctor of Philosophy in Chemical Engineering

Abstract

Indium phosphide (InP) quantum dots (QDs) stand out as the most promising candidate to replace the currently commercialized cadmium-containing materials for optoelectronic applications. This thesis focuses on using experimental and theoretical methods to study growth mechanisms of InP QDs from precursor conversion to final nanocrystal formation. As the key experimental platform, a high temperature and high pressure microfluidic system was first applied to study the effect of group V precursor reactivity on the QD growth. High-pressure flow conditions allow for precise control of synthetic parameters and also the use of low-boiling-point solvents for synthesis with enhanced mixing. Results showed that lowering the precursor reactivity did not significantly improve the QD quality, contradicting the original hypothesis. The unexpected role of precursor chemistry motivated investigation into the early-stage QD growth mechanisms. First-principles approaches were used without any prior assumptions on reaction pathways. Simulations showed that small clusters with indium-rich surfaces form in the early-stage QD growth. In and P precursors have different roles, with P precursors controlling the reaction energy, and In precursors determining the reaction barrier. With clusters identified as important growth intermediates in both simulations and experiments, their role during the QD formation was then investigated with a one-solvent protocol, which combined flow synthesis, GPC purification and MALDI mass characterization. Experiments revealed that similar clusters exist during the late-stage nanocrystal growth, suggesting their role as a continuous supply for the QD formation. Lastly, a QD size tuning strategy was developed involving the use of weakly associated ligands to synthesize cluster-free InP QDs with different sizes and narrow size distributions. This synthetic approach enabled the construction of a correlation between the absorption features and the mass and concentration of InP QDs. The importance of In precursor quality became apparent after exploring effects of impurities and solvents. For example, when water and hydroxide/oxide species contaminate In precursors, the growth of InP QDs are inhibited and batch-to-batch variations are observed.

Thesis Supervisor: Klavs F. Jensen
Title: Warren K. Lewis Professor of Chemical Engineering
Professor of Materials Science and Engineering
Thesis Supervisor: Heather J. Kulik
Title: Joseph R. Mares '24 Career Development Professor of Chemical Engineering

Acknowledgements

I have been very lucky to be cared, helped and guided during my whole PhD career. My thesis advisors, Professor Klavs Jensen and Professor Heather Kulik, have been very supportive, encouraging and inspiring. Klavs has given me the most opportunity I could imagine to have as a graduate student in exploring research. No matter how busy, he is always there to help. Although I joined Heather's lab in the middle of my PhD, I am impressed by her intelligence, diligence, and high standards on science. I am grateful to have Klavs and Heather as my advisors and their different mentoring styles truly benefit my professional growth. Professor Moungi Bawendi and Professor William Green have been great thesis committee members. Not only do they provide constructive advices during my committee meetings, but also they are willing to share their lab resources and help me whenever I need.

I want to thank the following funding resources that supported my study in MIT. In the first year, I was funded through the Robert T. Haslam ('11) ChemE Fellowship (2011). In the second and third years, my funding was from the US ARO through the Institute for Soldier Nanotechnologies (W911NF-13-D-0001). In the last two years of my PhD, my research was supported by the National Science Foundation under grant number ECCS-1449291. Part of the simulation work was carried out using computational resources from the Extreme Science and Engineering Discovery Environment (XSEDE), which was supported by National Science Foundation grant number ACI-1053575. Part of the simulation work was also carried out in part using the computational resources of the Center for Nanoscale Materials (Carbon cluster), an Office of Science user facility, was supported by the U. S. Department of Energy, Office of Science, Office of Basic Energy Sciences, under Contract No. DE-AC02-06CH11357.

It has been a great time to work with the past and current lab members in Jensen Lab. Jinyoung Beak helped me start my PhD in the group. He gave me a thorough training on how to assemble reactors, how to use a glove box and perform QD synthesis. I have benefited a lot from these trainings. Although Yi Shen joined the lab in the last year of my PhD, we had a great time working on the MALDI project. His passion and curiosity towards science have also inspired me. I have learned a lot from Andrea Adamo in fabricating tube reactors and being a good engineer, from Stephen Newman in thinking critically and positively about scientific problems, from Everret O'Neal in working efficiently and creatively, from Hongkun Lin in how to do experiments as a true chemist, and from Andrew Teixeira in rebuilding oil pumps and solving technical problems. Tatyana Shatova, Brandon Reizman, Yanjie Zhang, Baris Unal, Milad Abolhasani, Maud Fevre, Gaurav Giri, Saurabh Shahane, Nopphon Weeranoppanant, Yanxiang Shi, Stephen Born, Ulrich Neuenschwander, Lu Yang, Patrick Heider, Kosi Aroh, Cuixian Yang, Kyoungmi Lee, Yiming Mo, Haomiao Zhang, Kai Wang, and Jisong Zhang are all great lab members to share everyday with. The past two years in Kulik lab has also been a fun time. Qing Zhao helped me make better figures and slides. Tim Ioannidis, Helena Qi and Niladri Napa kindly helped me improving my coding and debugging skills.

My collaborators, Daniel Harris and Daniel Franke from the Bawendi Lab, have provided me a lot of insights in understanding III-V QD growth. Conversations with Daniel Harris are encouraging and inspiring. Discussions with Ou Chen are always helpful in improving my understanding about QDs in general. I am also thankful to other Bawendi Group members

including Whitney Hess, Yue Chen, Jennifer Scherer, and Darcy Wanger for sharing their experimental experiences on QDs.

A lot of MIT staff members have also helped me during my experiments. Alla Leshinsky and Richard Cook from MIT Koch Institute helped with the MALDI measurement, Gang Liu from the Department of Chemistry helped me solve electric problems with pumps and ovens, and Li Li from Department of Chemistry Instrument Facilities helped me with the ESI measurement. Other colleagues from various labs also showed their great kindness. Kurt Armbrust from Jamison Lab helped me with Karl-Fisher measurement. Mark Simon from Pentelute Lab improved my understanding on MALDI. Maggie He from Swager Lab and Bing Yan from Surendranath Group helped me with the XPS measurement. Strano Lab members have kindly offered their UV-Vis spectrometer for me to use.

Being a teaching assistant for Professor Bradley Olsen and Professor James Swan has also been a great experience. I have also learned a lot from my teammates, mentors and sponsors during the Practice School program. Our departmental administrative assistants, Alina Haverty, Gwen Wilcox, Suzanne Maguire, Sharece Corner, Sydney Greenley-Kois, Joel Dashnaw and Fran Miles, are all nice and sweet. I also gained help from MIT writing center in revising manuscripts and this thesis. Zachary Buras, Yuqing Cui, Shengchang Tang, Yurang Wang and Rong Yang have also helped me improve my presentation and written skills.

Last but not least, I want to thank my talented and brilliant friends here who inspire and motivate me to excel myself and become a better person. I also want to thank my family and friends abroad for their long-lasting love and support. My parents have accompanied me through every important moment of my life, also including this one. No matter how old I become or how far I go, I could never learn enough from them of being a humble, sincere and optimistic person.

Contents

List of Figures

List of Tables

Chapter 1

Introduction

1.1 Quantum Dots (QDs)

Colloidal semiconductor nanocrystals, also known as quantum dots (QDs), have attracted significant attention since their discovery in the early 1980s.[1-4] Different from the bare nanocrystals epitaxially grown in the gas phase, solution-synthesized QDs consist of two parts (Figure 1-1 A): (1) the inorganic cores that are single-crystalline or poly-crystalline with diameters between 2 and 20 nm, and (2) the capping ligands that stabilize the inorganic cores from aggregating in solution. In bulk semiconductors, the energy states in the conduction and valence bands are continuous and the electron-hole pairs (excitons) have a characteristic distance called the exciton Bohr radius. As the physical size of QDs is on the order or smaller than this radius, the energy states become quantized and the band gap energy increases (Figure 1-1 B). The smaller the size of the QDs, the more confined the excitons and the higher the band gap energy. This quantum confinement effect endows QDs with size and shape dependent optical and electronic properties. For example, with the size decrease of cadmium selenide (CdSe) QDs, their band gap increases and their first absorption peak shifts from near infrared to UV range (Figure 1-2). Besides CdSe QDs, synthetically available QDs include group II-VI, IV-VI, I-III-VI, and III-V semiconductors with different shapes and structures. Table 1-1 lists example QDs with their corresponding bulk properties and synthetically available first absorption peaks.

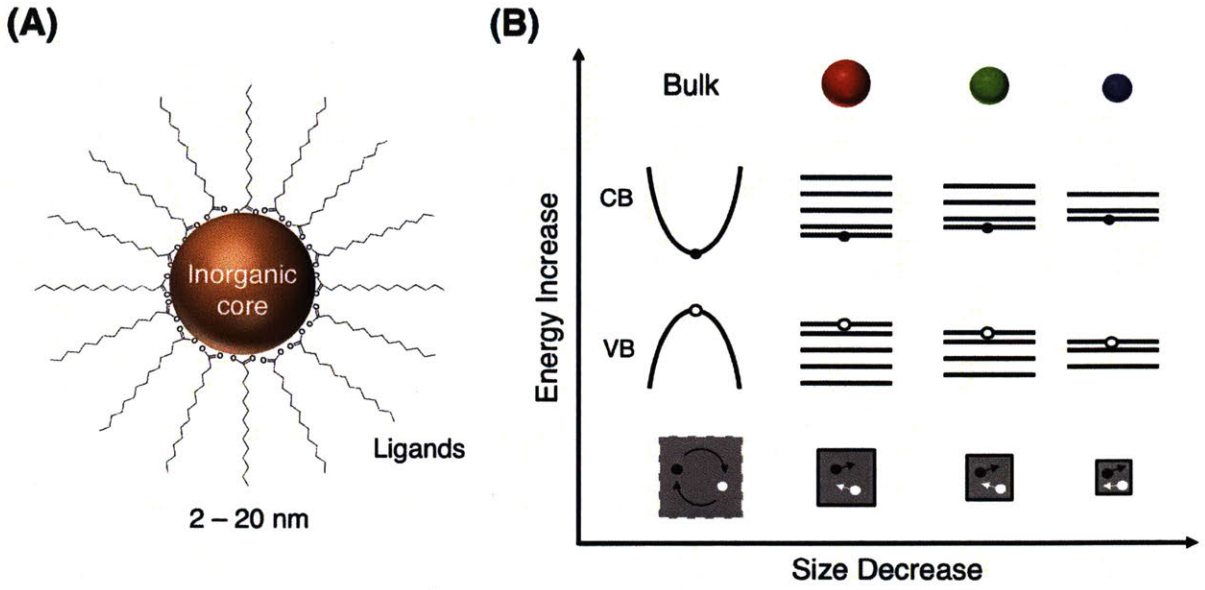

Figure 1-1: Schematic illustration of (A) quantum dots and (B) quantum confinement effects.

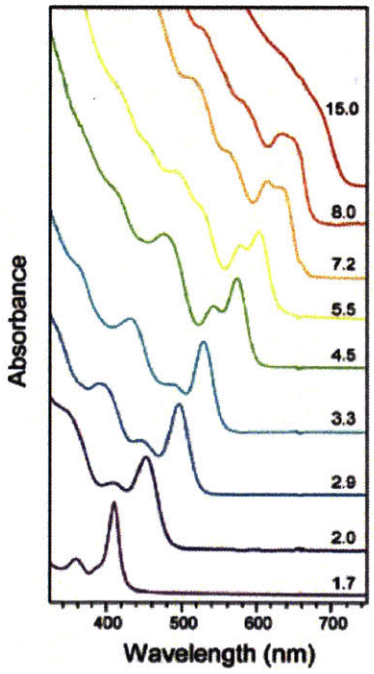

Figure 1-2: Absorbance spectra of CdSe QDs with different sizes in diameter (nm); adapted from Murray, C.B., Ph.D. Thesis, MIT, Cambridge, MA, 1995.

Table 1-1: Bulk band gap and the exciton Bohr radius for common QD materials, as well as their synthetically available range of the first absorption peaks.

QDs	Group	Bulk band gap (eV)	Bohr radius (nm)	First absorption peaks (nm)
InP	III-V	1.34	9.5	400-700[5]
InAs	III-V	0.36	34	700-1300[6]
CdSe	II-VI	1.73	5.4	400-700[7]
PbSe	IV-VI	0.27	46	1100-2100[8]
PbS	IV-VI	0.37	20	800-1800[9-10]

QDs have applications ranging from optoelectronics[11] and photovoltaics[12] to biological imaging[13]. For example, II-VI cadmium selenide (CdSe) derived QDs have been commercialized as lighting and display materials due to their narrow emission spectra and high color saturation.[14] They can also be used as fluorescent tags in biological systems due to their great chemical and photo stability and their bright emission.[13] IV-VI lead chalcogenide QDs are implemented in photodetectors and photovoltaics due to their size-tunable infrared band gap and their ability to generate multiple excitons, potentially enhancing the efficiency of solar cells.[12] Compared to their cadmium or lead counterparts, III-V group QDs have reduced environmental and biological toxicity and thus are under intensive investigation. Among III-V materials, indium phosphide (InP) and indium arsenide (InAs) QDs have been synthesized in a relatively monodisperse and well-crystallized form. Due to the same visible tunable optical properties, InP QDs are considered as a replacement for the commercialized CdSe products.[15] InAs QDs are promising materials for *in vitro* and *in vivo* imaging due to the high transmission of their fluorescence through tissue in the near infrared range.[16]

1.2 Synthetic Development of III-V QDs

The size, size distribution, crystallinity and stability of QDs directly affect their optical and electronic properties, such as their absorption and emission peak locations, peak line widths and photoluminescence quantum yields. Therefore, the performance of QDs is closely related to their growth process. Initial methods to grow colloidal III-V QDs are based on Wells' dehalosilylation reaction[17-18], where indium and gallium halides (or their modified forms) react with tris(trimethylsilyl)phosphine ($P(TMSi)_3$) or tris(trimethylsilyl)arsine ($As(TMSi)_3$) with trioctylphosphine (TOP) and/or trioctylphosphide oxide (TOPO) as solvents and ligands.[6, 19-23] This method requires a long growth time (up to days) at high growth temperatures (up to 300 °C), and further size-selective precipitation is required to narrow the nanocrystal size distribution. A breakthrough in the III-V QD growth was achieved by Peng and co-workers in 2002.[24] They proposed to use a non-coordinating solvent, 1-octadecene (1-ODE), and indium carboxylates to synthesize InP and InAs QDs. This approach greatly reduces the growth time and improves the size distribution of InP and InAs QDs. Today, nearly all $P(TMSi)_3$-based InP QD syntheses utilize this indium carboxylate approach with the growth tuned by different surfactants such as carboxylic acids, amines and alkylphosphines.[5, 25-30] Both indium halide and indium carboxylate approaches are used to synthesize InAs-based QDs.[31-35] Recently, an alternative approach to synthesizing InP QDs has been proposed, with tris(dimethylamino)phosphine ($P(N(Me)_2)_3$) as the phosphorus precursor.[36-37] Primary amines are required reagents for the nanocrystal formation, and both the precursor conversion mechanisms and nanocrystal surface chemistries have been investigated.[38-39] A similar strategy of using arsenic silylamide ($As(N(Me)_2)_2Cl$) to produce InAs QDs has also been demonstrated.[40] Table 1-2 summarizes the

methods to synthesize III-V QDs. This thesis is focusing on improving the understanding of InP QD growth with the indium carboxylate chemistry.

Table 1-2: Current colloidal synthetic approaches for III-V QDs

QDs	Precursors	Solvents, surfactants	Conditions
InP	$InCl_3$, $P(TMSi)_3$	TOP, TOPO	Several days, 270 – 300 °C[20-23]
	$In(RCOO)_3$, $P(TMSi)_3$	ODE, RCOOH, TOP, RNH_2	10 – 60 min, 180 – 300 °C[5,25-30]
	$InCl_3$, $P(N(Me)_2)_3$	RNH_2	10 – 60 min, 180 – 270 °C[36-37]
InAs	$InCl_3$, $As(TMSi)_3$	TOP	Several days, 250 – 300 °C[6,31-32,35]
	$In(RCOO)_3$, $As(TMSi)_3$	1-ODE, TOP	10 – 60 min, 130 – 300 °C[24,33-34,41]
	Indium salts, $As(N(Me)_2)_2Cl$	1-ODE, RNH_2, reducing $LiEt_3BH$	30 – 35 min, 250 °C[40]

1.3 Growth Behavior of III-V QDs

While highly crystalline II-VI group QDs have been grown with wide size tunability, narrow size distribution, and near-unity quantum yield, the quality of III-V materials has lagged behind. For example, the narrowest emission line widths (full width at half maxima) for CdSe-derived QDs are routinely below 30 nm[42], while for InP-derived QDs that are emitting in the same range, their line widths are around or more than 50 nm.[26,28-29] InAs-derived QDs have an even wider size distribution than their InP ananologs.[34,41] However, a similar single particle line width is characterized for CdSe, InP and InAs derived QDs, suggesting the ensemble inhomogeneity as the main reason for the broader line widths of III-V QDs.[43] This quality difference is explained by the different growth behaviors of II-VI and III-V QDs, which are hypothesized to depend on the bonding covalency, precursor reactivity and synthetic conditions.

The first hypothesis relies on the bonding differences between II-VI and III-V QDs.[44] For II-VI QDs, bare ions or atoms directly react with each other at high temperatures via rapid injection of one reagent into another. Particle nucleation is initiated immediately upon mixing. After the injection of precursors, the temperature of the reaction mixture drops, thereby stopping the nucleation and allowing for particle growth at relatively low temperatures. This synthetic scheme, also known as "hot injection" method, helps produce narrow size distribution of II-VI QDs.[45] However, for III-V QDs, direct adaptation of this method becomes difficult due to the more covalent nature of the chemical bonds in III-V compounds, as both the nucleation and growth require high temperatures and long reaction times. These synthetic conditions can greatly broaden the size distribution of III-V QDs.

The second hypothesis attributes the quality difference to the high reactivity of precursors. The more covalent III-V bonds require the use of highly reactive $P(TMSi)_3$ and $As(TMSi)_3$ as precursors. Even though their reactions with indium carboxylates greatly improve the size distribution of III-V QDs, their quality is still not comparable to that of II-VI CdSe QDs. A growth mechanism study by Allen and co-workers showed that the syntheses of InP QDs from indium carboxylates and $P(TMSi)_3$ are based on non-molecular growth processes in which the precursors are depleted at the early stage of growth, while the remaining nanoparticle formation is governed by ripening or coalescence mechanisms.[46] This growth behavior differs from that of II-VI QDs, where an initial nucleation of colloids occurs first, followed by subsequent growth of the nuclei from molecular precursors (Figure 1-3). This phenomenon possibly explains the poor quality of III-V QDs compared to II-VI QDs.

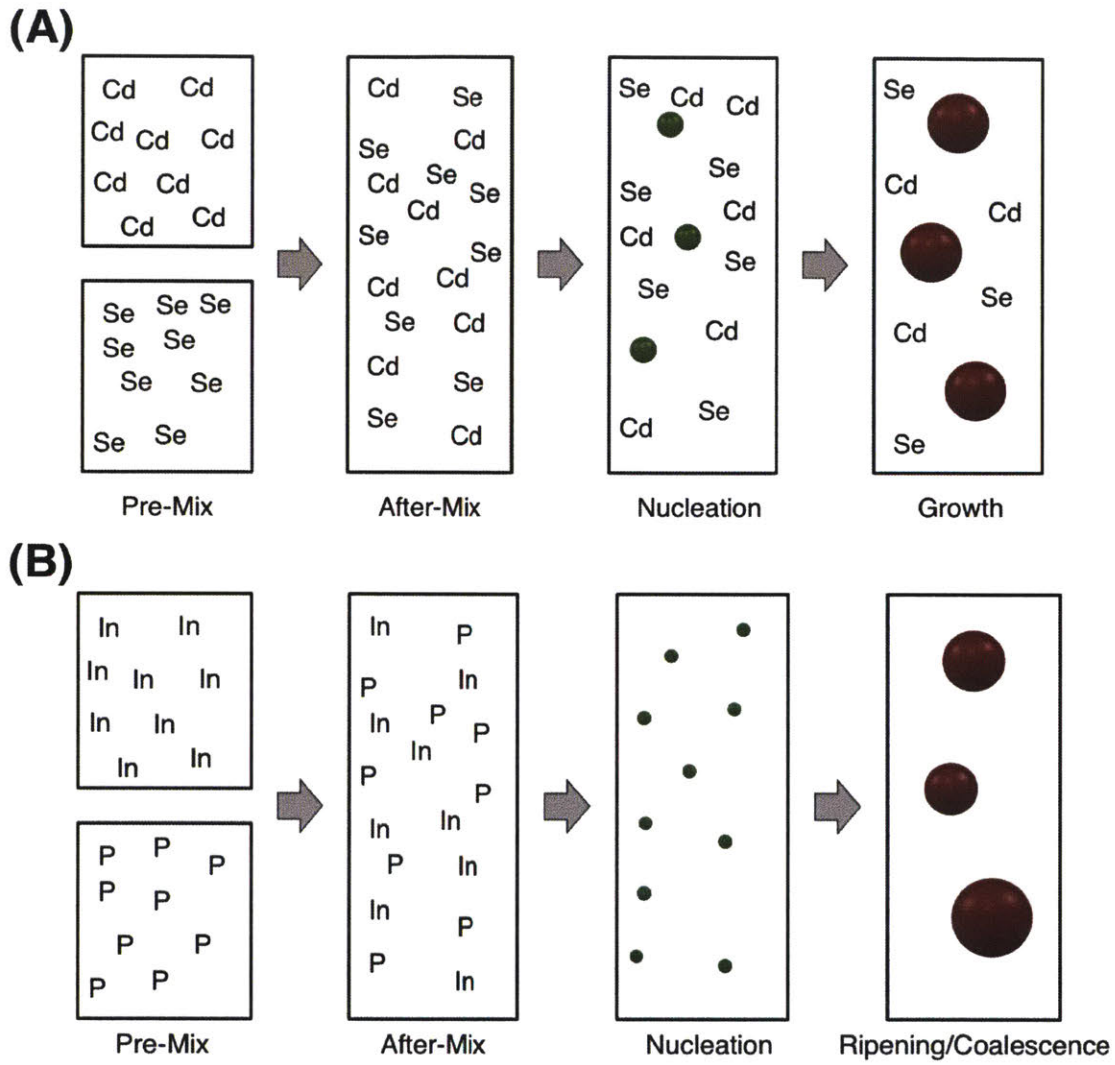

Figure 1-3: Proposed growth models of (A) CdSe and (B) InP QDs based on the studies of Allen and coworkers. [46]

The last hypothesis considers the fact that the synthetic conditions for III-V QDs may not be optimal. Current synthetic conditions for III-V QDs are directly adapted or modified from those of II-VI QDs, such as the use of hot injection methods. Since II-VI and III-V QDs undergo different growth behaviors, their optimal synthetic schemes may also vary from each other. For example, two-stage syntheses are developed to produce InP QDs with improved size distribution[41,47], where precursors are mixed at low temperatures and then brought up rapidly to

elevated temperatures. For InAs QDs, it was also observed that conducting the self-focusing process at an elevated temperature, after nucleation, could result in InAs QDs with well-controlled size and size distribution.[48] Not only could the heating scheme affect the growth, but also the syntheses of InP QDs were found to depend largely on the fatty acids chosen, the solvents in use and the indium-to-ligand ratio. Side reactions, such as those between phosphorus precursors and proton impurities[49], the thermal decomposition of carboxylic acids to produce water[50], and the surface oxide formation induced by amines[51], all serve as important factors affecting the quality of InP QDs.

1.3.1 Comparison between InP and InAs QDs

To improve the quality of InP and InAs QDs, such as their size tunability and size distribution, significant efforts have been devoted to investigating their growth mechanisms. Most of these studies utilize InP QDs as the model system, possibly due to the less reactive nature of phosphorus precursors compared to arsenic precursors and the relative air stability of InP QDs compared to InAs QDs. Moreover, since InP-derived QDs are progressing into the market as a Cd-free replacement for display applications, improving their quality can have an immediate economic impact and is thus attracting much attention.

The similar covalency between In-P and In-As bonds leads to similar precursor chemistry and growth conditions utilized for the syntheses of InP and InAs QDs. For the most often applied indium carboxylate chemistry, despite the same fast precursor conversion kinetics and high air sensitivity for both QDs, their syntheses differ from each other in the following aspects: first, it is more challenging to tune the size of InAs QDs at similar growth conditions.[52] While InP QDs can be synthesized with sizes around 3-4 nm, InAs QDs with sizes around 1-2 nm are obtained. Second, InP QDs are characterized by nearly zero photoluminescence quantum yields, while

InAs QDs have detectable emission features. Third, InP QD growth can be effectively tuned by adding excess carboxylic acids, possibly through their etching effect, while InAs QD growth is independent of acids.[53] These observations point out that although the syntheses and growth behaviors of InP and InAs QDs are similar, their reaction pathways and surface chemistries may be different. Special caution is needed before extrapolating the growth mechanisms of InP QDs to those of InAs QDs.

1.4 Methods to Study III-V QD Growth

1.4.1 Experimental Characterization

The growth of III-V QDs can be characterized via different experimental techniques. Transmission electron microscopy (TEM) and X-ray power diffraction (XRD) methods are applied to provide direct physical information about QDs such as their size, size distribution, lattice type and crystallinity. Absorbance and photoluminescence measurements are typical spectroscopy methods to characterize the growth behaviors of III-V QDs due to their size-dependent optical properties. These methods can also be incorporated *in situ* to improve our understanding of the QD formation kinetics. For example, Harris et al. probed the formation rates of InP/InAs bonds using *in situ* absorbance measurement at 310 nm in batch syntheses.[41] By assuming that the extinction coefficients scale linearly with the effective nanoparticle volumes in the UV range, they correlated the absorbance measurement to the early-stage nanocrystal formation kinetics. They have quantified the reactivity of different group V precursors using this method.

To better integrate these *in situ* characterization methods to monitor the growth of III-V QDs, novel reactor platforms (as compared to traditional batch syntheses) have been developed.

Nightingale et al. integrated a flow cell downstream of their capillary and Y-shaped microfluidic devices in order to monitor *in situ* the emission spectra of InP-derived QDs at different growth times, temperatures and precursor concentrations.[54] Similarly, Baek et al. integrated a flow cell at the outlet of their high temperature and high pressure chip reactors to record both the absorbance and emission spectra of III-V QDs and their core-shell structures.[53, 55] Recently, a droplet oscillating flow reactor has been developed to record the inline absorption of InP QDs with millisecond resolution.[56]

Besides these direct growth studies, other spectroscopy methods that are typically used for the characterization of molecular species or solid state materials have also been adapted to study the III-V QD synthetic chemistries. For example, nuclear magnetic resonance spectroscopy (NMR) has been applied to characterize the side reactions between the phosphorus precursors and excess acids used in the syntheses, which are hypothesized to broaden the size distribution.[49] X-ray photoelectron spectroscopy (XPS) has been implemented to characterize the surfaces/interfaces of InP-derived QDs to show that the nanoparticle surfaces/interfaces contain a mixture of oxide and hydroxide species.[50, 57] The existence of the surface oxides raises concerns about water contamination during the synthesis, and also possibly explains the current challenge in obtaining highly luminescent thick-shell InP core-shell nanostructures.

1.4.2 Theoretical Modeling

Along with experimental investigation, theoretical modeling has also been applied to understand the growth of QDs. First-principles calculations have provided molecular-level insights into the growth of the synthetically better-established II-VI and IV-VI QDs, specifically related to their precursor chemistry, structure-property relation as well as their ligand-dependent anisotropic growth mechanisms. For example, Eichkorn and co-workers computed the structure,

electronic excitations and electron affinities of small ligand-stabilized CdSe clusters by DFT calculations.[58] Jose and co-workers studied the structural evolution of CdSe clusters using experimental results and first-principles calculations.[59] By calculating the size and absorption spectra of CdSe clusters, they identified possible structures that match their experimental results. To validate the hypothesis that the anisotropic growth of CdSe nanocrystals is controlled by ligand binding energies, which affect the relative growth rates of different facets, DFT calculations have also been applied to study the ligand effects on the nanocrystal growth.[60-61] While III-V QDs have not been the subject of as much computational study, other III-V materials such as nanowires[62], nanotubes[63], hetero-structures[64] and bulk surfaces[65-67] have been investigated with first-principles techniques. Besides quantum chemical simulations, empirical theoretical models have also been developed to describe the QD growth processes. They either refer to the experimental observed size-focusing phenomenon as the criteria to check the model validity or directly use II-VI CdSe QD growth as the model system.[68-71] It should be noted that only first-principle calculations have been used in this thesis to study III-V QD growth.

1.5 Thesis Overview

This thesis has implemented both experimental and theoretical approaches to study the growth of III-V QDs from precursor conversion to final nanocrystal formation. InP QDs are chosen as the model system in most of these studies. The remainder of the thesis is outlined below.

The use of high temperature (HT) and high pressure (HP) microfluidic system to synthesize III-V QDs is discussed in the first part of the thesis. This platform is our key experimental investigation tool. The choice of flow synthesis allows for the precise control of synthetic parameters for mechanistic studies. The *in situ* absorbance measurement allows for fast

monitoring and screening of growth conditions. As an example, a two-stage HT and HP silicon chip reactor system is applied to compare the growth of III-V QDs with different group V precursors. The key finding is that lowering the precursor reactivity does not significantly improve the growth of III-V QDs, contradicting original hypothesis regarding the role of precursory chemistry on III-V QD growth.

The unexpected role of precursor chemistry motivates the theoretical work performed in the second part of the thesis, where early-stage precursor conversion mechanisms are investigated using first principle methods. Due to the challenges in performing experimental studies on the precursor interactions, this theoretical approach serves as an ideal tool for mechanistic discovery without any prior assumptions on reaction pathways. The key finding is that small clusters with indium rich surfaces form during early-stage QD growth. While phosphorus precursors are found to affect the reaction energy, it is the binding mode change of carboxylate ligands towards indium that controls the reaction barrier of the precursor conversion kinetics. Therefore, a combined tuning strategy of both indium and phosphorus precursors is likely necessary to improve the quality of QDs.

Following the investigation on the precursor conversion kinetics, in the third part of the thesis, various experimental techniques are applied to study the growth of InP QDs after precursor conversion. Consistent with the simulation results, absorbance measurement shows that clusters are formed during the early-stage growth in an indium-rich environment. To further investigate the role of clusters during QD formation, an air-free and one-solvent method is developed which allows for: 1) Synthesis of InP QDs in a HT/HP microfluidic reactor, 2) Purification of the resulting samples without precipitation (to avoid surface change), and 3) Simultaneous tracking of the existence of clusters in the presence of large InP nanocrystals via

MALDI-TOF mass spectrometry (MS). The key finding is that similar clusters exist during the late-stage growth of InP QDs under various conditions, suggesting their role as a continuous supply for the formation of larger nanocrystals. Our new protocol also provides opportunities for the characterization and growth study of small-sized air-sensitive clusters or QDs.

Due to the limited success in tuning precursor chemistry, the fourth part of the thesis focuses on utilizing the HT and HP platform to explore the effect of impurities, ligands and solvents on the growth of InP QDs. The effect of trace water contaminant in the commonly used indium precursors is first discussed. It is found that when the water contamination is low, the growth can be effectively tuned by growth temperature and time. However, when the water content reaches above a certain level, the growth presents a "focused" behavior. Similar inhibiting effects are also observed with trace amount of bases. However, as water and bases can poison the nanocrystal surfaces, they are not favorable additives to tune the QD growth. Following the impurity study, the effect of weakly associated ligands is discussed. A strategy of using TOP and TOPO is developed to synthesize cluster-free QDs with different sizes and narrow size distributions. This synthetic approach enables the construction of a correlation between the absorption features and the mass and concentration of InP QDs, which can further guide the controlled syntheses of InP derived core-shell structures. The effect of solvent is discussed last, where low-boiling-point solvents such as octane, toluene, heptane and *o*-xylene are used in the synthesis of high-quality InP QDs.

Chapter 2

A High Temperature and High Pressure Microfluidic Platform

2.1 High Temperature and High Pressure Microfluidic Synthesis

2.1.1 Background

Batch methods have enabled chemists to discover new chemistries and explore complicated approaches to synthesize high-quality QDs. However, batch methods inherently suffer from reproducibility and controllability challenges due to batch-to-batch variations in the injection rates of precursors, the temperature and concentration distribution within the flask, and the cooling rates of the reaction(Figure 2-1). For QD growth studies, reproducible and controllable syntheses are necessary to obtain reliable mechanistic information. Microfluidic systems are well known for their desirable characteristics such as enhanced mass and heat transfer, feedback control, and excellent reproducibility due to continuous steady-state operation, thus overcoming the limitations in batch processes.[72] By carrying out reactions on the micro scale, they also reduce the consumption of raw materials during chemistry screening and optimization. For the synthesis of QDs, which always involves the use of toxic, reactive, and air-sensitive precursors at high temperatures, microfluidic systems are well suited for process optimization as well as mechanism studies.[73-74]

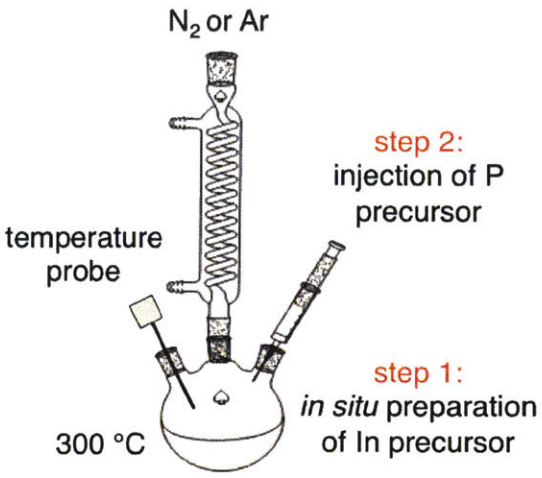

Figure 2-1: A schematic view of the batch synthesis procedures for InP QDs adapted from the work of Peng and coworkers.[24]

High temperature microfluidic systems have been demonstrated for the synthesis of II-VI and III-V QDs such as CdSe and InP in single-phase flow reactors.[54, 75] Due to the high temperature syntheses (up to 300°C), solvents with high boiling points such as 1-octadecene have been chosen that remain liquid over a wide temperature range. In order to maintain the flow conditions, solvents should be able to dissolve the precursors at ambient conditions as well. These requirements significantly limit the set of solvents, ligands, and precursors that are compatible with continuous flow systems. Furthermore, the solvents satisfying these requirements are very viscous, leading to slow mixing and broad residence time distribution, which can result in a broad size distribution of the QDs. One approach to resolve these limitations is to segment the reacting phase using an immiscible phase, which can narrow the residence time distribution and thus improve the mixing performance. Syntheses of QDs using liquid-gas and liquid-liquid segmented flows have been demonstrated with high reproducibility and scale-up potential.[76-79] However, even with segmentation, limitations on compatible

solvent/precursor combinations still remain a major obstacle in the application of flow reactors as a universal platform for QD synthesis.

Another way to expand the range of available solvents, precursors, and ligands in flow reactors is to apply high pressure into the system, which can maintain low-boiling-point solvents within the reactor in a liquid or supercritical phase.[80] Examples of such solvents are hexane, pentane, octane and toluene. In particular, the use of supercritical fluids allows for tuning the density of a fluid from a gas-like to a liquid-like phase and tuning the diffusivity in the opposite way, providing fast diffusion rate while retaining sufficient solubility for a variety of precursors or ligands. Gas phase reactants such as ammonia can also be used as the nitrogen source for nanomaterial synthesis.[81] Marre and co-workers developed a strategy to construct silicon-pyrex chip microreactors that can withstand high pressure and temperature conditions (up to 25 Mbar and 400 °C).[82] They were also able to couple online characterization techniques such as UV-Vis absorbance in the flow system, enabling fast screening and process optimization. Applications of HT and HP microchemical systems to nanomaterial synthesis have been demonstrated with metal, metal oxide, and semiconductor materials.[83] In particular, they have been successfully applied for the synthesis of II-VI and III-V core and core-shell QDs.[53, 55, 84-85]

2.1.2 Experimental Set-up

We have implemented an HT and HP microfluidic system to study the growth behaviors of III-V QDs. The platform consists of four parts (Figure 2-2): 1) high pressure syringe pumps, 2) multistage microreactors, 3) inline characterization unit, and 4) high pressure sample collector. Two types of microreactors have been used: silicon-pyrex-based chip reactors, and stainless-steel tube reactors. The use of multistage reactors allows for the independent control of growth temperatures and also enables additional injections of reagents during the QD synthesis. A

detailed description of the design, fabrication and assembling of the silicon-pyrex chip reactors can be found elsewhere.[53]

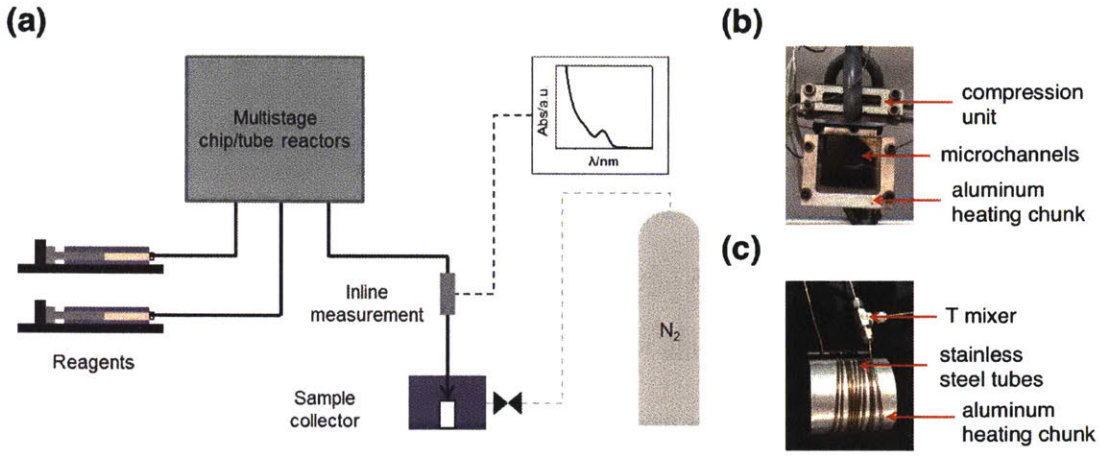

Figure 2-2: (a) Schematic view of a high temperature and high pressure reactor system; images of an assembled (b) chip reactor and (c) tube reactor. Cooling unit of the chip reactor and Insulation layer of the tube reactor are not shown.

Chip reactors have similar inert surfaces as conventional glass flasks, and their microchannels and injection ports can be customized via microfabrication. However, the fabrication process is expensive and complicated. Chip reactors are also fragile and their sizes are constrained by that of silicon wafers. As an alternative, stainless-steel tube reactors are relatively cheaper and easier to assemble with a wide choice of dimensions and lengths. Their inner walls can be coated with other materials such as silicon to eliminate surface effects during QD growth. They also have greater potential to be used in larger-scale industrial applications. A typical inner diameter is chosen around 0.02 inch for the tube reactors used in our work. The tubes are wrapped around cylindrical aluminum rods with a heating cartridge inserted in the center for heating. A highly efficient insulation layer composed of fiberglass and wool covers the stainless steel tubes. COMSOL simulation shows that the temperature difference across the

whole heated volume with perfect insulation around the wall is within 5 °C. The growth behaviors of InP QDs are compared using both chip and tube reactors. It is found that the 2-stage chip reactor and tube reactor systems with comparable heated volumes of individual stages produce InP QDs with similar absorption spectra under identical growth conditions (Figure 2-3).

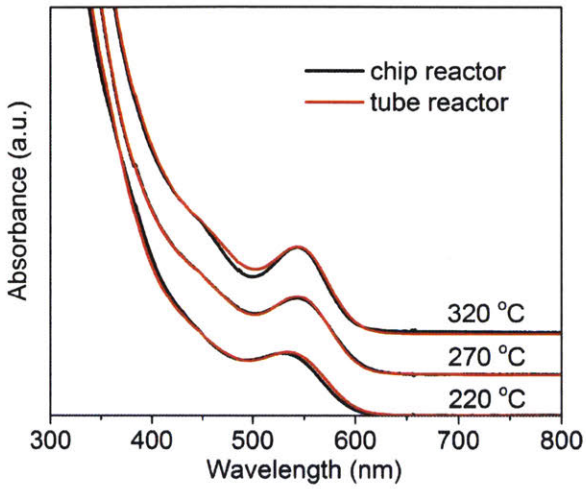

Figure 2-3: Absorption spectra comparison of InP QDs grown in two reactor systems. The temperature of the first stage is 130 °C and the temperature of the second stage is shown in the figure.

2.2 Group V Precursor Chemistry

Starting from the hypothesis that the high reactivity of group V precursors causes the limited size tunability and broad size distribution of III-V QDs, different group V precursors with lower reactivity have been synthesized. Joung and coworkers first reported the use of tris(tert-butyldimethylsilyl)phosphine, a modified precursor from $P(TMSi)_3$, for the synthesis of large-sized InP QDs with well-controlled size distributions.[86] Similarly, Harris and co-workers suggested the use of other TMSi analogs, such as the less reactive trimethylgermyl (TMGe) derivatives ($P(TMGe)_3$ and $As(TMGe)_3$), to improve the size distribution of InP and InAs QDs.

Following Harris' study, Baek et al. further compared the growth behaviors of these QDs synthesized with these less reactive precursors in a two-stage HT and HP chip reactor system. The use of such reactors eliminates the inconsistency in injection speed, stirring rate and heat transfer encountered in batch reactors. For InP and InAs QDs, the precursors are mixed at the first stage at a moderate temperature and then transported to the second stage at an elevated growth temperature. For syntheses using TMSi derivatives, the mixing temperature is found to have no effect on the QD growth, indicating the fast depletion of precursors. However, the temperature increase of the second stage facilitates the QD formation. In the case of InP QDs, the growth stops after a certain temperature, possibly due to the slowing down of the inter-particle ripening or coalescence processes. The growth behaviors of InP QDs using TMSi and TMGe derivatives do not show much difference, possibly due to the relatively small differences between their reactivities. However, for InAs QDs, the synthesis using TMGe derivatives produces QDs with sharper absorption features and their first absorption peak blue-shifts with the increase of the first-stage temperature. It is proposed that unreacted precursors may exist during the growth of InAs QDs due to the lower reactivity of $(TMGe)_3As$ as compared to $(TMSi)_3As$.

Encouraged by previous studies[41,53,86], we have performed a more systematic study on the role of group V (V = P, As) precursor chemistry. Two kinds of group V precursors have been synthesized and characterized in the Bawendi Group: triethylgermyl (TEGe) and isopropyl-dimethylsilyl (iPrDMSi) derivatives. *In situ* UV-Vis absorbance measurement in batch has been used to compare the reactivity of these precursors, which is found to span two orders of magnitude at 130 °C following the trend: $(TMSi)_3V > (TMGe)_3V > (TEGe)_3V > (iPrDMSi)_3V$. The quantitative measurement of the precursor reactivity can be found elsewhere.[52] Two-stage

HT and HP chip reactors are used to fast-screen reaction conditions and compare their growth behaviors.

Figure 2-4 shows the absorption spectra of InP and InAs QDs synthesized with these precursors at different temperatures. Regardless of their different reactivities, sharper absorption spectra are obtained at a high growth temperature around 320 °C for InP QDs, while intermediate growth temperatures around 220–270 °C are desirable to produce InAs QDs (Figure 2-4 A and C). Additionally, at high growth temperatures, the precursor reactivity does not affect the final particle size, and the use of the most reactive TMSi derivatives produces QDs with the narrowest size distribution. For both InP and InAs QDs, the growth dependence on the precursor reactivity is more obvious at lower growth temperatures, where in general large particle sizes are obtained with less reactive precursors. These results present a dilemma for the synthesis of III-V QDs by tuning the precursor chemistry. On the one hand, low-temperature synthesis produces the largest QDs with the least reactive precursors but with the broadest size distribution. On the other hand, high-temperature synthesis produces QDs with the narrowest size distribution but the particle size is independent of precursor reactivity. This insensitivity to precursor reactivity is further proved by the invariant growth of III-V QDs at different mixing temperatures when a high growth temperature is used for the final nanocrystal formation (Figure 2-4 B and D).

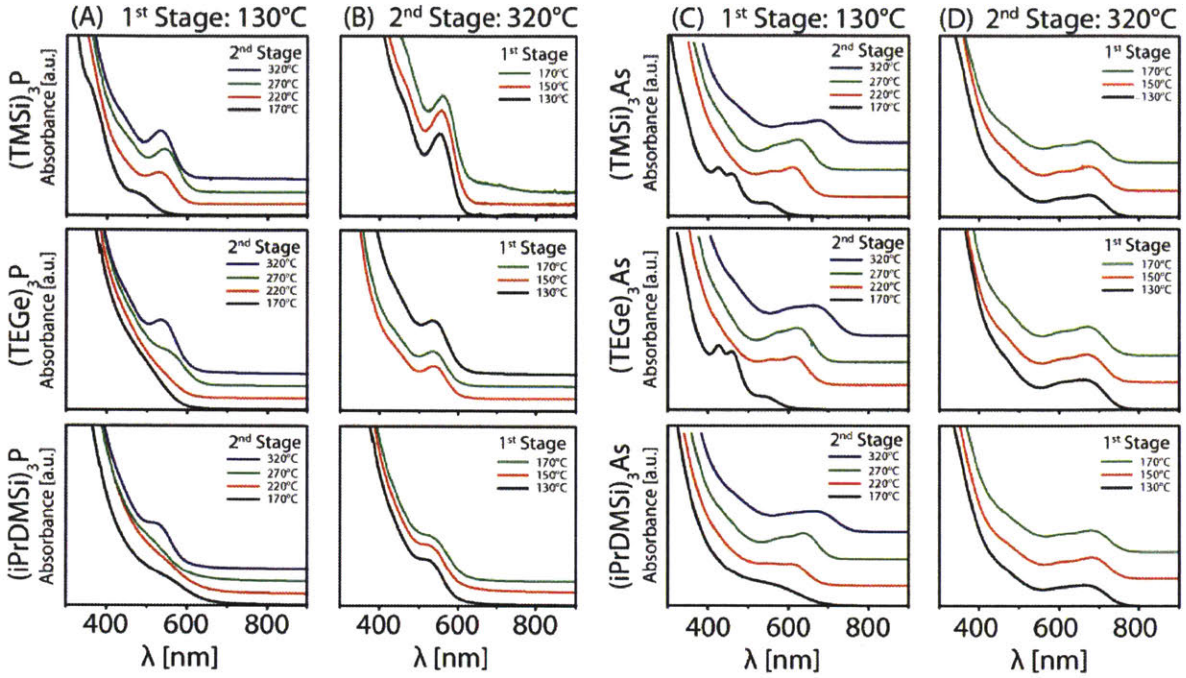

Figure 2-4: Optimization of growth conditions for different precursors using a two-stage chip reactor. Reproduced with permission from [52]. Copyright 2016 John Wiley and Sons.

The differing impact of precursor reactivity on III-V and II-VI QDs can be explained by considering different growth processes for both. For II-VI QDs, their monomeric species grow on the formed nuclei and the precursor reaction rates can significantly affect the final nanocrystal formation. However, for III-V QDs, their precursors, regardless of their reactivity, may form stable intermediate clusters first and then these intermediates further react to form larger nanocrystals. Higher precursor reactivity may lead to faster formation of these intermediates with better-defined absorption spectra, and a more homogenous cluster sample can result in a better-controlled final QD size distribution. In addition, the low-temperature growth difference caused by the precursor reactivity can be eliminated at high temperatures, as the thermal energy is sufficient to overcome the cluster-interaction barriers.

We have also investigated the effect of precursor ratio on the growth of InP QDs using a two-stage chip reactor with the two less reactive precursors, $(TEGe)_3P$ and $(iPrDMSi)_3P$ (Figure 2-6). It is found that for both precursors, increasing indium ratio over phosphorus enhances the size distribution of QDs, possibly due to the stabilization of cluster intermediates in the presence of excess indium.

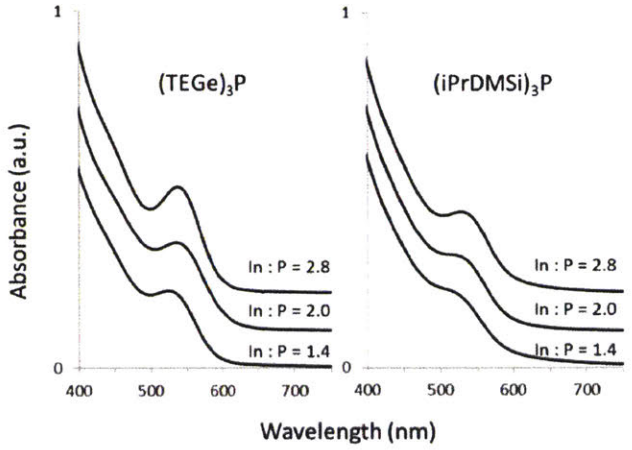

Figure 2-5: Absorption spectra of InP QDs obtained using different In and P ratios in a two-stage chip reactor. The mixing temperature is 130 °C and the growth temperature is 320 °C.

A three-stage synthesis is also applied to study the effect of growth time with $(TEGe)_3P$ and $(iPrDMSi)_3P$ as precursors (Figure 2-6). In both cases, the same growth behaviors are observed when the second-stage temperature is set the same as the first or third stage (namely, 130 °C or 320 °C in our study). These similarities indicate the completion of reactions in either the first or third stage. When the second-stage temperature is varied between 130 and 320 °C, a red shift and broadening of the spectrum is observed, in particular at 220 °C, possibly due to the change of the kinetic stability of cluster intermediates. This study also demonstrates the advantage of having good temperature control in flow systems, as the growth during the transient temperatures causes the broadening of QD size distribution.

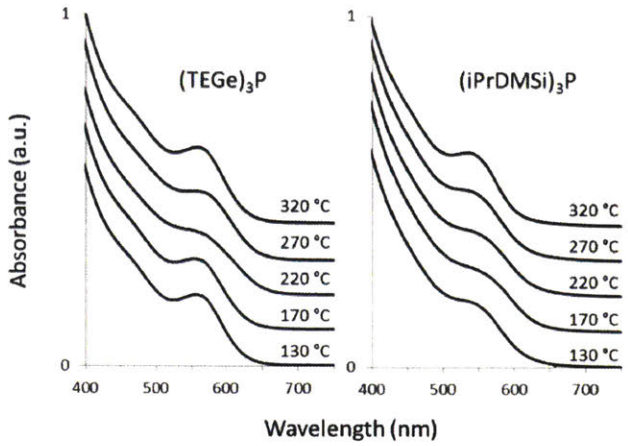

Figure 2-6: Absorption spectra of InP QDs synthesized with a three-stage chip reactor. The first/third stage temperature is 130/320 °C respectively. The second-stage temperature is shown in the figure.

The dilemma of tuning the precursor chemistry can be partially resolved by mixing the most and least reactive precursors for the syntheses. The growth study of InP QDs by mixing TMSi and iPrDMSi derivatives at different ratios is shown in Figure 2-7. At a low growth temperature where the reactivity of the two precursors has a larger difference, addition of the more reactive TMSi derivatives helps in narrowing the QD size distributions and also in increasing the QD sizes. However, when the growth temperature increases, the improvement becomes insignificant, possibly due to the similar reactivity of these two precursors.

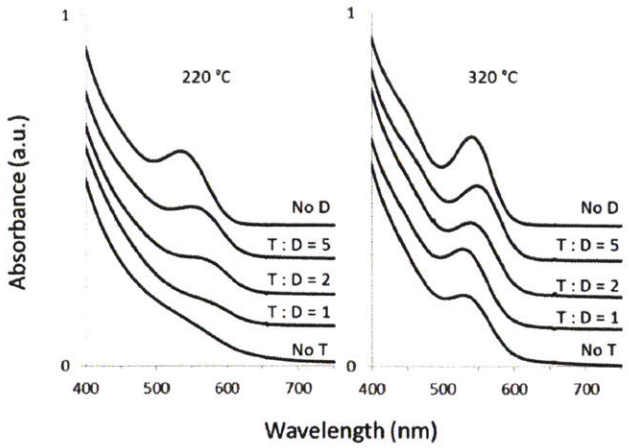

Figure 2-7: Absorption spectra of InP QDs obtained at different ratios of $(TMS)_3P$ (T) to $(iPrDMSi)_3P$ (D) with different second-stage temperatures. The first-stage temperature is 130 °C.

Recently, Gary et al. reported the synthesis of InP QDs using less reactive group V precursors such as triarylsilylphosphines.[87] Similar to our results, their study shows that the use of low reactivity precursors is not able to separate the nucleation and growth during QD formation, thus broadening the nanocrystal size distribution. They proposed an alternative synthetic method of mixing phosphorus precursors with different reactivities to achieve the separation between nucleation and growth. With this alternative approach, they were able to improve the size distribution of InP QDs.

2.3 Conclusion

Both our study and recent literature have shown that tuning precursor reactivity is not sufficient to improve particle size tunability and size distribution, although this strategy has proven to be successful in adjusting the growth of II-VI and IV-VI QDs. Existing models for II-VI and IV-VI formation and growth are thus non-predictive for the synthesis of III–V QDs, and additional fundamental research is required to improve our current understanding of the factors that determine final particle size and size distribution for III-V QDs.

2.3.1 A Two-Stage Growth Model of InP QDs

The unexpected role of precursor reactivity motivates further mechanism investigation into the growth of III-V QDs, in particular InP QDs. A two-stage growth model has been proposed where precursors are depleted at the early stage of growth to form cluster intermediates, and then intermediates transform into large nanocrystals (Figure 2-8).[47] A 1.3 nm InP cluster synthesized from indium phenyl acetate and $P(TMSi_3)_3$ has been experimentally characterized, strongly supporting this hypothesis.[88]

Figure 2-8: A two-stage growth model of InP QDs

Based on the two-stage model, we are interested in improving our understanding of the role of precursor chemistry in the early-stage QD growth, as it is found to contradict the current QD growth model. Additionally, we are also interested in the role of these cluster intermediates and how they participate in the late-stage growth of InP QDs. The following chapters will be a more detailed discussion of these two topics. Specifically, Chapter 3 and 4 introduces several first principle approaches and our use of these approaches in understanding the early-stage precursor conversion mechanisms. Chapter 5 shows our experimental characterization of cluster intermediates and on their roles of during InP QD growth.

Chapter 3

First Principles Methods

3.1 Electronic Structure Calculations

Electronic structure theory describes the motion of electrons in the electrostatic field generated by the nuclei in atoms or molecules. In quantum chemistry, quantum mechanics are used to solve the electronic motions due to the wave-like property of electrons. By employing the Born-Oppenheimer approximation, the motion of electrons is separated from that of nuclei, and the calculated electron energy at each nuclear configuration generates the potential energy surface (PES). Under these assumptions, the time-independent many-body electronic Schrödinger equation gives the electron energy at a certain nuclear configuration as

$$\hat{H}_{el}\Psi = E_{el}\Psi$$

In atomic units,

$$\hat{H}_{el} = -\frac{1}{2}\sum_i \nabla_i^2 - \sum_A \sum_i \frac{Z_A}{|r_i - R_A|} + \sum_{i>j} \frac{1}{|r_i - r_j|}$$

Here, the Hamiltonian operator ($\hat{H}_{el}$) accounts for the kinetic energy of electrons, the Coulomb attraction between electrons and nuclei, and the Coulomb repulsion between electrons. The electron energy (E_{el}) depends on the nuclear configuration (R_A). Hartree-Fock theory and Density Functional Theory are some of the most frequently employed methods to approximately solve this electronic structure problem.

3.1.1 Hartree-Fock Theory

Hartree-Fock theory has fundamental importance to current electronic structure calculations. To solve the time-independent many-body electronic Schrödinger equation, it assumes that the overall electron wavefunction (Ψ) can be described by a modified form of Hartree Product that satisfies the anti-symmetry principle, known as the Slater determinant. Each component in this determinant represents an individual electron wavefunction (χ) that is independent of other electrons.

$$\Psi_{HF} = \frac{1}{\sqrt{N!}} \begin{vmatrix} \chi_1(r_1) & \chi_2(r_1) & \cdots & \chi_N(r_1) \\ \chi_1(r_2) & \chi_2(r_2) & \cdots & \chi_N(r_2) \\ \vdots & \vdots & \ddots & \vdots \\ \chi_1(r_N) & \chi_2(r_N) & \cdots & \chi_N(r_N) \end{vmatrix}$$

It can be shown that the use of Slater determinant to describe Ψ is equivalent to assuming that each electron moves in an electric field that is averaged from the Coulomb repulsion of all other electrons. Because of the antisymmetrization of the determinant, each electron also feels an exchange interaction.

According to the variational theorem, which describes the true electronic energy at the global minimum, an upper limit of E_{el} can be obtained as:

$$E_{el} \leq E_{el}^{HF} = \langle \Psi_{HF} | \hat{H}_{el} | \Psi_{HF} \rangle$$

As the individual electron wavefunctions (χ) are unknown, some initial guesses of these wavefunctions (or orbitals) can be made and then used to calculate the electron energy. Using the variational theorem, the initial guesses can be refined iteratively until the electron energy reaches a local minimum (this process is also called a self-consistent-field approach). It should be mentioned that this local energy minimum depends on the choice of orbitals (also known as basis

sets). A larger basis set usually corresponds to a closer approximation of the exact E_{el}^{HF}. However, since a single determinant is used to describe Ψ in Hartree-Fock theory, even with a complete basis set, the correlation energy is absent in this approach, which is described as the difference between E_{el}^{HF} and the exact energy of the system. To improve the accuracy, post Hatree-Fock methods such as Coupled Cluster[89] and Møller-Plesset perturbation theory[90] have been used. These methods are very computationally intensive and are only applicable to systems with small sizes.

3.1.2 Density Functional Theory

Density functional theory (DFT) is one of the most popular and versatile methods applied in quantum chemical calculations. It is a balance between computational cost and calculation accuracy. As with Hartree-Fock theory, it aims to solve the electronic Schrödinger equation after making the Born-Oppenheimer approximation. However, unlike Hartree-Fock theory, which tries to calculate the electronic energy by solving the 3N-dimensional equation, DFT reformulates the energy equation into a form that depends on the 3-dimension electron density ($\rho(r)$), as demonstrated by Hohenberg and Kohn[91]:

$$E(\rho(r)) = F(\rho(r)) + \int V(r)\rho(r)\mathrm{d}r$$

Where $F(\rho(r))$ is a universal functional that accounts for the energy contribution from the electron kinetic energy and Coulomb repulsions, and $V(r)$ is the external electrostatic field generated by the positively charged nuclei. As with Hartree-Fock theory, with a known form of $F(\rho(r))$, the energy can be obtained through the variational theorem using the self-consistent-field approach.

In real applications, the form of the universal functional is not regularly used because it is difficult to evaluate energy of the electrons without information about their wavefunctions. Kohn and Sham[92] reformulated this universal potential by mapping the real system of interacting electrons onto a fictitious system of non-interacting electrons with the same electron density. The universal functional can be written as the sum of the kinetic energy of the non-interaction electrons, the Coulomb interactions described through their density and a lumped term which accounts for the additional interactions in the real system as compared to the fictitious system. This last term is called the exchange-correlation energy. The form of this exchange-correlation energy is unknown and the practical use of DFT requires the development of this exchange-correlation term under different assumptions.

The local density approximation (LDA)[92] is the simplest approximation made to describe the exchange-correlation term. It assumes that the electrons behave locally as a homogeneous electron gas with constant density. More complicated approximations include the generalized gradient approximations (GGA)[93] and the meta-GGA[94]. Unlike LDA, which assumes constant density, the GGA considers the changes in electron density away from the coordinates. GGA corrects the tendency of LDA to overestimates the exchange-correlation energy. A meta-GGA is a further modification after GGA where the second derivatives of the electron density are included in constructing the exchange-correlation term. Regardless of the different correction schemes, these assumptions are all based on mean-field approximations and they are expected to work well with systems with delocalized electrons.

Hybrid functionals[95] are another class of methods that are commonly used to describe the exchange-correlation term. They incorporate a portion of exact change from Hartree-Fock theory and correlation from other methods. These hybrid functional are developed because although

DFT has the explicit treatment (in principle, exact) of electron correlation,the exchange is not inexact. The introduction of Hartree-Fock exchange in these hybrid functions can approximately correct for this inexact exchange. For example, the most widely used hybrid method, B3LYP[96-98], includes the contribution from Hartree-Fock exchange, both LDA and GGA exchange and correlation functionals.

$$E_{XC} = E_X^{LDA} + a_0(E_X^{HF} - E_X^{LDA}) + a_X(E_X^{GGA} - E_X^{LDA}) + a_C(E_C^{GGA} - E_C^{LDA})$$

Where $a_0 = 0.2$, $a_X = 0.72$ and $a_C = 0.81$.

3.2 Ab Initio Molecular Dynamics

Molecular dynamics (MD) have long been applied to study the interactions within a complex system. The accurate evaluation of forces is essential in capturing these interactions. Forces can be obtained from various methods including force fields such as pair potentials, multi-body potentials, tight binding models, or reactive potentials. Alternatively, quantum-mechanical forces may be evaluated from electronic structure calculations using the Hellmann-Feynman theorem[99]:

$$F_I = -\langle \Psi | \frac{\partial \hat{H}}{\partial R_I} | \Psi \rangle$$

Where, F_I is the force acting on an ion I, $\hat{H}$ is a Hamiltonian operator depending on the coordinates R_I, and Ψ is the eigenfunction of the Hamiltonian. The MD method of using quantum-mechanical forces is called *ab initio* molecular dynamics (AIMD). Unlike classical MD, which uses empirical potentials to generate potential energy surfaces (PES) that are typically restricted to two-body contributions, AIMD methods calculate PES based on first-principles methods where many-body terms are included automatically, and therefore are more

accurate. Born-Oppenheimer (BO) MD and Car-Parrinello (CP) MD are the two commonly applied AIMD methods.

Under the Born-Oppenheimer assumption, BOMD straightforwardly solves the time-independent Schrödinger equation at each MD step with fixed nuclear positions, and then subsequently propagates the nuclei positions using Newton equations of motions. At each time step of the trajectory, the electron wavefunctions are minimized to their ground state, the forces acting on the nuclei are computed, and the nuclear coordinates are updated. The resulting BOMD method for the electron ground state is defined as

$$M_I \ddot{R}_I(t) = -\nabla_I \min_{\Psi_0}\{\langle \Psi_0 | \hat{H}_{el} | \Psi_0 \rangle\}$$
$$E_0 \Psi_0 = \hat{H}_{el} \Psi_0$$

Where, M_I is the ion mass, $\ddot{R}_I(t)$ is the acceleration of the ion at time t, and Ψ_0 is the ground state wavefunction of the electron Hamiltonian ($\hat{H}_{el}$). As there are no electron dynamics in BOMD, the electronic structure needs to be solved self-consistently at each MD step.

While the electronic and nuclear motions are separated in BOMD, CPMD explicitly includes the electrons as active degrees of freedom with fictitious masses. After an initial standard electronic minimization, the fictitious dynamics of the electrons keeps them on the electronic ground state corresponding to each new ionic configurations visited along the dynamics, thus yielding accurate ionic forces. There is no need for a self-consistent iterative minimization at each time step. However, both nuclear and electron configurations need to be updated during the iterations. In CPMD, the fictitious mass of the electrons should be chosen such that is small enough to avoid a significant energy transfer from the ionic to the electronic degrees of freedom. The small fictitious mass in turn requires the equations of motion to be integrated using a smaller

time step than the one commonly used in BOMD simulations. In the formal limit where the fictitious mass approaches zero, the equations of motion approach BOMD.

Regardless of the MD methods, the algorithm used to update position and velocity during the iteration is very important, which is called an integrator. The Velocity Verlet algorithm is a commonly used integrator, where the velocity and position are calculated at the same time period. As the velocity in this integrator is determined in a non-cumulative way from the two positions, the global error of the velocity is the same as that of the position ($O(\delta t^2)$). The position and velocity updating scheme in this integrator is as follows:

1. Calculate $x(t+\delta t) = x(t) + v(t)\delta t + \frac{f(t)}{2m}\delta t^2$
2. Obtain $f(t+\delta t)$ from $x(t+\delta t)$
3. Calculate $v(t+\delta t) = v(t) + \frac{1}{2m}[f(t) + f(t+\delta t)]\delta t$

With Newton equations of motions, the MD simulations are carried out in the microcanonical assemble, where the energy, volume and number of particles are kept as constant. However, in real experiments, conditions with constant temperatures are often applied and the corresponding assemble is called the canonical assemble. To allow MD sampling at a constant temperature, the velocities of the system are modified during the iterations as the kinetic energy of the system determines its temperature according to the Maxwell-Boltzmann distribution. Common techniques to control the temperature (velocities) include velocity rescaling, Andersen thermostat, the Nosé-Hoover thermostat and Langevin dynamics, to name a few. The velocity rescaling method is very straightforward, but it is also very unphysical. More frequently used are thermostats, where a heat bath is introduced to balance the thermal energy of the system. For example, Nosé-Hoover thermostat considers the heat bath as part of the system

with a fictitious variable with mass and velocity. Langevin dynamics mimics solvent effects and introduce a small damping force to control the system temperature.

3.3 Transition State Search

The harmonic approximation to transition state (TS) theory is used to predict the rates of chemical reactions. However, finding transition states on potential energy surfaces (PES) can be extremely difficult and remains one of the major challenges in chemical kinetics for medium and large systems. There are two categories of methods in TS search: the surface walking algorithms and the interpolation methods. Surface walking algorithms are usually based on a local quadratic approximation of the PES and can perform poorly for systems with several low-frequency vibrational modes (namely flat PES). These methods typically require good initial guesses and therefore it becomes challenging for searches starting far from the TS. As for the interpolation methods, both reactant and product information are required to obtain an inner-connected path which can eventually converge onto a minimum energy pathway (MEP). In difficult cases, a combined approach to enhance both the accuracy and efficiency of TS search can be used which utilizes the interpolation methods to obtain a good initial guess from an unconverged MEP and then optimize the initial guess into TS using surface walking algorithms.

3.3.1 Interpolation methods

Straightforward interpolation methods include linear synchronous transit (LST) and quadratic synchronous transit (QST). LST simply searches for a maximum along a linear path connecting reactants and products, while QST not only searches for a maximum along an arc but also makes sure it is also a minimum in all directions perpendicular to the arc. Both methods can end up with wrong or higher order saddle points. Improved interpolation methods include nudged elastic

band (NEB)[100] and the string method[101]. Both methods require an initial guess of the pathway that can be obtained through LST or QST. In NEB, different images (or nodes) are generated and relaxed to the MEP through a force scheme projected to the band. In the scheme, the potential forces act perpendicular to the band. The spring forces act along the band to overcome the parallel forces that tend to drag the nodes back to the nearby local minimum. Careful choice of Hooke constants for the spring forces is necessary to keep the nodes uniformly spaced along the path. Overall, the combined potential forces and string forces will drag the band towards the MEP. The concept behind the string method is very similar to NEB. It consists of two steps: the first step is called the evolution step, and its goal is to minimize the perpendicular forces acting on all the nodes. The second step is called re-parameterization step. It does not have a spring force to redistribute the nodes. It redistributes the nodes along the string after each evolution step and depends on a uniform parameterization density.

As both NEB and the string method require the input of an initial pathway, unchanged node number and uniform node distribution, a more flexible string method has been developed and it is called growing string method (GSM)[102]. With reactant and product information, the method intentionally chooses a variable parameterization density to focus nodes near the TS or near curves in the reaction pathway. The node number evolves during the iterations until the two ends are connected. As GSM eventually converges onto MEP, it is very computationally expensive. Practically, if only information on the TS is required, it is not necessary for GSM to converge and it can just provide an initial guess for the later TS search using surface walking algorithms. This idea motivated the development of the freezing string method (FSM)[103]. This method freezes newly grown nodes after a fixed number of iterations and it only aims to provide a good initial TS guess. As compared to GSM, FSM reduces computational cost by only interpolating

paths based on the innermost nodes instead of all nodes, growing nodes after only a few perpendicular optimization steps in frontier notes and not redistributing nodes along string.

3.3.2 Surface Walking Algorithms

With an initial guess structure, TS search via surface walking algorithms becomes a mathematical problem of locating the first-order saddle point on PES. To refine the guess, common eigenvector-following methods, such as partitioned-rational function optimization (P-RFO)[104], can be used. P-RFO is derived from the rational function optimization (RFO) method and it partitions the RFO matrix into two matrixes, maximizing along one mode (k) and minimizing along the rest. The mode (k) is generally chosen to correspond to the lowest Hessian eigenvalue.

$$\Delta x = \sum_{j=1}^{n} \Delta x_j$$
$$\Delta x_k = u_k^T f u_k / (\lambda_k - \gamma_p)$$
$$\Delta x_{i,i\neq k} = u_i^T f u_i / (\lambda_i - \gamma_n)$$

Where, Δx is the modified Newton-Raphson step, u_k is the eigenvector, λ_k is the eigenvalue and f is the force at the current configuration. P-RFO ensures movement uphill along the lowest Hessian eigenvector and downhill along all other along the lowest Hessian eigenvectors by introducing a shift parameter to the method (γ_p and γ_n). The shift parameter can be found iteratively based on the rational functional approximation from the RFO matrix. As the quality of the Hessian matrix strongly affects the TS search reliability in P-RFO, an exact Hessian calculation is performed beforehand. The corresponding cost normally scales as one power of system size higher than the energy or gradient calculations, making P-RFO searches expensive

for large systems. In general, it is the dependence on the correct local Hessian structure that is the greatest weakness of these standard Hessian-based TS search algorithms.

In recent years, Hessian-free surface walking algorithms have been developed to reduce the computational cost in locating TS. Standard examples are dimer methods and their improved versions[105-106]. In general, these methods approximate local curvatures (second derivatives of the potential energy) using forces (first derivatives of the energy) evaluated at the two end points on a dimer, thus eliminating the Hessian calculation. Through rotation and translation, the dimer can be oriented towards the lowest curvature mode (also the MEP direction). Once the dimer is aligned with the MEP, the force parallel to the dimer is inverted, making the dimer climb up to the saddle point. The careful choice of rotation and translation directions and steps are important parameters in determining the accuracy and efficiency of dimer methods. Additional discussions on dimer methods can be found in the Appendix.

Chapter 4

Early-Stage Indium Phosphide Quantum Dot Growth Mechanisms

4.1 Introduction

Current experimental techniques that can be used to characterize III-V clusters and QDs have not been able to identify the difficult-to-isolate early-stage intermediates. However, the formation mechanisms of these intermediates are essential in understanding the role of precursor chemistry. These challenges motivate the use of first-principles simulations to investigate early-stage growth intermediates. The lack of experimental information about the nature of III-V QD growth intermediates necessitates a sampling approach to first discover possible pathways rather than directly evaluating energetics for predefined pathways. AIMD simulations (in particular, BOMD) has been widely employed as a discovery tool where mechanisms were not already known, including, for example, the growth of carbon nanotubes or graphene on metal nanoparticles or surfaces[108-110], water splitting on InP/GaP surfaces[65-67], CO oxidation on ceria-supported gold nanoclusters[111] and water oxidation by cobalt nanoparticles[112]. These simulations are constrained to short timescales and small system sizes in order to avoid prohibitive computational cost. Barriers of key reaction steps must also be at or below the thermal energy

available in the simulation to ensure sufficient sampling. Strategies that enhance sampling efficiency within AIMD include high-temperature acceleration[113], replica exchange[114], and metadynamics[115] to name a few. Alternatively, use of multiple, lower levels of theory can reduce computational cost and enable accelerated discovery, for example through the use of reactive force fields[116] or mixed quantum-mechanical/molecular mechanics techniques[117]. Recent work has also shown the possibility of discovering hundreds of new reaction pathways starting from a mixture of organic molecule species with AIMD sampling that is accelerated through high-temperature, relatively approximate first-principles methods, and variable boundary conditions.[118]

As will be seen, we have employed variable boundary, high-temperature AIMD simulations starting from indium and phosphorus precursor mixtures in order to elucidate the nature of reaction mechanisms in early-stage InP QD formation. This approach enables us to observe the interactions and elementary reaction pathway steps that lead to formation of InP clusters. From these trajectories, we extract key reaction steps, and characterize their associated minimum energy pathways. In this chapter, I will first present computational details into the acceleration strategies and approximations made in order to enable the sampling and observation of growth dynamics of InP clusters at reasonable computational cost. I will then discuss the results of our AIMD simulations including observations of cluster formation and evaluation of the intermediate structures. Lastly, I will show our determination of reaction pathway energetics based on BOMD trajectories.

4.2 Computational Details

Our AIMD simulations were performed with the graphical-processing unit (GPU)-accelerated quantum chemistry package, TeraChem[119-120]. Indium acetate ($In(Ac)_3$) and phosphine

(PH_3) are used as the model indium and phosphorus precursors. One to seven $In(Ac)_3$ molecules and six to thirty PH_3 molecules are used in the AIMD simulations with the ratio between $In(Ac)_3$ and PH_3 molecules ranging from one to ten (Table B 1). Twenty AIMD simulations were performed for a total simulation time of about 330 ps. Initial spherical AIMD configurations were generated using Packmol[121-122], with a minimum 3 Å van der Waals distance between individual molecules. AIMD simulations were carried out at constant temperature (T = 2000 K) using a Langevin thermostat with a damping time of 0.3 ps. The 5.5 to 40 ps Born-Oppenheimer MD simulations were carried out with a 0.5 fs time step. The electronic structure for AIMD simulations was evaluated at the Hartree-Fock (HF) level of theory with the 3-21G[123] basis set.

Simulations were carried out with either constant or variable spherical boundary conditions. Molecules outside the initial radius, denoted r_1, experience a harmonic restraining force, while no force is applied to atoms inside the sphere. In the case of variable spherical boundary conditions, every 1.5 ps a Heaviside function was used to instantaneously decrease the boundary condition radius from r_1 to r_2 for 0.5 ps, after which the radius returned to its original value. The initial radius of the sampling space is chosen between 8 and 10 Å depending on the system size. For all variable spherical boundary condition simulations, the ratio of r_2 to r_1 was set to be between 0.6 and 0.7. Coordination numbers evaluated for molecular dynamics trajectories are evaluated based on rescaled covalent radii (1.25x) of indium, phosphorus, oxygen, and hydrogen atoms. These distance cut-offs are: 2.56 Å for In-O bonds, 3.16 Å for In-P bonds, and 1.79 Å for P-H bonds.[124] The values of these distance cutoffs also agree with the first local minimum on the radial distribution curve of In-O, In-P or P-H distance obtained from AIMD simulations.

Structures obtained from the HF AIMD trajectories were extracted for further evaluation with density functional theory (DFT) including geometry optimization and transition-state search and

characterization. Since the synthesis of InP QDs is carried out using solvents with low dielectric constant ($\varepsilon = 2$), all the energetic evaluations are performed in vacuum. DFT calculations in TeraChem employed the default B3LYP[96-98] functional, which uses the VWN1-RPA form[125] for the local density approximation component of the correlation. The composite basis set consisted of Los Alamos effective core potentials (LANL2DZ) for indium atoms and the 6-31G* basis set for all other atoms, which we refer to by the common short hand notation, LACVP*. Geometry optimizations of snapshots from AIMD trajectories were carried out in TeraChem using the DL-FIND[126] module with the L-BFGS algorithm in Cartesian coordinates. Default thresholds of 4.5×10^{-4} hartree/bohr for the maximum gradient and 1.0×10^{-6} hartree for change in self-consistent energy were employed. Partial charges were obtained from the TeraChem interface with the Natural Bond Orbital (NBO) v6.0 package[127]. NBO calculates the natural atomic orbitals (NAOs) for each atom by computing the orthogonal eigenorbitals of the atomic blocks in the density matrix, and the NBO partial charge on an atom is obtained as the difference between the atomic number and the total population for the NAO on the atom.

To characterize the energetics of different reactions, molecules that participated in reactive events were extracted from the overall AIMD trajectory and further processed to obtain transition state (TS) structures and activation energies. The reacting subset was identified based on observing changes in connectivity between molecules. Reactant and product structures were first geometry optimized using QChem 4.0[128] using the B3LYP/LACVP* level of theory. We validated our choice of functional and confirmed that alternative functionals did not substantially change predicted energetics (Table B 2). Two energetic characterizations were carried out for bond rearrangement. In the case of isolated bond dissociation or formation events (e.g. indium precursor agglomeration, indium-phosphorus precursor adduct formation), constrained

optimizations were carried out in which only the bond distance (e.g. In-O or In-P) was held fixed at values that span the relevant reaction coordinate. In the remaining cases (e.g. indium-precursor-assisted P-H bond dissociation), transition state searches were carried out in a multi-stage process. First, the freezing string method[129] was used to provide an interpolated path connecting the geometry-optimized reactant and product structures. In this method, linear synchronous transition (LST) is used for the initial interpolation of new path images that grow inward from reactant and product sides, and these structures are then optimized with the quasi-newton method with hessian update for up to a number of user specified steps (in our case, 3). The final number of images in the path approaches a target density (here, 21) but may exceed that value because a new image is guessed for the path until reactant- and product-derived paths cross. Unlike other path-based transition state search methods, the freezing string method does not obtain a converged minimum energy path but aims to provide a good guess for the location of a TS at reduced computational cost. The highest-energy image from the freezing string path was used as an initial guess for a P-RFO TS search. These TSs were characterized by an imaginary frequency corresponding to the expected nuclear motion. For the dissociation processes involving multiple indium precursors, a second imaginary frequency with zero intensity and a value of <30i cm^{-1} was obtained. Due to the abundance of soft modes in many of the structures, zero-point vibrational energy and entropy corrections were omitted. In cases where these effects could be included, activation energies changed by less than 2 kcal/mol. We also note that experimental solvents in QD synthesis consist of very low dielectrics. Inclusion of solvent effects[130-131] led to a lowering of activation energies by at most 2 kcal/mol. Tests for basis set superposition errors by computing the counterpoise correction[132] also led to less than 1 kcal/mol corrections on phosphine precursor energetics and were thus omitted.

4.3 Acceleration Approach

In order to accelerate the fruitful sampling and discovery of pathways that lead to formation of InP QDs, we have made a number of careful approximations. We now consider what effect such approximations may have on the predicted mechanism of cluster growth by considering a) the effect of model precursor choice, b) the role of the electronic structure method and basis set size in AIMD, and c) the choice of boundary conditions employed.

4.3.1 Choice of Model Precursors

Long chain indium carboxylates such as indium myristate ($In(My)_3$, 130 atoms) and tris(trimethylsilyl) phosphine ($P(SiMe_3)_3$, 40 atoms) are the most commonly used precursors for the synthesis of InP QDs[5, 24, 49, 55, 87, 133-134] (Figure 4-1). Due to the large size of these experimental precursors, we employ indium acetate ($In(Ac)_3$, 22 atoms) and phosphine (PH_3, 4 atoms) as model molecules (Figure 4-1). Our choice is justified in part by the fact that phosphine has been used as a precursor with $In(My)_3$ to grow InP QDs[135], and previous computational QD studies have often employed acetates to model longer chain carboxylates[136-137]. The speed-up obtained by using the model precursors is substantial: HF/3-21G gradient calculations on $In(Ac)_3$ are about 6 times faster than $In(My)_3$ and on PH_3 are about 100 times faster than $P(SiMe_3)_3$.

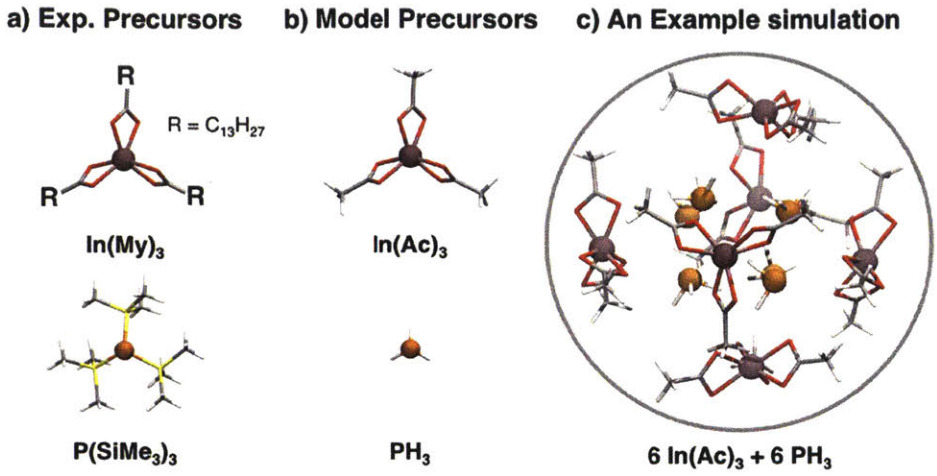

Figure 4-1: (a) Experimental precursors, (b) model precursor analogues used in simulations, and (c) snapshot from example AIMD simulation with spherical boundary depicted. In (brown) and P (orange) atoms are shown as spheres, while other atoms (oxygen in red, silicon in yellow, carbon in gray, and hydrogen in white) are shown in stick representation.

In order to identify whether the simplifications of the model precursors affect the electronic and geometric structures, we compared properties of the simplified molecules with their experimental analogues. For the two indium precursors, identical In or O partial charges and In-O bond distances are obtained regardless of the use of HF/3-21G or B3LYP/LACVP* as the electronic structure method (Table B 3). We investigated whether the steric effect of longer chain carboxylates alters dynamics by carrying out AIMD simulations with bulkier indium trimethyl acetate (In(^{t}BuCOO)$_3$, 49 atoms) and PH_3 precursors. Comparable reaction pathways were observed in AIMD trajectories of In(^{t}BuCOO)$_3$ and In(Ac)$_3$ (Figure B 1).

Unlike the indium precursors, the B3LYP/LACVP* partial charges of phosphorus in PH_3 and P(SiMe$_3$)$_3$ are substantially different,having values of 0.01 *e*- and -0.71 *e*-, respectively. This difference is expected since P and H atoms have comparable electronegativity[138], giving rise to covalent bonding, while the less electronegative Si leads to a partially ionic P-Si bond. The P-H

bond is also 0.86 Å shorter than the P-Si bond, suggesting a stronger interaction between P and H atoms as compared to that between P and the $SiMe_3$ group that is also reflected in the B3LYP/LACVP* bond dissociation energies: 78 kcal/mol for the P-H bond and 62 kcal/mol for the P-Si bond. Nevertheless, AIMD simulations of $In(Ac)_3$ and $P(SiMe_3)_3$ molecules generated analogous intermediates and reaction steps as when PH_3 was used (Figure B 1). Reaction coordinate characterization in this work focuses on PH_3 precursors, but both predicted and calculated differences with respect to $P(SiMe_3)_3$ precursors will be discussed where relevant.

4.3.2 Accelerated *ab initio* molecular dynamics sampling

We have employed a number of strategies to enhance the rate of sampling of reactive collisions between indium and phosphorus precursors. In addition to employing an elevated temperature of 2000 K, we carry out dynamics with a low level of theory and near-minimal basis set combination (i.e., HF/3-21G). The choice of high-temperature was made to accelerate the timescale of observed reaction events in the simulations while preserving qualitative bonding and bond rearrangement that is likely to occur at lower temperatures (e.g., 1000 K), closer to solution chemistry conditions. Snapshots from the dynamics are then refined by B3LYP/LACVP* geometry optimizations and minimum energy path searches. Therefore, the HF/3-21G AIMD sampling only needs to reproduce qualitative changes in bonding consistent with B3LYP/LACVP*. The computational benefit of using HF/3-21G is significant: for an example 156 atom simulation that contains 6 indium precursors carried out in TeraChem on 2 GPUs, HF/3-21G requires about 60 s per MD step while B3LYP/LACVP* requires about 1900 s per MD step. We note that the predominant computational cost in all simulations presented in this work is associated with the electron-rich indium precursors.

It is useful to quantify, however, the extent to which HF, which includes no treatment of dynamic correlation, produces a substantially different description of the electronic structure than a hybrid DFT approach. First, we compare the equilibrium properties of $In(Ac)_3$ and PH_3 precursors (Figure B 2). HF yields shorter In-O and P-H bond distances than B3LYP at the same basis set size by about 0.05 and 0.03 Å, respectively. However, both HF and B3LYP bond distances are reduced when increasing the basis set size from 3-21G to LACVP* by about 0.03 to 0.05 Å, with B3LYP reductions slightly larger than HF. The net result is a cancellation of errors between the underestimation of bond lengths by HF and overestimation from the incomplete basis, leading to agreement within 0.01 Å between HF/3-21G and B3LYP/LACVP* for In-O and P-H bond lengths. Interestingly, partial charges computed with NBO show a similar trend. For the same basis set, HF overpolarizes the In-O bond compared to B3LYP. For a given method, increasing the basis set size leads to larger In-O charge separation, and B3LYP is more sensitive to the increase in basis set size than HF is. The net result is that while the In partial charge with HF/LACVP* of around +2.2 *e*- overestimates the B3LYP/LACVP* In charge by +0.2 *e*-, HF/3-21G and B3LYP/LACVP* partial charges are in quantitative agreement. Similar fortuitous cancellation of errors between basis set incompleteness and absence of treatment of dynamic correlation is apparent in the P atom charges in PH_3. Agreement of vibrational frequencies is also good, as comparison of frequencies for the optimized $In(Ac)_3$ molecule using HF/321G and B3LYP/LACVP* reveals that the absolute mean difference for frequencies larger than 50 cm^{-1} is around 9% (Table B 4). This overall fortuitous error cancellation therefore further motivates sampling AIMD at the HF/3-21G level at around $1/30^{th}$ of the computational cost of a B3LYP/LACVP* calculation.

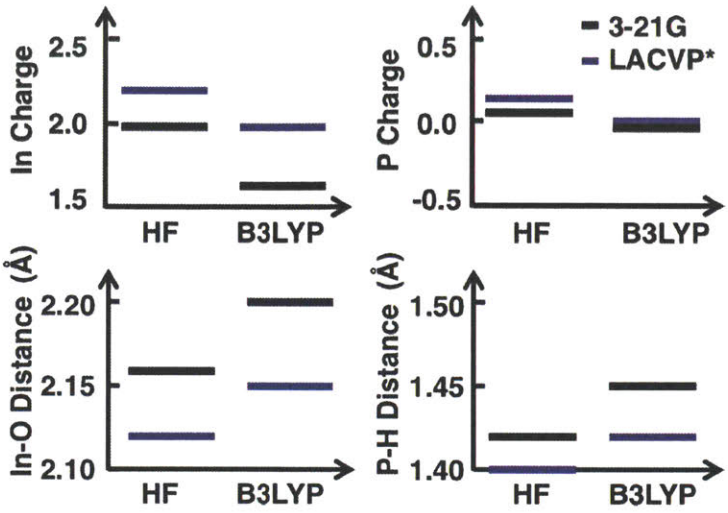

Figure 4-2: Comparison of partial charges (In or P, top) and bond distances (bottom) for $In(Ac)_3$ (left) and PH_3 (right) molecules obtained with Hartree-Fock or DFT (B3LYP) using the 3-21G (black line) or LACVP* (blue line) basis sets.

While equilibrium properties are consistent between HF/3-21G and B3LYP/LACVP*, our ultimate interest is in reproducing dynamics and sampling of reactive intermediates, which necessitates moving away from equilibrium, zero-temperature properties. Parallel AIMD simulations with both HF/3-21G and B3LYP/LACVP* were performed for a system containing one $In(Ac)_3$ and one PH_3 molecule. Nearly identical In-O and P-H radial distribution function peak values and shapes were obtained from the two simulations (Figure B 2). As an even more strenuous test case, at transition-states, basis set superposition errors and static correlation errors can dominate and interfere with the error cancellation. For the formation of an In-P bond from an $In(Ac)_3 \bullet PH_3$ adduct to $In(Ac)_2PH_2 \bullet HAc$, HF/3-21G predicts both a lower barrier (~6 kcal/mol less) and more favorable reaction energy (~13 kcal/mol lower). This discrepancy in barrier heights is not necessarily a disadvantage, as lower barriers for desired reactions will lead to enhanced sampling of reaction events during the AIMD simulation. Regardless, all AIMD

trajectories obtained with HF/3-21G are then quantitatively assessed with B3LYP/LACVP* through geometry optimization and transition state searches.

4.3.3 The choice of boundary conditions

For reaction mechanism discovery involving organic species, it has recently been shown[118] that enforcing spherical boundary conditions that shrink periodically is a useful way to enhance the frequency of collisions during molecular dynamics that lead to chemical transformations. As the chemistry of the systems studied here are quite distinct from small organic molecules, we have tested the extent to which periodically shrinking boundary conditions is a useful strategy to enhance the sampling rate of reactive collisions between indium and phosphorus precursors. In this approach, the key adjustable parameters are the ratio (r_2/r_1) of the smaller radius (r_2) to the larger radius (r_1), the time spent at each radius (t_1 versus t_2), and the harmonic restraint force applied (k_1 versus k_2) to enforce the boundary conditions. We have chosen r_2/r_1 to be around 0.6-0.7 since a tighter r_2 can lead to the unphysical cleavage of C-C and C-H bonds. We note that the shrinking process also slows convergence to self-consistency and increases the time per MD step. For example, in a simulation containing 6 indium precursors and 6 phosphorus precursors, the time per MD step increases by a factor of 1.7 when the smaller boundary is enforced. For the other two parameters, we employ the defaults outlined in Ref. [118], which correspond to t_1=1.5 ps and t_2=0.5 ps and force constants k_1=1.0 kcal/(mol•Å^2) and k_2=0.5 kcal/(mol•Å^2). One further disadvantage of this approach is the loss of direct information about the timescale of events, but since we are already using a lower level of theory (HF/3-21G), direct dynamics timescales already carry limited meaning.

Generally, we have observed different growth intermediates when using different boundary conditions. For example, in two AIMD simulations containing one $In(Ac)_3$ and eight PH_3

molecules (Figure B 3), the use of shrinking boundary conditions leads to the formation of an intermediate species $In(Ac)_2PH_2$ while the use of constant boundary conditions only leads to the formation of an $In(Ac)_3 \bullet PH_3$ adduct. Conversely, in another two AIMD simulations sampling the interaction between three $In(Ac)_3$ and thirty PH_3 precursors, only the intermediate structures such as $[In(Ac)_3]_3$ complexes and $[In(Ac)_3]_3 \bullet PH_3$ adducts were observed in a 15 ps simulation at periodically shrinking boundary conditions without explicit In-P bond formation. Employing constant boundary conditions for the same system leads to the formation of various different intermediates containing stable In-P bonds within 12 ps (Figure 4-3). Although $[In(Ac)_3]_3 \bullet PH_3$ is still observed, further interaction between an acetate and P-H bond within the $[In(Ac)_3]_3 \bullet PH_3$ adduct leads to the first P-H bond dissociation at about 5 ps followed by a second P-H bond dissociation at about 8 ps. Mechanisms and dynamics of In-P bond formation are discussed in detail below. However, these observations highlight the fact that for the more complex inorganic systems we are interested in, an effective sampling strategy must incorporate varying absolute and relative numbers of indium and phosphorus precursors and applying both variable and constant boundary conditions.

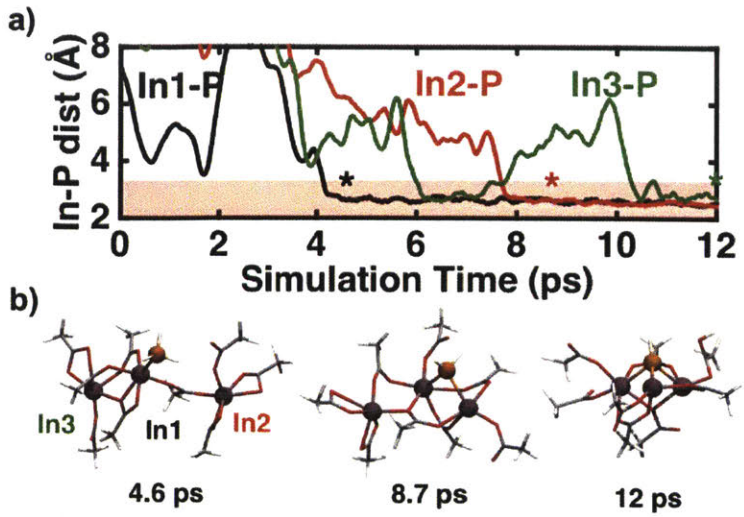

Figure 4-3: (a) Evolution of In-P distances in a constant spherical boundary AIMD trajectory containing one PH_3 and three $In(Ac)_3$ molecules. The distance cutoff for In-P bonding is indicated as a shaded region in the graph. (b) Snapshots of only the reacting molecules from the trajectory at different simulation times as annotated by color-coded asterisk in (a).

4.4 Formation of an InP Cluster

Using high-temperature ab initio molecular dynamics, we directly observe the formation of a small indium-rich InP cluster. Of twenty trajectories in total, this cluster formation is observed in an AIMD simulation that contains six $In(Ac)_3$ and six PH_3 molecules and constant boundary conditions. In this trajectory, overall cleavage of the three P-H bonds in a single PH_3 molecule results in the formation of a cluster with In_4P stoichiometry. While the cluster forms around only one PH_3 molecule, the other five PH_3 molecules rapidly adsorb and desorb from free indium sites. We estimate the maximum lifetime of adduct formation for each of the five PH_3 molecules as ranging from 0.08 to 0.60 ps at 2000 K, during which time the In-P distance is shorter than the previously defined distance cutoff. Four major interactions are observed during the overall cluster formation process: 1) agglomeration of the six $In(Ac)_3$ molecules into an $[In(Ac)_3]_6$

complex; 2) formation of an $[In(Ac)_3]_6 \bullet PH_3$ adduct; 3) dissociation of three P-H bonds concomitant with formation of In-P bonds; and 4) configurational rearrangement of the intermediates and cluster structures. For step 3, P-H bond dissociation is facilitated by nearby acetates of the indium precursors and leads to In-P bond formation. When the acetate that carries out hydrogen abstraction comes from the same precursor as that which is forming the In-P bond, we refer to this event as *intracomplex* P-H bond dissociation. Alternatively, the acetate that carries out hydrogen abstraction may belong to a different indium precursor, which we refer to as *intercomplex* P-H bond dissociation. Energetics for representative steps of each of these processes obtained at the B3LYP/LACVP* level of theory are discussed in detail in Section 4.5

During the overall cluster formation process, the coordination environment of the reacting phosphorus precursor evolves from three hydrogen atoms to four or five indium atoms, as shown in Figure 4-4 (the evolution of In-P and P-H bond distances is available in Figure B 4 and Figure B 5). In the first 4 ps of the high-temperature simulation, both the agglomeration and adduct formation processes occur, leading to significant rearrangement. During agglomeration, the six $In(Ac)_3$ molecules form a C-shaped chain in which individual precursors become linked by bridging carboxylates. Next, an $[In(Ac)_3]_6 \bullet PH_3$ adduct forms with the phosphorus atom weakly bound to an indium atom at one end of the chain, increasing the phosphorus coordination number (CN) from 3 to 4.

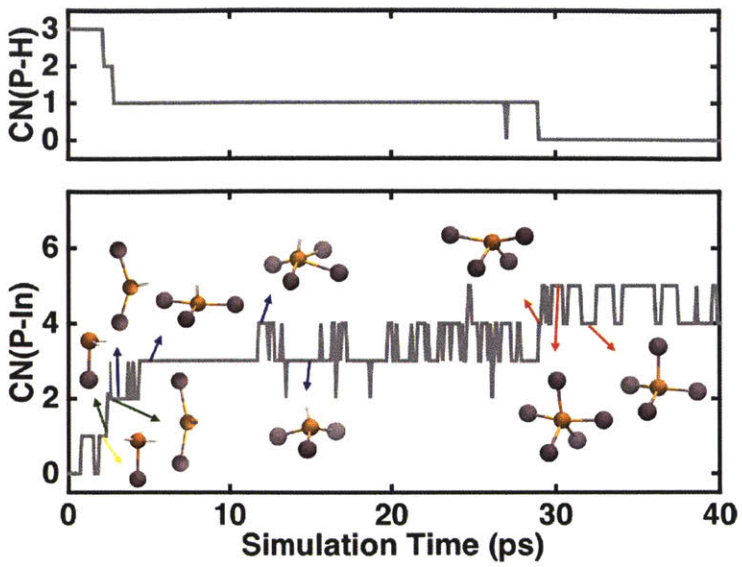

Figure 4-4: (top) Changes in coordination number of P by H and (bottom) P by In during cluster formation in an AIMD trajectory. Coordination numbers are plotted every 0.1 ps. Snapshots showing the phosphorus and the coordinating indium and hydrogen atoms are annotated in inset as indicated by arrows colored by the number of coordinating hydrogen atoms (three: yellow, two: green, one: blue, zero: red).

Next, dissociation of the first and second P-H bonds also occurs within the short 4 ps timeframe. After the adduct formation step, the first P-H bond is dissociated through the intercomplex mechanism, producing an HAc ligand and bringing the phosphorus CN back to 3 (Figure 4-5). This ligand remains bonded to the original indium precursor, but the abstracted proton rapidly transfers to a nearby acetate on the other end of the chain, rendering a new indium center undercoordinated. This second precursor then forms a second bond with the central phosphorus atom, producing a seesaw shaped complex with a central In_2PH_2 unit (H-P-H angle of 98° and In-P-In angle of 163°). At the same time as the In_2PH_2 unit is formed, an acetate on one of the two phosphorus-coordinating indium sites changes from doubly coordinating indium (chelating bidentate) to single, monodentate coordination. This available oxygen anion is then

free to abstract the second hydrogen atom from the central phosphorus (at around 2.7 ps) through the intracomplex pathway (Figure 4-6), leading to a three-coordinated phosphorus bonded with two indium atoms and one remaining hydrogen atom (In_2PH). In the remaining 1.3 ps, the central In_2PH unit evolves from a nearly planar geometry to tetrahedral, with the lone pair on the P atom facing a nearby indium atom that then coordinates the central phosphorus, forming an In_3PH unit at 4.0 ps. Such fast rearrangement suggests that these processes have barriers below k_BT = 4.6 kcal/mol at this level of theory.

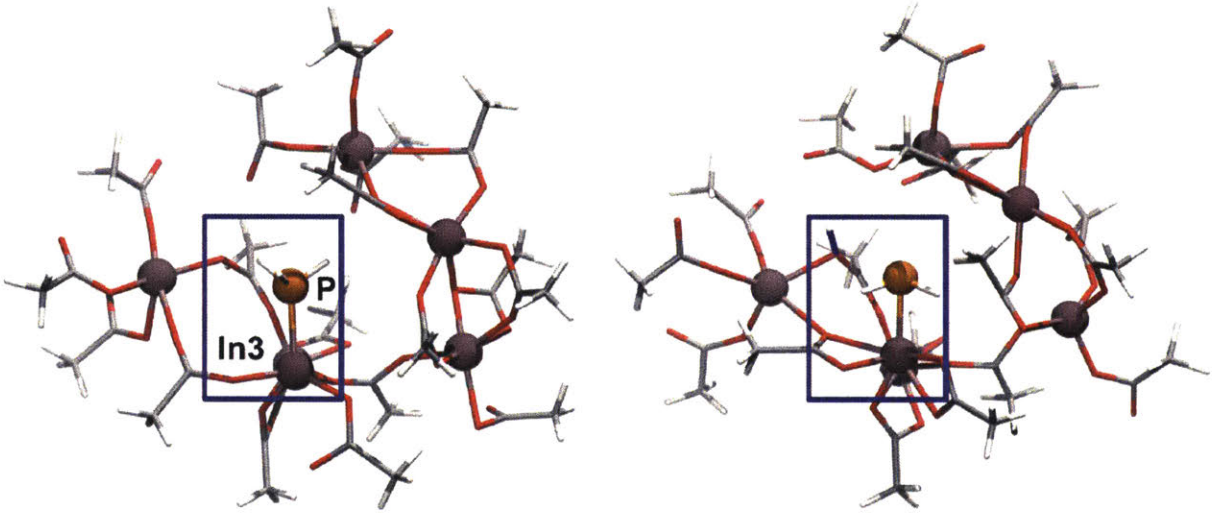

Figure 4-5: Snapshots taken before and after the first P-H bond dissociation.

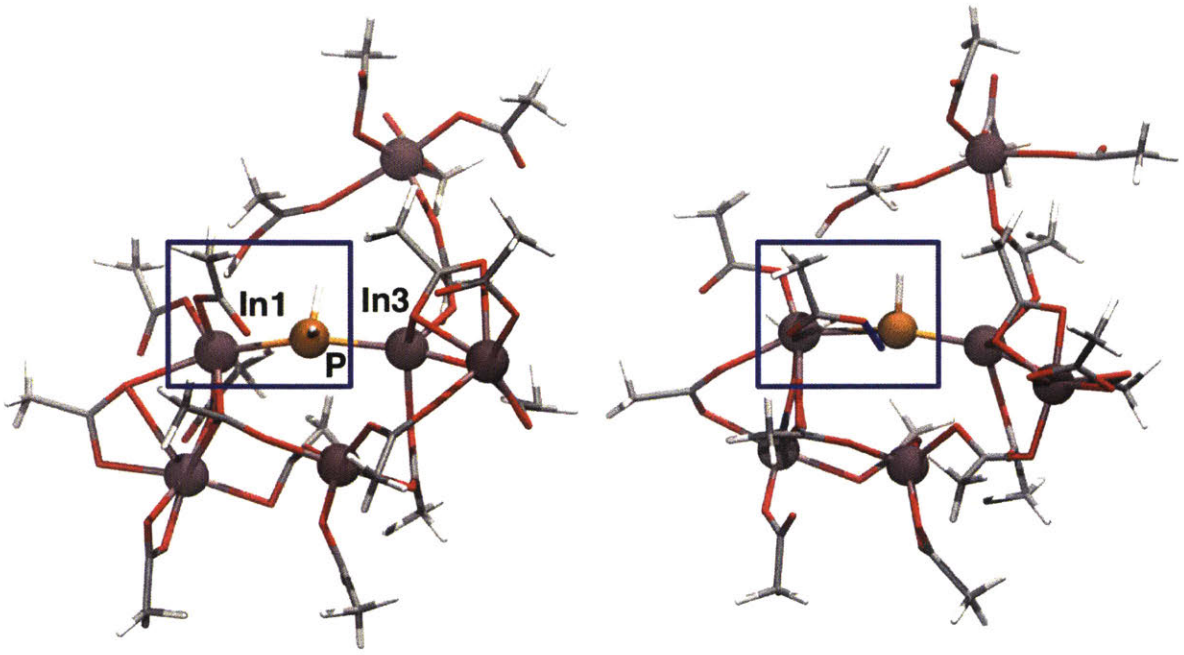

Figure 4-6: Snapshots taken before and after the second P-H bond dissociation.

After such rapid bond rearrangement, much slower rearrangement occurs over the next 25 ps, consisting primarily of slight rearrangement in the configuration of the central phosphorus unit and surrounding agglomerated indium precursors. During this interval, different phosphorus coordination types are observed including In_2PH, In_3PH, In_4PH, In_5PH and In_6PH, with In_3PH being the predominant configuration (around 72% of the time) followed by In_4PH (around 25% of the time). These observations suggest a preference of phosphorus for CNs of 4 or 5. Along with the change of the phosphorus coordination, the two or three unbonded indium atoms gradually move from the side of the In_nPH unit to the top of the unit to form a cage-like structure that surrounds the remaining hydrogen atom (Figure 4-7). An available acetate must mediate the final P-H bond dissociation, but the agglomerated indium rearranges relatively slowly, causing the delay in the third P-H bond cleavage as compared to the first two P-H bond dissociations. We

note, however, that the formation of the cage-like structure is likely only a necessity for phosphine precursors. If $P(SiMe_3)_3$ is instead used as the precursor, the P-Si bond distance is both longer and weaker, making it possible for more distant, intercomplex indium precursors to mediate bond dissociation.

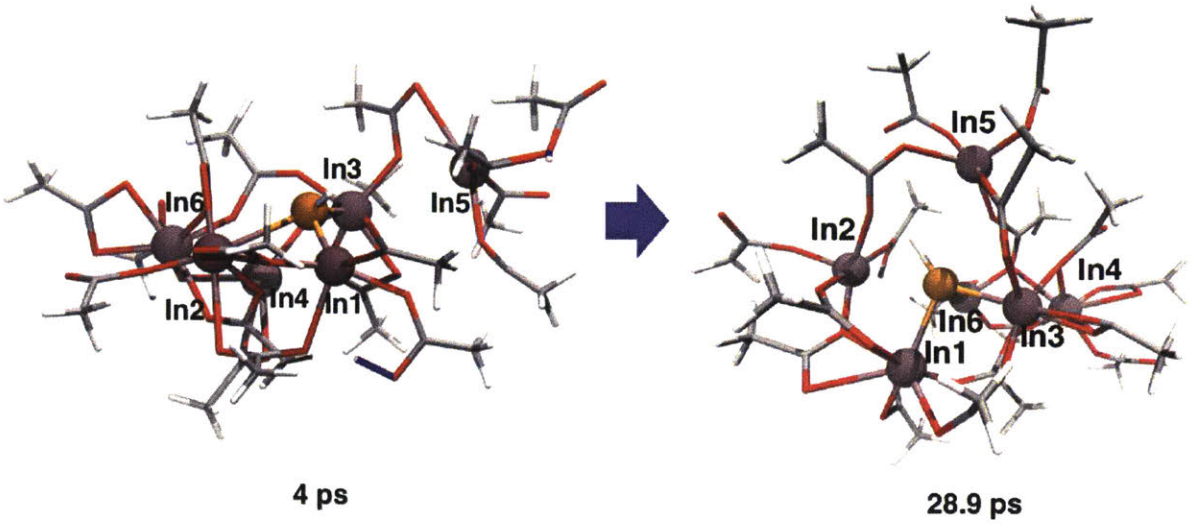

Figure 4-7: Snapshots taken showing the structure rearrangement of the intermediate structures containing one P-H bond.

This third P-H bond dissociation occurs through the intercomplex mechanism at around 28.9 ps (Figure 4-8). The formation of the fourth In-P bond occurs simultaneously with the P-H dissociation process, leading to the formation of a seesaw-geometry In_4P unit. Rearrangement of the cluster geometry is then observed after the dissociation of the third P-H bond until the end of the 40 ps AIMD simulation, with the phosphorus CN dynamically changing between four (~41% probability, approximate tetrahedral geometry) and five (~59% probability, approximate pyramidal or trigonal bipyramidal geometry). The average CN on the phosphorus atom is calculated to be around 4.6, slightly higher than that in the bulk, zinc blende InP crystals (CN = 4) but consistent with previous observations of coordination preference in other InP clusters[139].

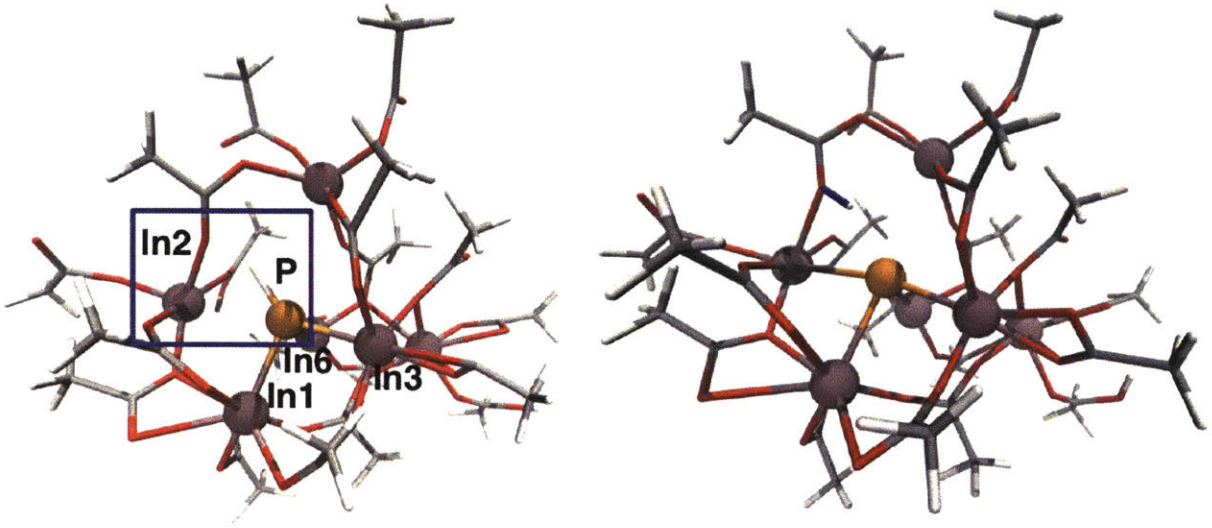

Figure 4-8: Snapshots taken before and after the third P-H bond dissociation.

We analyzed the In-P and In-O radial distribution functions from the last 10 ps of the AIMD trajectory (RDFs, Figure 4-9). The In-P RDF has a first peak at 2.54 Å[140], identical to the experimental value of the In-P distance in bulk, zinc-blende InP crystals. Such good agreement confirms the fortuitous error cancellation observed between the use of HF and the near-minimal basis set with respect to higher-level theory. The In-O radial distribution function has a first peak at 2.12 Å, consistent with the In-O bond distance in an isolated B3LYP/LACVP*-optimized $In(Ac)_3$ molecule.

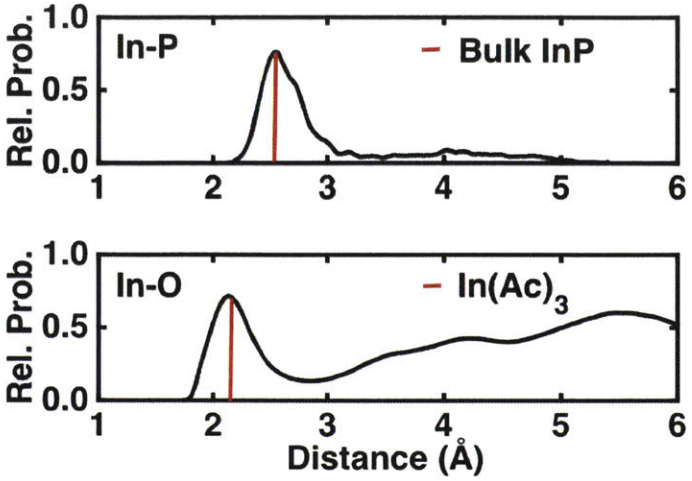

Figure 4-9: In-P (top) and In-O (bottom) radial distribution function based on the last 10 ps of the AIMD simulation containing six $In(Ac)_3$ and six PH_3 molecules. The red line in the top panel indicates the average In-P distance in the bulk crystal and that in the bottom panel indicates the average In-O distance in the bidentate $In(Ac)_3$ molecule optimized at B3LYP-LACVP*.

We obtained a cluster structure by optimizing a snapshot taken at 35 ps in the AIMD simulation with B3LYP/LACVP* (Figure 4-10). This cluster structure has a central, tetrahedral core consisting of one phosphorus atom bonded to four indium atoms (In_4P). The average In-P distance and In-P-In angle of the In_4P unit match closely (within 0.01 Å and 1.2°, respectively) to experimental values for bulk, zinc-blende InP crystals. While additional incorporation of phosphorus in larger clusters may yet cause deviation in bond lengths from the zinc-blende InP structure, good agreement between experimental and theoretical bond lengths and angles for the crystal and the In_4P complex corroborates the choice of theoretical methods employed. In addition to the core structure, two additional $In(Ac)_3$ molecules bond to other indium precursors through four shared, bridging bidentate acetates. Experimentally, the surface of larger InP QDs has been characterized as indium rich[50], and it has been found that an excess amount of indium precursors is beneficial for InP synthesis with indium carboxylate precursors[24]. Our

computational results are both consistent with these experimental observations and suggest for the first time that the agglomeration of indium precursors is necessary for the formation of InP clusters and that clusters are indium rich even during the earliest stages of growth.

a)

b)

PIn_4	d_{In-P} (Å)	$\theta_{In-P-In}$ (°)
Cluster	**2.55**	**108.3**
Crystal (exp.)	**2.54**	**109.5**

Figure 4-10: (a) Structure of a cluster with tetrahedrally In-coordinated phosphorus obtained from geometry optimization of AIMD trajectory cluster (tetrahedron highlighted in yellow). (b) Comparison of average In-P bond distances and In-P-In angles in the cluster and experimental values for zinc blende, crystalline InP.

While the coordination environment around several of the indium atoms changes greatly over the course of the cluster formation process, shifts in B3LYP/LACVP* In partial charges are modest (Figure B 6). In contrast, the phosphorus and hydrogen atom partial charges are initially nearly neutral in phosphine (P: +0.03 *e*- and 3H: -0.03 *e*-) but gain and lose significant electron

density (P: -1.65 e-, 3H: +1.52 e-), respectively, after all P-H bond dissociation steps. Relative charge values are also consistent between both B3LYP/LACVP* and HF/3-21G, in agreement with observations about error cancellation for precursors in this system. During the dissociation of the first P-H bond, the electron density on the P atom increases by 0.52 *e*- while the electron density on the leaving hydrogen atom decreases by 0.51 *e*-. The electron density on the indium atom bonded to the phosphorus atom slightly increases by about 0.09 *e*- (i.e., becomes more neutral) while electron densities on other indium atoms decrease slightly (Table B 5). During the dissociation of the second and third P-H bonds, a similar trend for the charge changes of phosphorus, hydrogen and indium atoms are observed (Table B 6 and Table B 7). These simultaneous and symmetric changes of phosphorus and hydrogen electron densities occur alongside the increase of the P-H bond distances, suggesting the polarization of the P-H bond during the dissociation process (Figure B 7). Less drastic changes of P electron density would likely be observed during the dissociation of a P-Si bond when $P(SiMe_3)_3$ is used as the precursor because the P-Si bond is already more polar than P-H bond, and P charges in $P(SiMe_3)_3$ (-0.71) are closer to the final value in the In_4P cluster (-1.65). Overall, this charge analysis suggests a partially ionic P-H dissociation mechanism mediated by the strongly negative charge localized on the abstracting carboxylate that causes evolution in the electronic structure around the phosphorus precursor but does not significantly affect the indium precursor.

4.5 Characterization of Mechanisms

Following analysis of the HF/3-21G AIMD trajectory that permitted direct observation of cluster formation, we now extract reaction steps sampled across trajectories and analyze energetics of indium agglomeration and In-P bond formation minimum energy pathways at the B3LYP/LACVP* level of theory.

4.5.1 Indium Precursor Agglomeration

Agglomeration of indium precursors ($In(Ac)_3$) to $[In(Ac)_3]_n$ complexes is observed in every AIMD trajectory with more than one indium precursor. During dynamics, complexes are formed through carboxylate ligands that bridge multiple indium atoms. We model the energetics for this agglomeration in the simplest case of two $In(Ac)_3$ molecules forming an $[In(Ac)_3]_2$ complex. In order to identify possible stable intermediates, we ran a 12 ps HF/3-21G AIMD simulation (Figure B 8) and geometry optimized 100 equally spaced snapshots in the last 10 ps with B3LYP/LACVP* (Table B 8). The resulting intermediates are characterized by one to four bridging carboxylates shared between the two indium atoms. Five carboxylate ligand binding modes are observed: i) partial (3%) and ii) full (1%) monodentate (i.e. singly-coordinating indium) that are distinguished by the distance of the non-coordinating oxygen to the indium center; iii) chelating (52%), iv) bridging (31%), and v) chelating, bridging (13%) bidentate (i.e. doubly-coordinating indium), which are distinguished by the extent to which the oxygen atoms strongly coordinate the same indium atom (chelating) or are shared between two indium atoms (bridging) (Figure 4-11). The observed binding modes are consistent with previous experimental and computational studies[50, 136], supporting indium agglomeration in the AIMD trajectories as mechanistically relevant.

When carboxylates bind in a monodentate fashion, the In-O bond is shortened (2.02 Å for partial mode and 1.93 Å for full mode) with respect to the three bidentate modes (2.11-2.26 Å), suggesting higher In-O bond order in monodentate cases. Monodentate modes are also thermodynamically unfavorable with respect to the bidentate binding modes, as suggested by their low occurrence frequencies. For example, the energetic cost of forming a full-monodentate acetate from a chelating-bidentate structure in the isolated precursor ($\Delta E_{FM\text{-}CB}$) is calculated as 21

kcal/mol (Figure 4-12). Notably, the carboxylate chain length has essentially no effect on the In-O bond energy, as $\Delta E_{FM\text{-}CB}$ for the longer chain indium myristate is comparable at about 20 kcal/mol. The value of $\Delta E_{FM\text{-}CB}$ can be reduced in $[In(Ac)_3]_2$ complexes (as low as 15 kcal/mol) due to the stabilization offered from the bridging acetates (Figure B 10). Further stabilization of monodentate carboxylates is likely in larger agglomerated complexes, as we previously noted several monodentate species that formed dynamically during the high-temperature AIMD simulations.

a)

2.16 Å	2.02 Å	1.93 Å	2.11 Å	2.26 Å
52%	3%	1%	31%	13%
Chelating Bidentate	Partial Monodentate	Full Monodentate	Bridging Bidentate	Chelating Bridging Bidentate

b)

$[In(Ac)_3]_2$	No. of Bridging Acetates				
	0	1	2	3	4
ΔE_{bridge}	0	-2±2	-14±1	-13±2	-18±4

Figure 4-11: (a) Indium-carboxylate coordination modes obtained from optimized structures of MD-sampled $[In(Ac)_3]_2$ complexes annotated with average In-O distance and frequency of occurrence. (b) Relative energies of chelating bridging bidentate or bridging bidentate $[In(Ac)_3]_2$ complex structures with increasing numbers of bridging bidentate ligands.

As the number of bridging ligands between In centers increases, the formation energy of the $[In(Ac)_3]_2$ complex becomes increasingly favorable. While a single bridging acetate ligand is only favorable by -2 ± 2 kcal/mol, the energetic benefit increases to -18 ± 4 kcal/mol for four bridging acetates (Figure 4-11). Ranges in energetics here are obtained from the small variations in 100 geometry-optimized snapshots. We have also computed energetic barriers for the

sequential formation of bridging ligands. The initial agglomeration of two indium precursors to form a complex with one to three bridging acetates has a low activation energy (0-3 kcal/mol), while the barrier for adding a fourth bridging acetate to the complex is calculated to be 6 kcal/mol (Figure B 11). The higher barrier due to formation of the fourth bridging interaction is largely due to the fact that the three-bridge structure is more stable than the four-bridge structure by about 2 kcal/mol (i.e. the reverse barrier for transitioning from four- to three-bridge structures is only 4 kcal/mol). In each step, the new acetate bridge forms by orienting toward the neighboring indium atom in a position compatible with bonding followed by shortening of the second indium-oxygen bond.

Overall, observations of both energetically favorable and low-barrier rearrangement for agglomeration through bridging interactions supports our previous observations of dynamic indium agglomeration during cluster formation. We note, however, that indium precursors employed during experimental synthesis (e.g., indium myristate) may be less likely to form the highly-interconnected four-bridge structures due to steric repulsion of the long alkyl chains. Importantly, the observation of the reduction in energetic penalty for monodentate indium-carboxylate ligands with increasing agglomeration is likely preserved even in the case of long chains. This result suggests that agglomeration of the indium precursor may facilitate creation of indium sites available for forming In-P bonds.

4.5.2 Formation of In-P Bonds

In addition to indium precursor agglomeration, AIMD sampling of mixtures of $In(Ac)_3$ and PH_3 precursors reveals multiple modes of In-P bond formation. In all cases, PH_3 molecules first weakly associate with individual $In(Ac)_3$ or complexed $[In(Ac)_3]_n$ precursors to form $In(Ac)_3 \bullet PH_3$ or $[In(Ac)_3]_n \bullet PH_3$ adducts. We previously noted that this weak interaction was

characterized during dynamics by relatively short, sub-ps lifetimes. For stable In-P bond formation to occur, P-H bond dissociation must occur. When the In-P bond formation and P-H bond cleavage is mediated by a carboxylate coordinated to the indium forming the In-P bond, this process is called *intracomplex*, while we refer to the process as *intercomplex* when the acetate is coordinated to a different indium precursor (Scheme 4-1). We now examine possible mechanistically relevant differences in the energetics between the two types of P-H bond dissociation pathways.

Scheme 4-1: (a) Intracomplex P-H bond dissociation mechanism with $In(Ac)_3$ or $[In(Ac)_3]_2$ both participating in the In-P bond formation and carrying out H abstraction. (b) Intercomplex P-H bond dissociation mechanism in which a second $In(Ac)_3$ carries out the H abstraction.

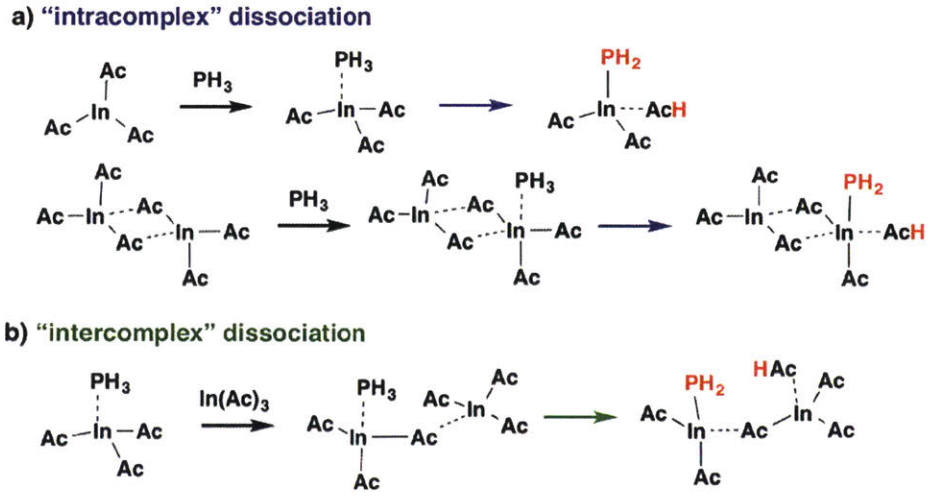

Intracomplex pathway. We first consider the formation of an $In(Ac)_3 \bullet PH_3$ adduct and subsequent intracomplex P-H bond dissociation (Figure B 12 and Figure 4-12). The optimized $In(Ac)_3 \bullet PH_3$ adduct has an In-P distance of 3.69 Å, confirming the weak interaction between In and P observed in AIMD trajectories. Following the barrierless adduct formation, one of the In-O bonds breaks ($d_{In\text{-}O}$=3.65 Å) and the uncoordinated oxygen abstracts a proton from PH_3 to form an In-P bond ($d_{In\text{-}P}$=2.61 Å). The In-O and In-P bond distances closely resemble their values in

the product of 3.77 Å and 2.55 Å respectively, which would initially suggest the formation of a late transition state. However, the transferring proton is shared between phosphorus and oxygen (d_{P-H}=1.62 Å, d_{O-H}=1.34 Å) in the transition state (Table B 9). The activation energy for the In-P bond formation process is 21 kcal/mol, which is the same as the energy penalty to form a full-monodentate acetate from a chelating-bidentate acetate in $In(Ac)_3$.

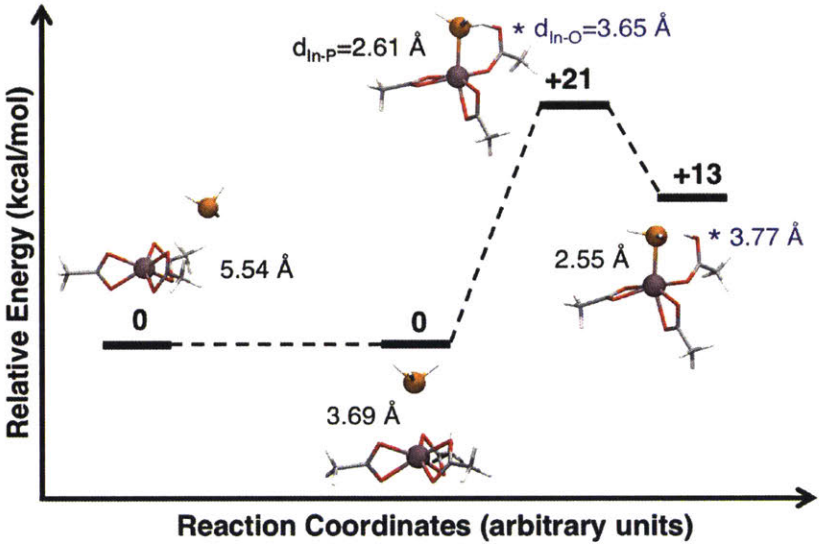

Figure 4-12: Energetics and structures of the intracomplex pathway with one $In(Ac)_3$ and one PH_3 molecule for In-P bond formation. Indium-phosphorus distances are shown in black and indium-oxygen distances are shown in blue for the unbonded oxygen that is denoted with a blue asterisk.

Since the energetic cost of forming monodentate acetates is lowered in agglomerated indium precursors, we computed the energetics of an intracomplex pathway using a two-bridge $[In(Ac)_3]_2$ complex (Figure 4-13 and Figure B 13). Here, we observe an adduct with a shorter In-P bond (2.85 Å) that is mediated by partial lengthening of one of the indium-acetate oxygen bonds (3.01 Å). The process of forming the $[In(Ac)_3]_2 \bullet PH_3$ adduct destabilizes the uncoordinated oxygen, requiring 5 kcal/mol. After the adduct formation, the destabilized oxygen further

dissociates from indium (d_{In-O}=3.68 Å) in order to abstract a proton from the associated phosphine, with a barrier of 15 kcal/mol. The overall barriers for the process are 20 kcal/mol, yielding no net energetic benefit of agglomeration on the activation energy for In-P bond formation in this case. However, we did observe during dynamics that agglomeration of larger numbers of indium precursor copies increased the likelihood of dynamic formation of monodentate acetates. Further analysis in this case reveals that although monodentate mode is more stabilized in the $[In(Ac)_3]_2$ complex, the proton affinity of the uncoordinated oxygen in the $[In(Ac)_3]_2$ complex is lowered as compared to $In(Ac)_3$ (Table B 10). The cancellation of these two effects produces comparable activation energies and transition state structures for the two intracomplex dissociation processes. Notably, in both cases, In-O and In-P bond distances more closely resemble the products than the adduct distances, but the transferring hydrogen is located symmetrically between P and O (Table B 9).

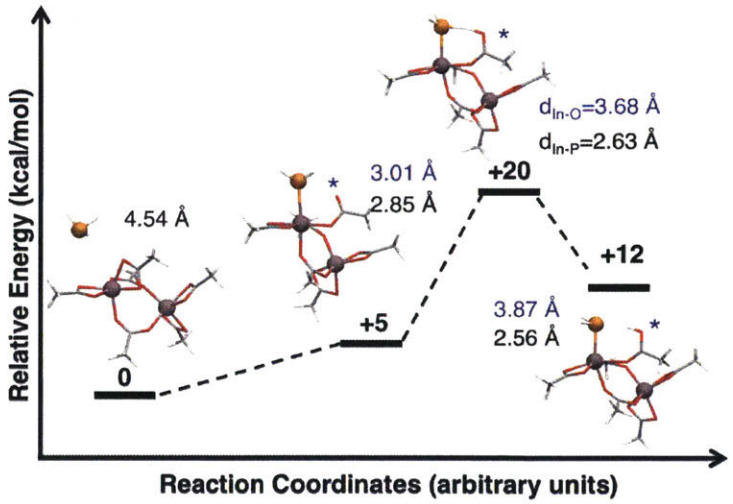

Figure 4-13: Energetics and structures of the intracomplex pathway between a $[In(Ac)_3]_2$ complex and one PH_3 molecule for In-P bond formation. Indium-phosphorus distances are shown in black and indium-oxygen distances are shown in blue for the unbonded oxygen that is denoted with a blue asterisk.

Intercomplex pathway. We modeled the intercomplex pathway using one $In(Ac)_3 \bullet PH_3$ adduct and a separated $In(Ac)_3$ precursor for comparison with the intracomplex pathway (Figure B 14 and Figure 4-14). The formation of a bridging acetate between the adduct and $In(Ac)_3$ has a reaction barrier of 4 kcal/mol due to the partial dissociation of an In-O bond to form a bridging-bidentate acetate. The subsequent P-H bond dissociation is facilitated by the cleavage of another In-O bond in the nearby $In(Ac)_3$, after which the uncoordinated oxygen abstracts a hydrogen atom from PH_3, leading to the formation of an In-P bond. The transition state is characterized by a 0.5 Å shorter distance between indium and the under-coordinated oxygen (d_{In-O}=3.2 Å) than that in the corresponding transition state from the intracomplex pathway, although P-H and O-H distances are comparable (Table B 9). The shorter In-O bond distance lowers the activation energy by 7 kcal/mol with respect to the intracomplex pathway. This relationship between distance and relative energetics agrees well with the evaluated In-O bond distance dependence of energetics in isolated $In(Ac)_3$ molecule where a configuration with a 3.2 Å In-O bond is 5 kcal/mol lower in energy than one with a 3.7 Å In-O bond (Figure B 9). The favorable geometry afforded in this intercomplex pathway calculation implicates the dominance of intercomplex pathways over the intracomplex pathway, consistent with AIMD trajectories in which the majority of In-P bond formation steps occurred through the intercomplex pathway. This observation also highlights the important role of bridging coordination modes to both stabilize indium while predisposing an oxygen atom toward proton abstraction from the phosphorus precursor.

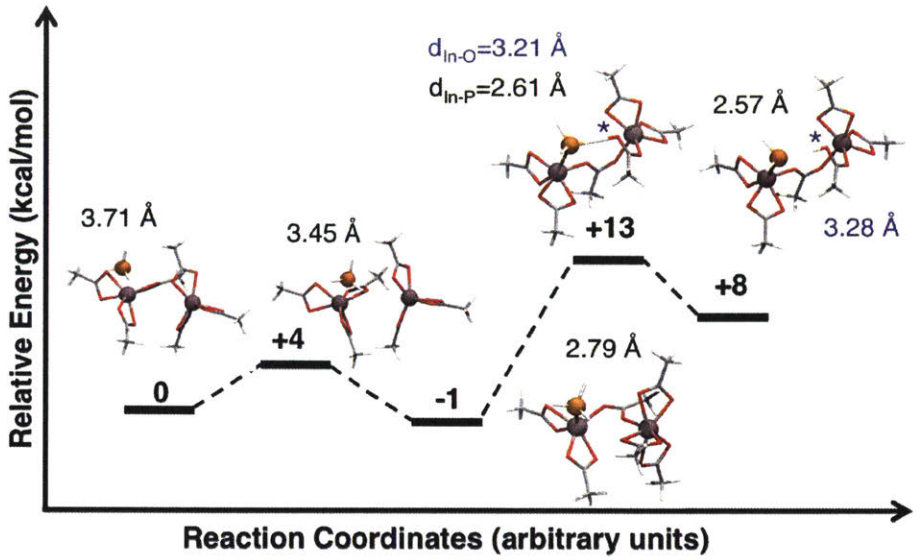

Figure 4-14: Energetics and structures of the intercomplex pathway for In-P bond formation. Indium-phosphorus distances are shown in black and indium-oxygen distances are shown in blue for the unbonded oxygen that is denoted with a blue asterisk.

We have noted that In-P bond formation and P-H dissociation pathways have energy barriers corresponding roughly to the energetic cost of forming a monodentate acetate on an indium precursor. Therefore, starting from an indium precursor structure with pre-formed monodentate acetates should lower the energy barrier for the formation of In-P bonds. We designed a new intracomplex pathway starting with a full-monodentate $In(Ac)_3$ and PH_3 molecule (Figure B 15 and Figure B 16) and confirmed that the barrier of new pathway is calculated to be 5 kcal/mol. Although the reaction barrier is lowered, we have simply shifted the cost to form a full-monodentate $In(Ac)_3$ away from the P-H dissociation transition state and have not reduced the overall steepness of the reaction landscape. However, dynamic formation of monodentate acetates is likely under experimental conditions, particularly if ligands are designed that stabilize the process of forming undercoordinated indium species by shifting the relative energetics of bidentate and monodentate binding modes.

Since the experimental phosphorus precursor ($P(SiMe_3)_3$) has different geometric and electronic properties than PH_3, we expect that these differences should affect In-P bond formation energetics (Figure B 17 and Figure B 18). Here, the adduct formation is again barrierless. However, the In-P distance (2.75 Å) is 0.94 Å shorter in this adduct than in $In(Ac)_3 \bullet PH_3$ due to the additional hydrogen bonding interactions between methyl groups of $P(SiMe_3)_3$ and indium precursor acetate ligands (Figure B 19). As a result, the formation of the In-P bond not only requires the cleavage of an In-O bond but also disrupts some of the favorable hydrogen bonding interactions. The loss of these hydrogen bonding interactions explains why a higher estimate of the activation energy (27 kcal/mol) is observed for the larger precursor, despite the lower bond dissociation energy of the P-Si bond. We have not computed the energetics of the intercomplex pathway due to computational cost and large number of soft degrees of freedom, but we expect that the reaction energy will be significantly lowered both due to the lower activation energy for that pathway compared with phosphine and due to the preservation of favorable hydrogen bonding interactions. While In-P bond formation with phosphine precursors was endothermic by 13 kcal/mol, it becomes exothermic by 5 kcal/mol for $P(SiMe_3)_3$ precursors, consistent with differences in the bond dissociation energy of the P-H and P-Si bonds in the two molecules. A clear mechanistic picture emerges that the phosphorus-ligand bond in the phosphorus precursor controls reaction thermodynamics for In-P bond formation, while the indium-ligand bond controls the activation energy, and thus kinetics, for the process. Thus, while experimental efforts to tune InP QD synthesis have focused on phosphorus precursor chemistry without significant effect on quality of QDs, a concerted effort that tunes both indium and phosphorus precursors is likely necessary.

4.6 Conclusion

In this chapter, we have presented a computational approach for the sampling and discovery of reactive intermediates that form during early stage growth of indium phosphide quantum dots. As the structure of intermediates were previously unknown, we undertook a number of efforts to ensure sampling of possible favorable configurations over a total of 330 ps of AIMD on systems up to 277 atoms in size. This acceleration strategy included the use of GPU-accelerated quantum chemistry employed without explicit dynamic correlation (i.e. Hartree-Fock) and in a near-minimal basis set (3-21G). Opposing effects of inclusion of dynamic correlation (i.e. with the hybrid functional B3LYP) and a larger LACVP* polarized basis set led to fortuitous error cancellation that imparted excellent agreement between HF/3-21G and B3LYP/LACVP* geometric and electronic structure, allowing us to directly sample dynamics at $1/30^{th}$ of the computational cost of a production-quality DFT calculation. Additionally, we employed variable boundary conditions in order to enhance diversity and number of reactive collisions that were sampled in our high-temperature molecular dynamics.

Our sampling strategy enabled us to directly observe the formation of an indium-rich In_4P cluster that already possesses the same structural properties as the experimental bulk zinc-blende crystal structure of indium phosphide. Our indium rich cluster is consistent with experimental characterization of larger InP QDs, and we demonstrate for the first time that an indium-rich surface is likely present from the earliest stages of growth. While only indium phosphide was considered in this work, the mechanistic insights we observed are likely also relevant to the growth of other phosphide materials, such as Zn_3P_2, which has been shown experimentally[141] to form Zn-rich clusters. During the 40 ps cluster formation trajectory, we observed rapid agglomeration of indium precursors around a single phosphorus precursor. In these simulations,

cluster formation was mediated by cooperative effects, which we refer to as an intercomplex pathway, in which one indium precursor formed a bond with the phosphorus center while another abstracted a proton from phosphine. We then characterized the minimum energy pathways of key processes observed in dynamics and confirmed that intercomplex pathways for In-P bond formation was also found to be more energetically favorable than the intracomplex pathway due to stabilization of the indium-acetate oxygen during the proton abstraction process.

Overall, we consistently observed that the highest barriers to In-P bond formation were exclusively determined by energetic penalties associated with indium-carboxylate bond cleavage. The net favorability of the reaction, on the other hand, was determined by the nature of the phosphorus precursor (e.g. PH_3 or $P(SiMe_3)_3$). These observations challenge the paradigm that a single precursor may be tuned in order to optimize the target size distribution of InP QDs. Altering the stability of agglomerated and monodentate indium precursor structures will adjust the energy landscape for In-P bond formation, while tuning phosphorus precursor chemistry can alter how much heat is generated during the QD synthesis process by the downhill nature of the precursor reaction. In the future, a greater focus on tuning the chemistry of indium precursors should enhance the quality of InP QDs with desired size distribution and enable the growth of the use of InP QDs in a wide range of consumer applications.

Chapter 5

Cluster-Mediated Growth of Indium Phosphide Quantum Dots

5.1 Introduction

First principles approaches have provided insights on the early-stage growth of InP QDs from precursors to small clusters. It was found that the early stage interaction between precursors produces indium-rich InP clusters. Different roles of precursors are identified with the indium precursors controlling the thermodynamics and the phosphorus precursors determining the reaction kinetics. In order to fully understand the whole growth behavior of InP QDs, it is also essential to study the transformation of clusters formed after the precursor reactions. As the number of atoms in clusters already exceeds the affordability of *ab initio* computational studies, experimental approaches are applied in this chapter to explore the growth from early stage clusters to final nanocrystals. Meanwhile, as a validation of the *ab initio* study, experimental demonstration of the formation of clusters during the precursor reaction is also necessary. As will be seen, we have employed various characterization tools including absorbance and mass measurement to probe the formation of clusters and their roles during the formation of large nanocrystals. As the use of absorbance measurement to capture the cluster/QD growth trajectory is straightforward, we have undertaken a number of efforts to construct an integrated one-solvent

and air-free protocol to enable the mass measurement of InP growth mixtures. Our results show that small InP clusters are formed right at the beginning of the synthesis and medium InP clusters remain present throughout the entire process, thus acting as a reservoir for QD growth.

In this chapter, I will first present our experimental observation of small cluster formation during early-stage growth. Then I will motivate the use of matrix-assisted laser desorption and ionization (MALDI) mass spectrometry (MS) to probe the role of clusters during the QD formation. I will also provide our results on the late-stage InP growth mixture characterization using both absorbance measurement and MALDI MS.

5.2 Absorbance Characterization of InP Clusters/QDs

After mixing both indium and phosphorus precursors for about 6 min at room temperature, we observed the early-stage intermediates with a first absorption peak around 320 nm according to the absorbance measurement (Figure 5-1). The distinct first absorption peak suggests the formation of small InP clusters upon the precursor interaction. It is also found that excess indium precursors are required for the observation of this distinct absorption peak, with a sharper peak obtained by a greater amount of indium. The indium-dependent cluster formation is consistent with our AIMD simulation wherein indium-rich InP clusters are formed. The formation of these clusters is independent of the reactor (chip, tube or batch), the indium carboxylate precursor, and the solvent (Figure C 1). The increase of growth temperature destabilizes the 320 nm clusters and transforms them to larger intermediate clusters with their first absorption peaks around 360 nm.

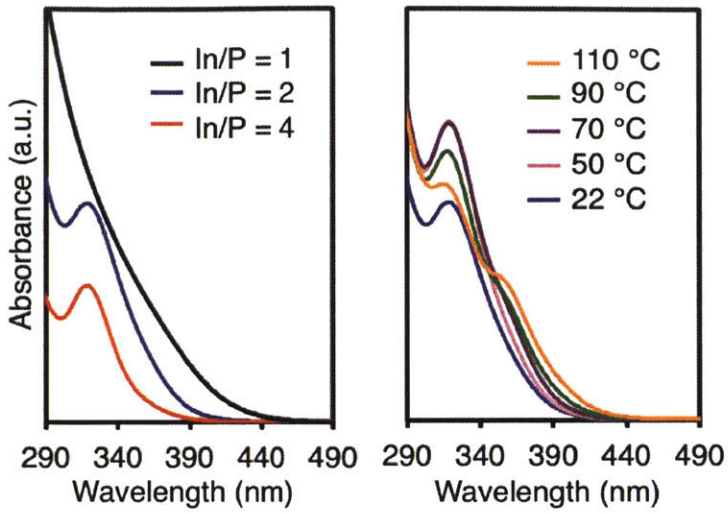

Figure 5-1: Left: Absorbance characterization of InP clusters synthesized with different indium and phosphorus ratios in a one-stage chip reactor. The temperature is set as 22 °C. Right: Absorbance characterization of InP growth mixtures synthesized at different growth temperatures in a one-stage chip reactor. The In and P ratio is set as 2. For all the experiments, the total flow rate is set as 60 μL/min. Toluene is used as the solvent. 4 vol% TOP is added into the indium precursors to dissolve them in the solvent.

The absorption peak at 320 nm disappears with the increase of growth temperature, and cluster mixtures with two absorption peaks around 360 and 380 nm show up in the absorbance spectra (Figure 5-2). Clusters with the 360 nm peak remain in the spectra with the temperature increase, while clusters with the 380 nm absorption peak grow larger to become QDs. At 180 °C, despite the formation of QDs with their first absorption peak around 490 nm, the 360 nm absorption feature is still obvious. As the QD first absorption features become stronger with the increasing QD concentration, the 360 nm absorption features become invisible (e.g., at 210 °C). The same phenomenon was observed for syntheses at different growth times at different growth temperatures (Figure C 2). Two possibilities exist to explain the disappearance of the signal of

360 nm clusters: (1) these clusters have been fully consumed to QDs; or (2) the absorption features of these clusters are covered but they still exist in the growth solution. These two different possibilities correspond to two transformation pathways of these clusters, respectively. (1) "Secondary nucleation": these clusters fully decompose at higher temperatures to molecular species, which contribute to the further growth of QDs; (2) "a continuous supply": these clusters act as a reservoir for the growth of large nanocrystals until they are fully consumed. To elucidate the role of these clusters, absorbance measurement are not adequate, and new characterization methods are needed to capture the existence of both clusters and QDs.

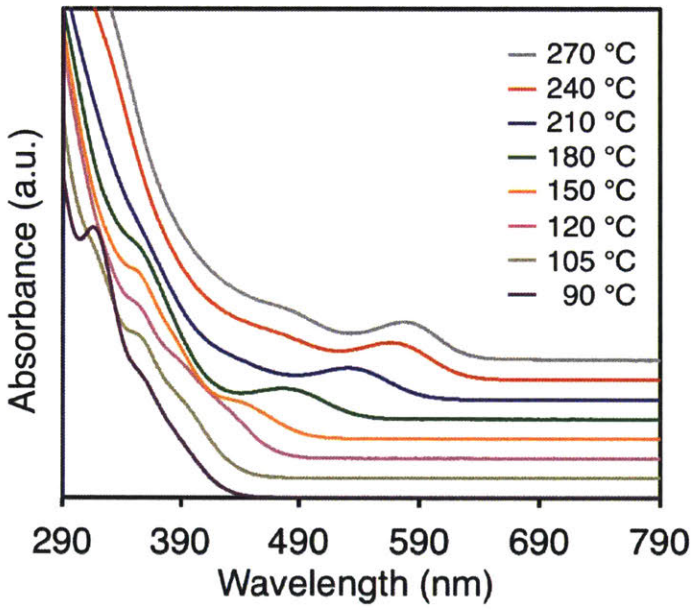

Figure 5-2: UV-Vis spectra of InP growth trajectories synthesized at different temperatures in the tube reactor. For all the experiments, the total flow rate is set as 40 μL/min. The In and P ratio is set as 2. Toluene is used as the solvent. 4 vol% TOP is added into the indium precursors to dissolve them in the solvent.

5.3 MALDI Characterization of InP Clusters/QDs

Historically, absorbance measurements have been employed to monitor the growth of InP QDs. In our study, we have also employed absorbance to capture the growth of InP clusters/QDs from precursors. However, as QDs possess larger absorption cross sections,[142-144] it is challenging to uncover the existence of clusters when QDs are also present, in particular at the late stage of growth when the QD concentration is high. Their small size, close to 1 nm,[47, 88] also makes clusters difficult to observe by other available methods such as high resolution transmission electron microscopy (HR-TEM), dynamic light scattering (DLS), and small-angle X-ray scattering (SAXS). Yet, to gain insights into InP QD growth from clusters, it is crucial to characterize cluster intermediates during nanocrystal formation.

As a soft ionization technique, matrix-assisted laser desorption/ionization time of flight (MALDI-TOF) mass spectrometry (MS) has been applied to studies of Au nanoclusters,[145-146] metal oxide nanoparticles,[147-148] ZnS,[149] CdS,[150] and CdTe[151] nanoparticles. It has also been used to characterize non-classical growth mechanisms of inorganic nanoparticles.[152-153] MALDI MS requires samples to be co-crystallized with a matrix in a solid form. Since QD batch syntheses commonly utilize ligands or solvents with high boiling points, these non-volatile impurities need to be completely removed in order to meet the MALDI vacuum requirements. In a typical QD purification process, polar solvents are added into the non-polar growth solution to precipitate out the nanoparticles, during which the chemical identity of the surface QD atoms and/or surface ligands may be altered; or smaller clusters may be removed from the final solution.[154-156] Moreover, InP cluster/QD surfaces are very sensitive to oxidation, especially when exposed to air.[50] These surface changes may affect the mass data and pose challenges to directly applying MALDI MS in characterizing InP growth intermediates. Here we present an air-free, one-solvent

method that allows us to synthesize InP QDs in a microfluidic reactor, to purify the resulting samples without precipitation, and to simultaneously track the formation of larger QDs and the consumption of smaller clusters via MALDI MS.

In our integrated approach, toluene is used as the solvent for synthesis, purification, and matrix preparation (Figure 5-3). Syntheses of InP growth intermediates are performed in HT and HP microchemical systems under inert conditions (Figure C 3). Purification of the intermediates is achieved by gel permeation chromatography (GPC) in a glove box. GPC has been demonstrated to effectively remove unreacted precursors, ligands, and side products from QD growth solutions without perturbing the ligand-binding environment.[157-158] Moreover, both clusters and QDs elute out from the GPC column at the same time, and therefore, they are preserved together in the purified solution. The absorption spectra of both clusters and QDs remain unchanged after GPC purification (Figure C 4). ^{1}H and ^{31}P NMR spectra[159] before and after GPC purification show the effective removal of impurities and weakly associated ligands in the growth solution (Figure C 5 and Figure C 6). The one-solvent and air-free synthesis and purification allow us to obtain oxygen-free QDs for further mass characterization (Figure C 7). Trans-2-[3-(4-tert-Butylphenyl)-2-methyl-2-propenylidene]malononitrile (DCTB), a common MALDI matrix for metal clusters and nanoparticles,[146] is added to the purified InP-toluene solution. The InP-DCTB-toluene mixture is then spotted and dried on a MALDI plate in a glove box.

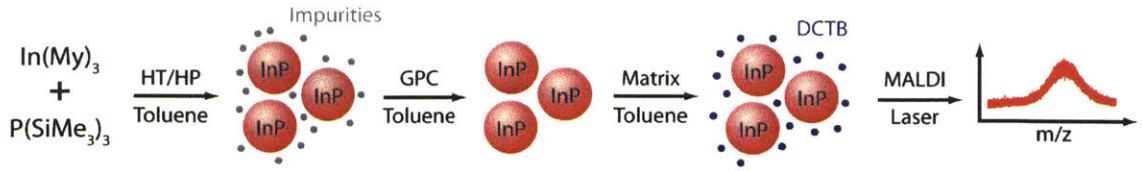

Figure 5-3: An integrated air-free approach to characterize InP growth mixtures using MALDI MS.

To assure the accuracy of the mass characterization, at low mass range, tripsinogen was used as the external standard (11999 and 23981 Da) to calibrate the spectrometer. At high mass range, albumin (bovine serum, BSA) was used as the external standard (33216 and 66431 Da) for the calibration. As the MALDI spectrometer (Bruker Microflex) utilizes a nitrogen laser (337 nm, 3.69 eV) to desorb and ionize the matrix from the MALDI plate, we also studied the effect of laser power on the stability of InP growth mixtures (Figure 5-4). InP clusters exhibit similar mass peaks upon lasing for the whole range we have investigated, which is typically below 50% of the instrument setting. However, the mass peaks of QDs only remain unchanged upon lasing at low laser powers (30-40%). We characterized the mass spectra of clusters and QDs below 7 kDa, and observed fragment signals (Figure C 8). The mass loss of the clusters upon lasing is possibly due to the removal of excess indium myristate precursors on the QD surfaces upon heating. The mass loss of QDs is attributed to the deconstruction of InP bonds, as the In-P bond dissociation energy is only about 2.05 eV. To minimize the mass loss of clusters and QDs and also to obtain a reasonable mass intensity, the laser intensity was set between 20-30% for cluster characterization and between 30-40% for QD characterization. The observed mass loss of QDs motivates us to do a systematic study on the accuracy and resolution of MALDI mass characterization.

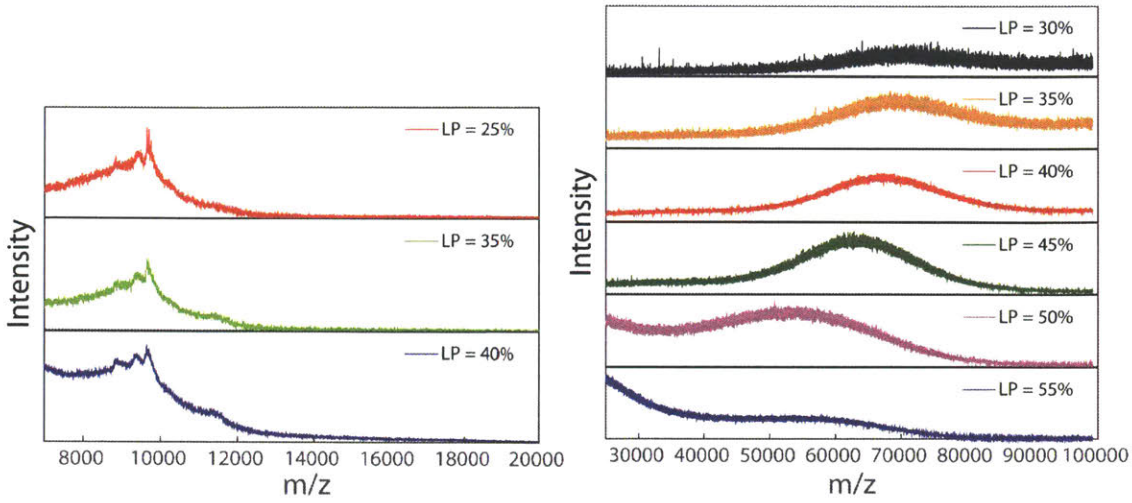

Figure 5-4: (Left) Cluster stability and (Right) QD stability upon MALDI lasing at different lasing powers (LP) set in the MALDI instrument.

We validated the mass accuracy and resolution of MALDI MS in characterizing InP QDs. To check the MALDI resolution, we compared the mass results of four similar QD samples with their absorbance measurement (Figure 5-5). As the UV-Vis spectra show, the four samples have slightly different first absorption peak locations and peak line widths. The mass distribution and peaks obtained from MALDI correspond to UV-Vis absorbance data, capturing the change of size and size distribution of QDs with high resolution.

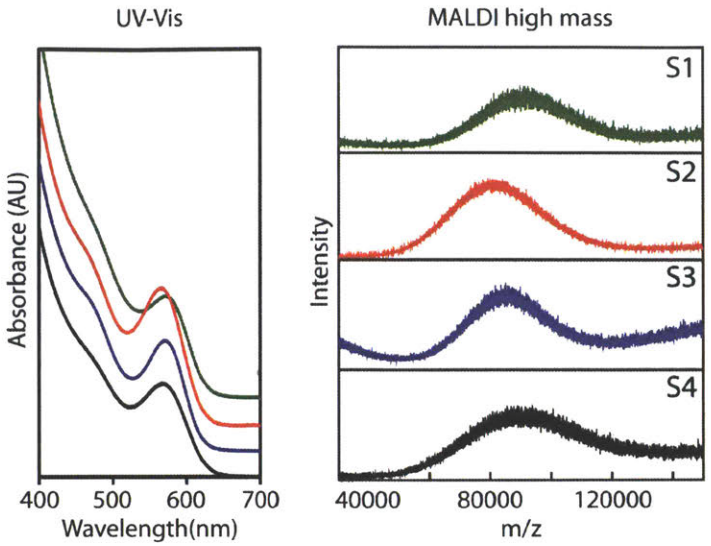

Figure 5-5: Comparison of UV-Vis (left) and MALDI (right) resolution in characterizing the size and size distribution of four different QD samples.

To check the MALDI accuracy, we compared the mass-derived sizes of two QD samples with those obtained from STEM imaging analysis (Figure 5-6 and Figure C 9). The two QD samples have first absorption peaks at 520 and 580 nm and are confirmed to be cluster-free. The general protocol is as follows (detailed calculation available in Appendix D): the purified QDs are first characterized by ^{1}H and ^{31}P NMR to show that myristate is the only organic ligand species bond to the QDs. The inorganic core mass can then be obtained by subtracting the myristate mass from the particle mass. The volume of the inorganic core is obtained by assuming that its density is the same as that of bulk InP crystal. Since InP QDs have been observed in both nearly spherical (S) and tetrahedral (T) shapes,[38,47,157] the projected area corresponding to either shape is calculated from the volume of the inorganic core and compared with that obtained from STEM-HAADF analysis. While MALDI MS is known to cause the possible fragmentation of CdSe nanoparticles,[160-161] good agreement is achieved between MALDI and STEM characterization, confirming the accuracy of MALDI in determining InP QD mass.

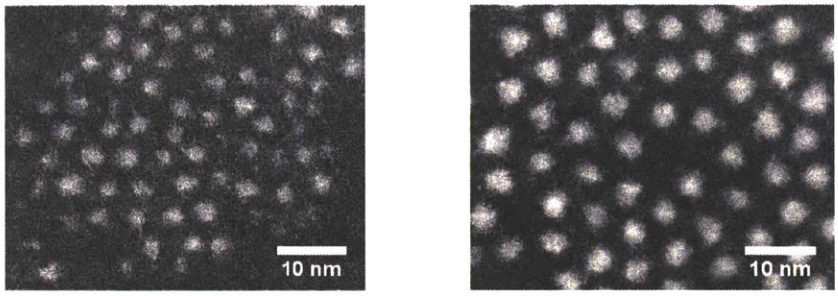

Figure 5-6: Comparison of MALDI mass with STEM imaging

We also tested the sensitivity of MALDI characterization at low mass using two growth mixtures with UV absorption features (Figure 5-7). The growth mixtures labeled as "Cluster 1" are also the most reported InP clusters in the literature. Although only one first absorption peak for this sample is observed located at around 380 nm, its mass characterization shows that the growth mixtures actually contain two major groups of clusters. Apparently, the absorption feature of the larger clusters has covered that of the smaller ones. For the growth mixtures labeled as "Cluster 2", despite the absorption peak located at around 360 nm, they also have broad absorption features at around 380 nm. Interestingly, both clusters from "Cluster 1" also exist in the growth mixtures labeled as "Cluster 2", according to the mass spectra. Despite that we observed fragmented peaks in the mass characterization of clusters, "Cluster 2" has smaller masses as compared to "Cluster 1", consistent with their corresponding absorbance measurements.

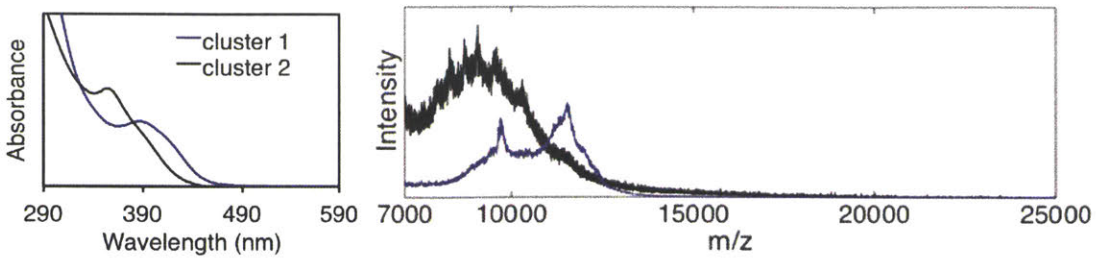

Figure 5-7: UV-Vis absorbance measurement (left) and MALDI low mass characterization (right) of two InP clusters.

5.4 Role of Clusters During Late-Stage InP QD Growth

InP QDs have been synthesized in both one-step and two-step manners in batch syntheses. In a one-step procedure, one precursor is injected into the other at temperatures around 270 – 300 °C and then the growth continues. In a two-step process, the precursors are mixed at medium temperatures around 100 – 130 °C and then the resulting mixtures are brought up to elevated growth temperatures. InP clusters synthesized at medium temperatures have been characterized using absorbance measurement. However, when they are heated at high temperatures, it is not clear whether they still exist, since the formation of QDs can cover the absorbance signal of these clusters. It also remains a question whether these clusters form at all when the precursors are mixed at high temperatures. To answer the above questions, we first performed one-step syntheses and then tracked the growth of InP QDs after mixing precursors at high temperatures. Then we performed syntheses in a two-step manner where after the formation of clusters at medium temperatures, we tracked the transformation of these clusters at high temperatures.

InP growth intermediates were first synthesized at different growth times and temperatures in a one-stage tube reactor system (Figure 5-8). The absorbance measurement shows the occurrence of clusters at early growth times, with these clusters later transforming into larger

nanocrystals. It should be mentioned that the absorption features of these clusters are visible in the absorbance spectra until 2.2 min of reaction (growth time calculation from flow rates available at Table C 1). Compared to the absorbance measurement, MALDI MS spectra of the same InP growth mixtures not only provide information on the mass evolution of the larger particles, but also reveal the existence of the clusters with masses around 10k Da during the growth process. For the QD growth at 240 °C, similar clusters remain in the growth solution while the QD mass increases from 60 kDa close to 90 kDa. Surprisingly, clusters still exist even after 13 min of reaction time at 240 °C (Figure 5-9). Complete consumption of the clusters is only achieved for growth times longer than 8 min at 270 °C (Figure 5-8 top black curves and Figure 5-9).

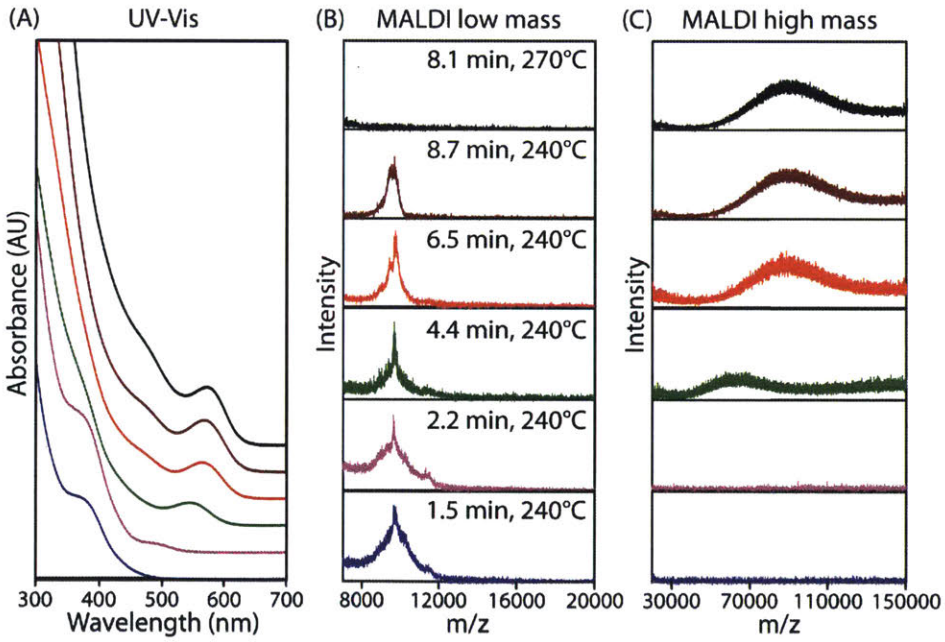

Figure 5-8: (A) UV-Vis absorbance spectra and their corresponding (B) low mass and (C) high mass MALDI spectra of GPC-purified InP growth mixtures synthesized in a tube reactor. The growth time and temperature are provided in the middle figure for each condition.

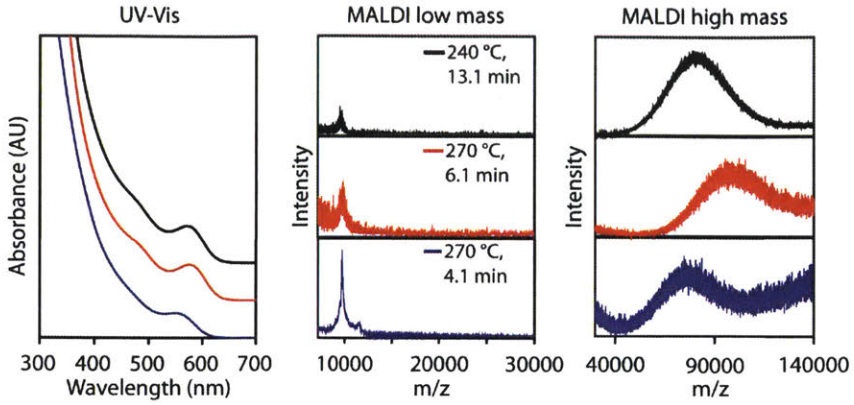

Figure 5-9: Additional MALDI low and high mass spectra of InP growth intermediates synthesized at 240 and 270 °C in the tube reactor.

These small cluster mixtures are also observed in two-step syntheses, where clusters are first formed at low temperatures and then used as precursors to form QDs at high temperatures. In a two-stage chip reactor system,[133] these similar clusters show up after the precursor reaction in the first reactor at 130 °C (Figure 5-7 black curve), and then grow in a second reactor at temperatures between 180 and 300 °C (Figure 5-10). Although the absorption features of these clusters are not visible at growth temperatures higher than 180 °C, mass characterization shows their existence even at 300 °C. As higher temperature results in the formation of larger nanocrystals, these clusters are not yet fully consumed. Two-step batch syntheses also confirm the existence of the cluster mixtures with masses around 10 kDa, where a different solvent (1-ODE) is used. At low temperature (150°C) and short growth time (1 min), these clusters form at the beginning of the reaction and remain present throughout the growth at 230°C for 14 min (Figure 5-11).

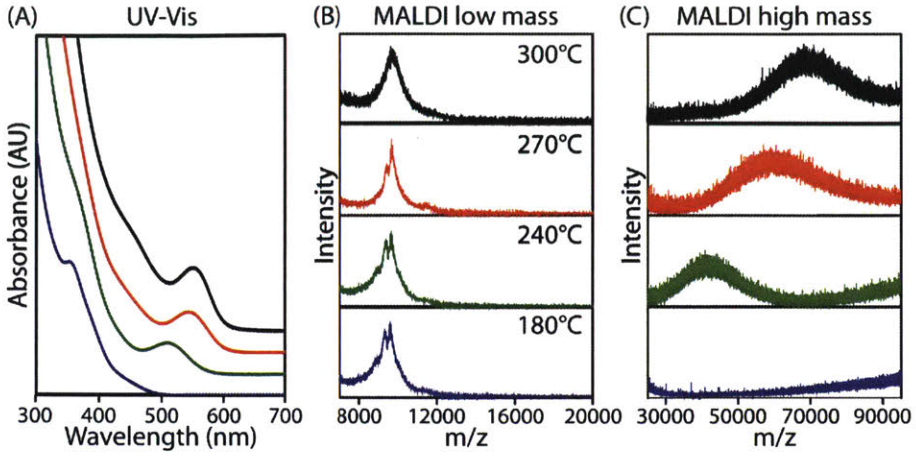

Figure 5-10: (A) UV-Vis absorbance spectra and their corresponding (B) low mass and (C) high mass MALDI spectra of GPC-purified InP growth mixtures synthesized in a two-stage chip reactor system. The temperature of the first stage is 130 °C and that of the second stage is shown in the middle figure for each condition.

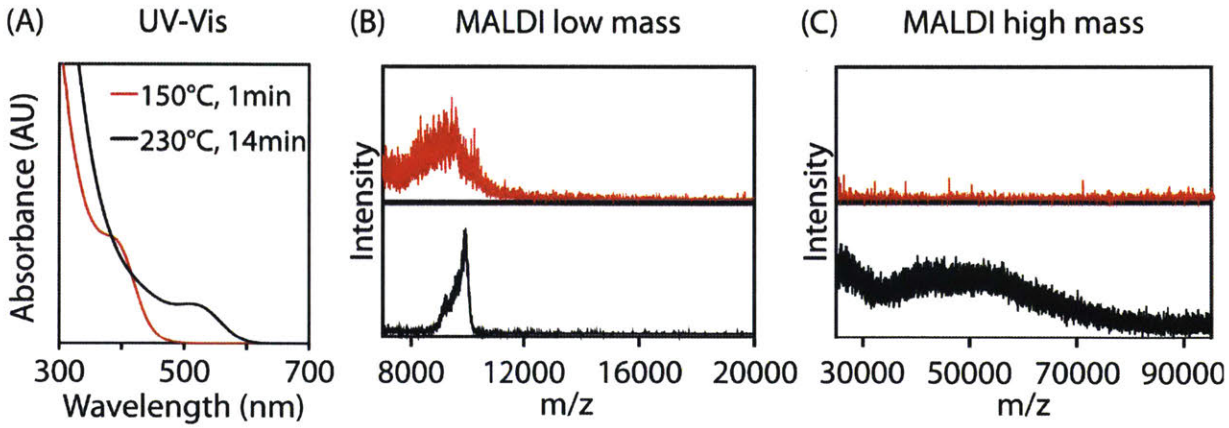

Figure 5-11: UV-Vis and MALDI characterization of InP growth intermediates prepared in batch synthesis.

Sub-nm InP clusters with an absorbance peak below 400 nm have been previously identified as important growth intermediates during the formation of InP QDs.[47, 88] However, the UV absorption features of large nanocrystals in late-stage growth can overshadow that of the clusters and thus hide their presence. With MALDI MS, the clusters can be differentiated in the growth

mixtures. Our observation of similar clusters in MALDI MS under different synthetic methods confirms their presence and stability during the growth of InP QDs. Moreover, the strong dependence of QD formation on the clusters' existence suggests their role as a continuous supply for the growth of larger InP nanocrystals.

5.5 Limitation in MALDI Characterization

While MALDI MS has been used to uncover the existence of clusters during the late-stage QD formation, we have encountered several challenges in revealing the mass signal of QDs during the initial transformation of clusters. For example, as Figure 5-12 shows, although the formation of QDs is clearly visible in the absorbance spectra, we can only capture the existence of clusters in the growth mixture (the high mass characterization also shows no QD signal). There are several explanations for this discrepancy. First, during the initial transformation of clusters, the overall QD concentration is much lower than that of clusters and the size distribution of QDs is also very broad. As a result, for QDs with specific masses, their concentration can be very low. As the spectrometer is more sensitive in low-mass characterization, indicating that clusters are easier to be desorbed and ionized as compared to QDs (Figure C 10), the QD mass signal may be buried in the noise. Second, it is also observed that clusters tend to form crystals more easily than QDs during the sample preparation process. Due to the different crystallization speeds between QDs and clusters, QDs are likely to be wrapped inside of the cluster crystals. As the MALDI laser desorbs samples from the crystal surface, the QDs may not be detected due to this sample inhomogeneity. In summary, MALDI is only a qualitative characterization method and the numerical intensity obtained from the mass spectra should not be linked directly to the particle concentrations.

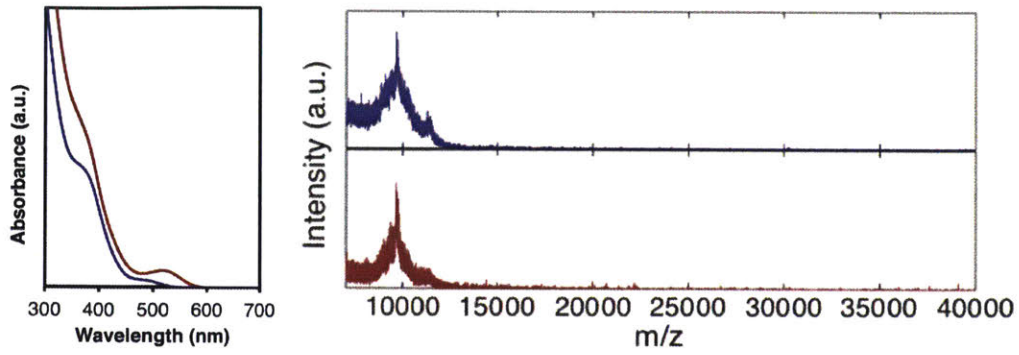

Figure 5-12: Comparison between absorbance (left) and MALDI (right) measurement during the initial transformation of clusters to form QDs.

5.6 Conclusion

In this chapter, we have used various experimental techniques to probe the formation of clusters and their roles in the late-stage growth of InP QDs. According to the absorbance measurement, the formation of clusters is observed at the early-stage growth in an indium-rich environment, consistent with our *ab initio* observations in Chapter 3. We have also developed a one-solvent air-free protocol involving HT and HP flow syntheses, GPC purification, and MALDI mass characterization to track the existence of clusters along with the QD formation. Careful validation has been performed to ensure the applicability, accuracy, and resolution of MALDI MS in characterizing InP growth mixtures.

The use of MALDI MS allows for differentiating the signals of clusters and QDs, yielding important insights into InP QD growth. Interestingly, similar clusters are persistent during the formation of QDs regardless of the different synthetic approaches and solvents in use, suggesting their role as a supply for the formation of larger InP nanocrystals. The protocol of using MALDI MS thus provides new opportunities in characterization and understanding of the growth mechanism underlying small-sized air-sensitive clusters or QDs.

Chapter 6

Effect of Impurities, Ligands and Solvents

6.1 Introduction

In the literature, effects of synthetic parameters other than precursor reactivity have also been explored as alternative strategies to tune the growth of InP QDs. For example, acids and amines are found to significantly impact the size tunability and size distribution of InP QDs. Acids have been used as one of the major methods to obtain large QDs with first absorption peaks redder than 600 nm. By combining amines and acids during the synthesis, InP based QDs can be grown with first absorption peaks ranging from 400 nm to 700 nm.[5] However, the synthesis with these ligands presents a dilemma. For *acids*, they are found to cause side reactions that interfere with the QD growth. They can react with $P(TMSi)_3$ as a proton source to generate $PH_x(TMSi)_{3-x}$ species, which are thought to compete with $P(TMSi)_3$ for indium monomers during the nanoparticle growth and thereby to contribute to the broadening of the size distribution.[49] *In situ* water generation is also observed in the presence of excess acids through their ketonization reactions, and water is proposed to cause the hydroxide/oxide formation on the nanoparticle surfaces under growth conditions.[50] This hydroxide/oxide layer is speculated to be one of the reasons for the inhibited growth of InP QDs. For *amines*, oxide formation on QD surfaces is also

observed in their presence.[51] Amines can also disrupt the InP cluster formation processes and result in QDs with broad size distribution.[47]

The high sensitivity of InP growth towards acids and amines motivates us to perform studies on the effect of common synthetic parameters, including impurities, ligands, and solvents. In this chapter, I will first discuss the effect of trace water in limiting the growth of InP QDs. Although the syntheses of indium precursors are believed to be "water-free", we observed that the commonly used indium precursors derived from anhydrous $In(Ac)_3$ actually contain a detectable amount of water. Water, as previously discussed, can serve as a proton source or a hydroxylation factor to affect the QD formation processes. I will then present a strategy to tune the growth of InP QDs through the use of ligands such as TOP and TOPO. These ligands can be removed from the QD surfaces after purification, suggesting that they are weakly coordinating ligands. Finally, I will discuss the use of different low-boiling-point solvents in synthesizing InP QDs. The use of an HT and HP microfluidic platform enables us to explore this parameter space, which is not accessible in conventional batch syntheses.

6.2 Effect of Trace Water

One of the most common methods for the *in situ* generation of indium precursors, utilized here, uses anhydrous $In(Ac)_3$ and long chain carboxylate acids. Although water is not a byproduct of this reaction, we observed that the synthesized $In(My)_3$ precursors actually contain a detectable amount of water due to the water contamination in the $In(Ac)_3$. This phenomenon has been discussed previously.[135, 162] In this part, we provide direct evidence showing how the growth of InP QDs is affected by the water contamination in the $In(My)_3$ precursors. Unlike traditional batch syntheses of InP QDs where $In(My)_3$ is generated *in situ* and then mixed with $P(TMSi)_3$ at elevated temperatures, our synthetic procedure involves two steps: first, the as-

synthesized indium precursors are purified and vacuum-dried and then stored in a glove box; second, the indium precursors are dissolved to react with phosphorus precursors in a microfluidic reactor system in an inert atmosphere. The approach of isolating and purifying the indium precursors eliminates the effect of excess acids on the precursor chemistry and the surface chemistry during the nanoparticle growth.

At low water content, InP growth is largely dependent on the temperature and time with the first absorption peak reaching 620 nm (Figure 6-1 a). The growth becomes inhibited as the water content increases and the first absorption peaks is pinned around 550 nm (Figure 6-1 b). Although the nanoparticle size is larger at lower water content, the particle shape is irregular. The absolute absorbance below 400 nm (i.e., 310 nm) provides a qualitative measurement of the QD reaction yield by assuming that the extinction coefficient of InP QDs in the UV region scales with particle volume.[41,49] The reaction yields are similar for both low and high water content, while the particle concentrations are estimated to increase with increasing water content (Table D 1). In our experiments, the water content was varied by directly adding water to the relatively dry $In(My)_3$ (water/$In(My)_3$ (mol/mol) = 0.015), which was synthesized using $In(CH_3)_3$ and dried MA (water/MA ~ 0.002) (water contents of the relevant precursors and solvents are summarized in Table D 2 and Table D 3). Differences in the QD growth behavior can be attributed directly to water due to the precise control of growth time and temperature that is offered by the microfluidic set-up.

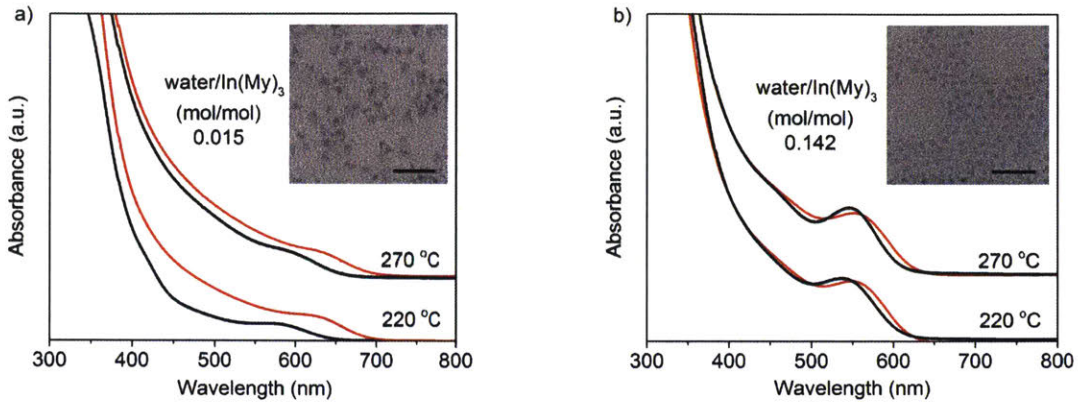

Figure 6-1: Absorption spectra and TEM images of InP QDs with different water contents in the $In(My)_3$ solutions in a 2-stage (black line) and 3-stage (red line) reactor. In a), water/$In(My)_3$ (mol/mol) is 0.015, equivalent to 15 ppm water in the 40 mM $In(My)_3$ precursor solution. In b), water/$In(My)_3$ (mol/mol) is 0.142, equivalent to 144 ppm water in the 40 mM $In(My)_3$ precursor solution. For a 2-stage reactor, the temperature of the first stage is 130 °C while the temperature of the second stage is shown in the figure; for a 3-stage reactor, the temperature of the first and second stage is 130 °C and 220 °C while the temperature of the third stage is shown in the figure. The chip reactor system was used for the experiments. The bar length in the TEM images is 20 nm. Spectra are off-set for clarity.

When water/$In(My)_3$ (mol/mol) is below 0.05, the wavelength of the first absorption peak decreases with increasing water content (Figure 6-2). When water/$In(My)_3$ (mol/mol) is higher than 0.05, the first absorption peak appears pinned at ~540 nm, indicating that the effect of water on size tunability becomes saturated. In our experiments, the water content measured from different batches of $In(Ac)_3$-derived $In(My)_3$ ranges from 0.065 ~ 0.182 (Table D 2 and Table D 3) and the corresponding first absorption peaks stay around 540 nm. It is known that without a large excess of acids or multiple injections of precursors, the use of $In(Ac)_3$-derived $In(My)_3$ and

$P(TMSi)_3$ fails to produce nanoparticles with an absorbance peak as red as 600 nm.[5, 24, 55] Our results suggest that the water contamination in the $In(Ac)_3$-derived $In(My)_3$ precursors may be one of the reasons for the previously observed limited size tunability of InP QDs. Besides the water contamination in the indium precursors, previous work has also shown that water can be generated *in situ* by the ketonization reaction of excess acids under growth conditions[50]. While excess acids could help produce large InP QDs, their water-generating side reactions could have the opposite effect on the growth.[49]

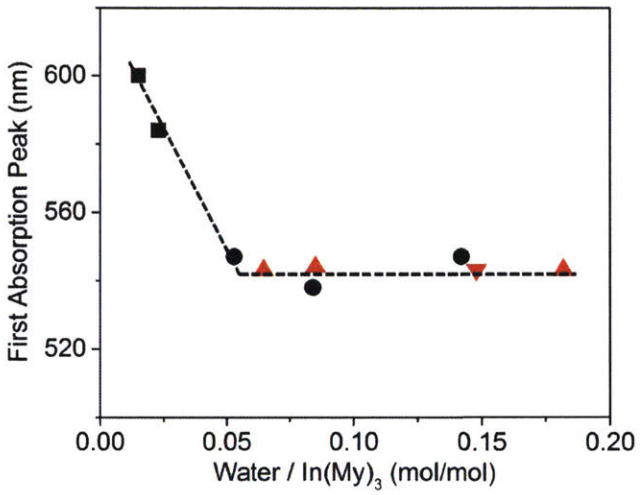

Figure 6-2: Position of the first absorption peak of InP QDs changing with water content. (black square) indicates $In(My)_3$ synthesized from $In(CH_3)_3$, (black dot) indicates water doped $In(My)_3$ synthesized from $In(CH_3)_3$, (red up triangle) indicates $In(My)_3$ synthesized from $In(Ac)_3$, (red down triangle) indicates water doped $In(My)_3$ synthesized from $In(Ac)_3$. The dashed line is for visualization. The 2-stage chip reactor system was used for the experiments. The temperature of the first and second stage was 130 °C and 270 °C, respectively.

At low temperatures (≤130 °C), the formation of small clusters with the first absorption peak around 385 nm is observed at both low and high water contents under similar conditions (Figure 6-3 a), indicating that the size tunability is not affected. When the temperature is increased (≥220 °C) the absorption spectra under conditions of increased water content are blue shifted ~30 nm (Figure 6-3 b). It has been suggested that the formation of InP QDs consists of two major steps: precursors deplete at the early stage of growth to form small clusters, and these clusters interact with each other through inter-particle processes such as ripening, coalescence or second nucleation. These clusters are believed to react further to form InP QDs via inter-particle processes that occur at elevated temperatures. Spectral differences between wet and dry syntheses appear only at the elevated temperatures where interparticle growth dominates. Therefore, it is likely that the presence of water inhibits this inter-particle growth.

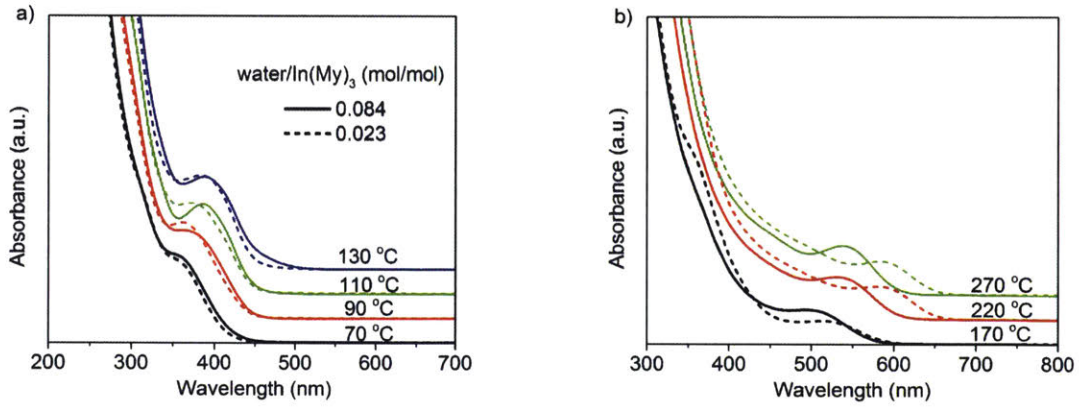

Figure 6-3: Absorption spectra of InP QDs at low and high temperature range. In a), the temperatures of the first and second stage are the same as shown in the figure. In b), the temperature of the first and second stage is 130 °C while the temperature of the second stage is shown in the figure. The water content was varied by adding water to $In(My)_3$ (water/$In(My)_3$

(mol/mol) = 0.023). The chip reactor system was used for the experiments. Spectra are off-set for clarity.

The mechanism for how water may affect the tunability of InP QD growth has been noted in literature. Cros-Gagneux et al.[50] hypothesized that water could provide an oxidizing environment to form oxides/hydroxides on the InP nanoparticle surface under growth conditions, which could inhibit nanoparticle growth. Consistent with their hypothesis, we show that at low water content, the growth can be effectively tuned by growth temperature and time, while at high water content, the growth becomes inhibited. Other studies also reveal the role of water as a hydroxyl source to cause the formation of oxides/hydroxides on nanoparticle surfaces. Reiss et al.[51] synthesized InP/In_2O_3 core-shell nanoparticles, and attributed the oxide shell formation to the hydroxylation of water on the nanoparticle surface. In their study, water was generated by the side reaction between amine and anhydride. Recently, Zherebetskyy et al.[137] also discussed the role of water impurities in lead precursors in generating hydroxyl groups on PbS nanoparticle surface to affect nanoparticle size and size tunability. Based on previous work, we attribute the inhibited growth of InP QDs to the hydroxylation effect of water. As observed for the hydrolysis reaction between water and indium carboxylates, it is likely that the increased temperature facilitates the hydrolysis rate of water towards the InP cluster surface, which leads to the formation of hydroxide/oxide layers on the surface and therefore inhibits nanoparticle growth.

To further test the hydroxylation effect, we intentionally added base to the $In(My)_3$ solution. The purpose of adding base was to increase the hydroxyl concentration in the indium solutions. The growth of InP QDs with base addition was conducted in the tube reactor system to eliminate any possible interaction between the strong base (KO^tBu, pKa of its conjugate acid is 17) and the SiO_2 surface of the chip reactors. We note that the KO^tBu remains as a solid in the precursor

solution, and is filtered out prior to nanoparticle growth. Figure 6-4 shows a comparison of the spectra with and without addition of base to the nearly dry and wet indium precursors. We hypothesize that the addition of KO^{t}Bu transforms all the water impurities in the indium precursors to free hydroxides. The blue shift of the spectrum (black curve) due to the addition of base to the nearly dry $In(My)_3$ precursor (green curve) is more pronounced than when a similar amount of water is added to the $In(My)_3$ precursor solution (red curve), indicating the strong effect of free hydroxides in inhibiting the growth of InP QDs. A further blue shift was observed when base was added to the wet $In(My)_3$ (blue curve), confirming the effect of increasing hydroxide content in inhibiting the nanoparticle growth.

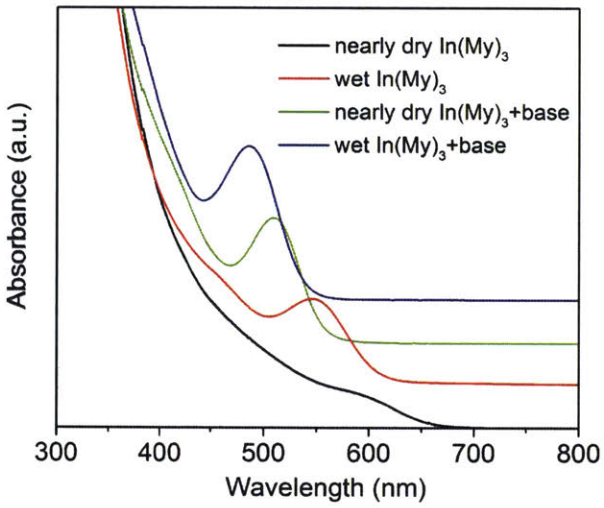

Figure 6-4: Absorption spectra of InP QDs with base addition. Water content in "nearly dry $In(My)_3$" and "wet $In(My)_3$": water/$In(My)_3$ (mol/mol) = 0.015 and 0.142, respectively. Base content: KO^{t}Bu/$In(My)_3$ (mol/mol) = 0.134.The growth temperature of the first and second stage was 130°C and 270°C respectively. Spectra are off-set for clarity.

Therefore, our results regarding the effect of hydroxyl impurities provide direct evidence for the hypothesis suggested in previous work that water limits the growth of InP QDs. They also

highlight concerns about the impurities that are introduced or generated *in situ* during the QD growth. While our work mainly focuses on showing the hydroxylation effect of water on nanoparticle growth, the interaction between water and phosphorus precursors at the early stage of growth is also possible. The product from this reaction, $SiMe_3OH$, could also serve as another hydroxyl source interfering with QD growth. Taken together, these considerations indicate the complex role of water in affecting precursor reactions and QD formation, and heighten concerns about water contamination in indium precursors.

6.2.1 Water Effect on InAs QDs

While water is found to drastically impact the growth of InP QDs, no obvious effect is observed during the syntheses of InAs QDs (Figure 6-5). This phenomenon is similar to that observed for acids, which are found to help produce larger InP QDs but not to influence the growth of InAs QDs. These observations underlie the differences between InP and InAs, and raise cautions in directly extrapolating the mechanisms observed for InP QDs to that of InAs.

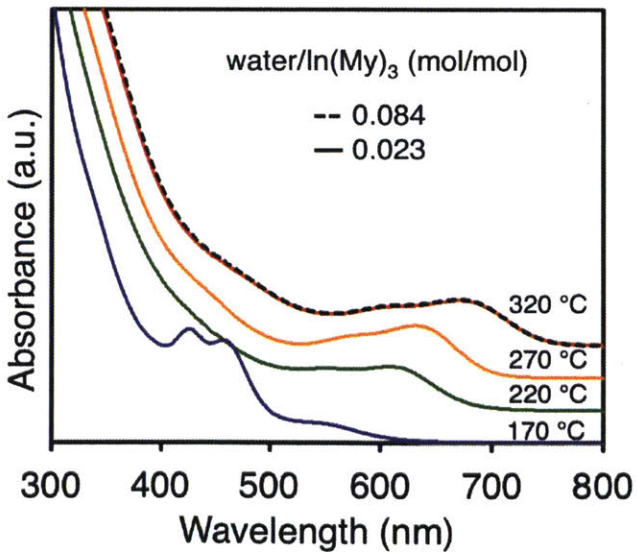

Figure 6-5: The growth of InAs QDs with or without water addition into the $In(CH_3)_3$-derived $In(My)_3$ precursor. A two-stage chip reactor is used and the temperature of the first stage is set as

130 °C with the temperature of the second stage shown in the figure. $As(TMSi)_3$ is used as the arsenic precursor and its concentration is set as 20 mM in octane. The indium concentration is set as 60 mM. The flow rates of both precursors are set as 30 μL/min.

6.3 Effect of Ligands

Although the addition of trace amounts of hydroxyl impurities such as bases drastically changes the InP QD growth, they are not favorable ligands to tune the nanocrystal sizes as the hydroxyl groups can permanently poison the nanoparticle surfaces. However, the study suggests that it is possible to adjust the growth of InP QDs by controlling the coordinating strength of ligands towards indium. As changing precursor reactivity fails to improve the size tunability and size distribution of InP QDs, this phenomenon inspires us to explore the ability of ligands with different coordinating strengths to tune the QD growth. In particular, we aim to develop a strategy to synthesize cluster-free QDs with varying sizes, as the presence of clusters not only reduces the overall reaction yield of InP QDs, but also affects the results of their optical studies. As will be seen in this part, we have applied different surfactants to prepare InP QDs with different sizes. Regardless of the different ligands combination, they are directly added to the $In(My)_3$ precursor solutions and the syntheses are performed at high growth temperatures (270 °C) and with long reaction times (above 8 min). These ligands also help dissolve the indium precursors in the solvent to allow for the flow operations.

TOP and TOPO are the main ligands that have been investigated. Both ligands can help dissolve the indium precursors in solvents such as toluene or octane. Increasing both ligand concentrations helps reduce the final QD sizes. Syntheses utilizing TOPO generate smaller QDs than TOP, indicating a stronger coordinating effect. The same phenomena are observed regardless of the solvents in use (Figure D 5). By tuning the concentration of TOPO and TOP,

QD samples with first absorption peaks ranging from 520 to 580 nm are synthesized in toluene with $In(My)_3$ prepared from fresh $In(Ac)_3$ (Figure 6-6). In general, high growth temperatures and long growth times are necessary in order to obtain cluster-free QDs (detailed growth conditions available in Appendix C and D). As further increasing TOPO amounts fails to reduce the QD sizes (Figure D 6), smaller QDs are obtained by adding trace amounts of bases into the indium precursor solutions (a sample spectrum with first absorption peak at 509 nm is shown in Figure 6-6). MALDI MS of these solutions at low mass shows no detectable clusters, while high mass characterization maps out QD masses ranging from 40 to 99 kDa. By increasing the base amount, QD samples with the first absorption peak as small as 475 nm can be obtained. However, the resulting QDs have dual peaks in their mass spectrum and the cluster signal is still visible (Figure D 7). Small amounts of amines can also be used to reduce the size of QDs with their first absorption peaks as small as 470 nm. However, multiple peaks are observed in the mass spectrum, including those of clusters in the low mass range (Figure D 8). Among the above four surfactants, TOP and TOPO can be fully removed after GPC purification, while small amounts of amines and hydroxyl groups remain bonded to the nanoparticle surfaces, as shown by the NMR characterization (Figure D 9 and Figure D 10).

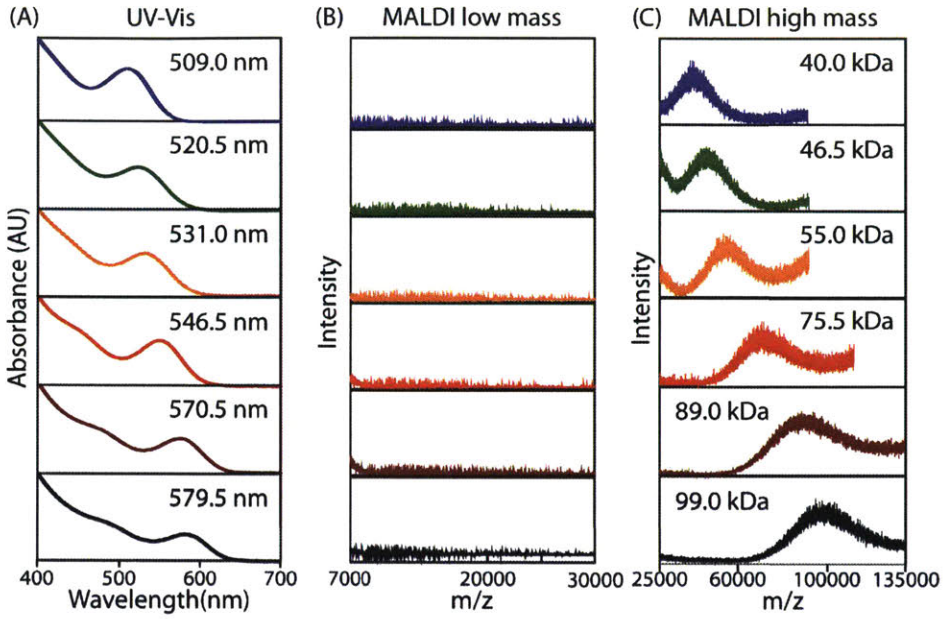

Figure 6-6: A) UV-Vis absorbance, (B) low mass and (C) high mass MALDI MS spectra of GPC purified cluster-free InP QDs synthesized in a tube reactor in toluene at 270 °C.

The synthesis of cluster-free InP QD samples allows us to extract size-dependent absorption calibration curves and molar extinction coefficients of QDs, which are essential for studies concerning nanocrystal sizes and concentrations.[142-144] With MALDI MS, the extinction coefficient of a QD sample can be quantified by measuring its absorption and then determining its concentration by dividing the QD dry mass by the MALDI particle mass (Table 6-1). Unlike the traditional method of quantifying extinction coefficients based on TEM, here no assumption regarding the particle shape or density is made. Nevertheless, with the estimated inorganic core mass, the size of the particles can be estimated by assuming a certain shape, and a sizing curve can be constructed. Furthermore, for clusters free QDs synthesized from TOP and TOPO, as myristate is the only organic ligand on the QD surface, which is the only proton source on the nanoparticle, the mass information combined with proton quantification through NMR can provide the number of ligands and InP units per particle (Table 6-1). It should be noted that,

regarding the sample with the first extinction peak at 509 nm, hydroxides are also bonded to the nanocrystal surface due to the introduction of bases. As it is difficult to fully differentiate the signal of hydrogen in hydroxides from the other hydrocarbons in the NMR spectra, we did not evaluate the number of InP units for this sample.

As previous studies have indicated, the extinction coefficient of QDs scales linearly with their effective nanoparticle volume,[41] and hence with the number of molecule units per particle. With the extinction coefficients and the number of InP units, this scaling factor, namely, the extinction coefficient per InP unit, can be calculated for QDs with different sizes. This scaling factor is found to be around 5100 $M^{-1}cm^{-1}$ for InP QDs evaluated in our work (Table 6-1 and Figure D 9), which agrees well with previous literature on InP QDs with similar sizes[23] (Figure D 10). The estimated absorption cross section of QDs at 310 nm also agree well with that of bulk materials (Table D 5). We have also evaluated the extinction coefficients at 350 nm to compare with available literature results, and observed good agreement for InP QDs with similar sizes[23] (Figure S13).

Table 6-1: Cluster-free QDs with their first absorption peaks, their estimated number of ligands and InP units, and their extinction coefficients per particle (ε) and per InP unit (ε') at 310 nm.

First Abs. peak (nm)	# of ligands	# of InP units	ε ($M^{-1}cm^{-1}$)	ε' ($M^{-1}cm^{-1}$)
520.5	111	117	6.0×10^5	5.1×10^3
531.0	130	141	7.1×10^5	5.0×10^3
546.5	157	198	10.2×10^5	5.2×10^3
570.5	185	274	14.3×10^5	5.2×10^3
579.5	201	313	16.1×10^5	5.1×10^3

It should be mentioned that the strategy of using ligands such as TOPO and TOP to tune QD sizes also provides opportunities for the synthesis of high-quality InP-based core-shell structures. Unlike ligands such as amines and acids that can cause side reactions to interfere with the InP growth, both TOP and TOPO are weakly coordinating ligands and can be removed from the QD solution after purification. As a result, their impact towards the shell synthesis can be eliminated. In addition, with the known extinction coefficients, better control of the shell growth can be achieved as the QD concentration can be calculated and the concentration of shell precursors can be rationally designed.

6.4 Effect of Solvents

One advantage of operating under HT and HP conditions is the ability to choose from a wide range of solvents with low boiling points. Analogous to 1-ODE, a commonly used batch solvent, short-chain alkanes have been used for the synthesis of II-VI and III-V QDs. It is found that alkane solvents with lower viscosity such as hexane or octane produce CdSe QDs with smaller sizes and narrower size distributions.[85] The results are explained by the improved mixing performance with lower viscosity, which results in the formation of more nuclei and thus smaller final particle sizes. Thus far, no other low-boiling-point solvents besides octane have been used to grow III-V QDs. However, for the MALDI mass characterization, we have used toluene instead of octane for the syntheses to meet the one-solvent requirement for GPC purification and matrix preparation. As toluene has different physical properties than octane, such as viscosity and polarity, we are interested in whether the change of solvent can result in a change of QD growth behaviors. Therefore, in this part, we have compared the syntheses with different low-boiling-point solvents. We have focused on solvents containing only C and H atoms as other atoms such as O or N may coordinate on the indium to interfere with the QD growth.

Octane and toluene are the two major solvents used for the syntheses. Growth with toluene shows a greater dependence on the batch-to-batch variations in indium precursors than octane. For example, for $In(My)_3$ synthesized from aged and fresh $In(Ac)_3$, the indium precursor solutions in octane produce InP samples with similar first absorption peaks around 570 nm, while a difference of 40 nm in the first absorption peaks is observed when toluene is used (Figure 6-7). It is observed that when dissolving $In(My)_3$ in TOP-solvent mixtures, trace amounts of white solids (~mg) remain in the octane but the toluene solution is clearer. This phenomenon is more obvious for $In(My)_3$ synthesized from aged $In(Ac)_3$. We have attributed the white solids to the hydroxide/oxide-containing indium species. The existence of hydroxide/oxide contamination is supported by the ESI mass characterization of the $In(My)_3$ precursors (Table 6-2, Figure D 11, Figure D 12 and Figure D 13). We hypothesize that these indium species are more soluble in polar solvents such as toluene. As our previous study shows, hydroxylation of the indium precursors could cause a drastic blue shift of the first absorption peak. The aged $In(Ac)_3$ contains more hydroxides/oxides, which are later transferred to the $In(My)_3$ precursors. Therefore, with aged $In(Ac)_3$, syntheses using toluene produce much smaller QDs than those from fresh $In(Ac)_3$. Meanwhile, due to the low solubility of the hydroxide/oxide-containing indium species in octane, the growth is insensitive to the freshness of the indium source.

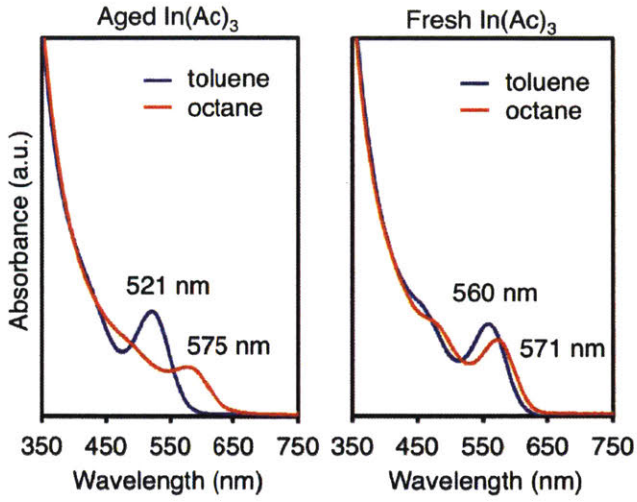

Figure 6-7: Growth comparison with toluene and octane using $In(My)_3$ synthesized from aged and fresh $In(Ac)_3$. 4 vol% TOP is added to the indium precursor to improve their solubility. A one-stage tube reactor with a 355 μL volume is used for the synthesis at 270 °C and the flow rates of indium and phosphorus precursors are set as 15 μL/min.

With $In(My)_3$ derived from fresh $In(Ac)_3$ as the precursor, we investigated the role of solvent viscosity in affecting the growth (Figure 6-8). O-xylene is used to compare with toluene and heptane is used to compare with octane (Table D 4). These solvents are all dried with molecular sieves and their measured water contents are below 10 ppm. In all the conditions, heptane and octane behave similarly although the operating temperature (270 °C) and pressure (900 psi) is already in the supercritical regime of heptane. At a short growth time (i.e., flow rate 60 μL/min), the growth is identical between toluene and o-xylene. With longer growth times, the more viscous o-xylene produces QDs with slightly larger sizes but broader size distributions, indicating a stronger ripening process due to the poorer mixing performance of the solvent as compared to toluene. Nevertheless, these solvents can be used for the synthesis of InP QDs with high quality.

Table 6-2: Representative m/z peaks from ESI mass spectrometry for the characterization of $In(My)_3$ precursors dissolved with TOPO in CH_2Cl_2 with 30 vol% ethanol.

Composition	m/z* (experimental)	m/z* (theoretical)	Proposed molecular constituents	Absolute relative error (ppm)
$[C_{100}H_{207}InP_3O_7]^+$	1729.4101	1729.4125	$[In(My)_2(TOPO)_3]^+$	1
$[C_{128}H_{262}In_2P_3O_{12}]^+$	2315.7432	2315.7213	$[In_2(My)_4OH(TOPO)_3]^+$	9
$[C_{156}H_{315}In_3P_3O_{16}]^+$	2884.0135	2884.0198	$[In_3(My)_6O(TOPO)_3]^+$	2
$[C_{56}H_{108}InO_8]^-$	1023.6873	1023.7095	$[In(My)_4]^-$	22

* The m/z peak used here corresponds to the highest intensity peak among the isotope

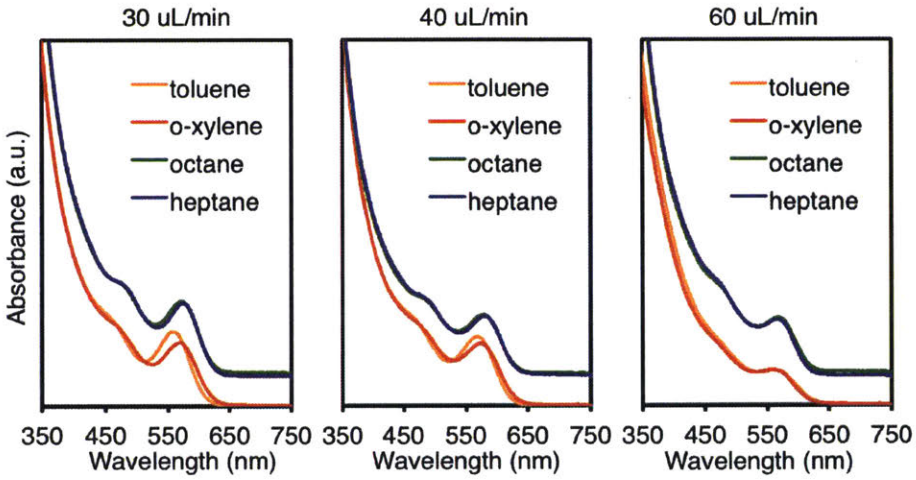

Figure 6-8: Growth comparison with different solvents with 4 vol% TOP added to the indium precursor to improve their solubility. A one-stage tube reactor with a 355 μL volume is used for the synthesis at 270 °C. The total flow rates are indicated in the figure.

6.5 Conclusion

In this chapter, we have investigated how impurities, ligands, and solvents impact the growth of InP QDs. Water impurities in indium precursors are found to limit the QD growth, likely through its hydroxylation effect towards indium. Different ligands can also interact with

indium with different coordinating strengths, resulting in QDs with different sizes. The freshness of indium sources may also cause different levels of hydroxide/oxide contamination in the syntheses, causing batch-to-batch variations. Clearly, the effects of these synthetic parameters are all related to the indium precursors. However, although significant efforts have been devoted to finding alternative phosphorus precursors in the literature, indium precursors have not attracted equal attention. The quality control of indium precursors and the design of novel indium-precursor-ligand combinations are to be better understood to further improve the size tunability and size distribution of InP QDs.

Chapter 7

Summary and Outlook

7.1 Summary

InP QDs stand out as the most promising candidate to replace the currently commercialized cadmium-containing materials for optoelectronic applications. To produce high-quality InP QDs, significant efforts have been devoted to their synthetic development and growth mechanism studies. The most common recipe to synthesize InP QDs utilizes indium carboxylates and $P(TMSi)_3$ as precursors. Before this thesis work, most of the mechanism studies regarding III-V InP QD growth focused on precursor conversion events, where the fast reactivity of group V precursors is hypothesized to cause the broad size distribution and limited size tunability of QDs. However, common experimental methods such as absorbance measurement, TEM imaging, and NMR spectroscopy have limited capability to identify the difficult-to-isolate early-stage intermediates or track the intermediate species during the formation of InP QDs. In spite of the many first-principles calculations to study II-VI QDs, no theoretical work has been performed previously to facilitate our mechanistic understanding of the growth of InP QDs. Therefore, in this thesis, both experimental and theoretical approaches have been used to study the growth mechanisms of III-V QDs, in particular InP, from precursor conversion to final nanocrystal formation. The overall contributions of this thesis to the QD community are summarized below:

First, we have developed novel theoretical and experimental methodologies to study the growth of InP QDs: (1) The high-temperature *ab initio* molecular dynamics sampling approach enables us to discover the indium-rich cluster formed at the early-stage growth and identify the mechanism pathways for the formation of In-P bonds. This *ab initio* discovery tool is well suited to study the early-stage QD reaction mechanisms involving short-lived and reactive intermediates. (2) The air-free and one-solvent protocol involving MALDI MS allows us to characterize the late-stage intermediates during the growth of InP QDs. The MALDI experiments revealed the role of clusters as a continuous supply for the formation of large nanocrystals, which would have been difficult via other spectroscopic methods. Our protocol provides new opportunities for characterization and understanding of the growth mechanism underlying small-sized air-sensitive clusters or QDs.

Second, by combining the results from the theoretical and experimental studies of the precursor conversion mechanisms and the role of clusters, we have constructed a clear picture of the formation process of InP QDs (Figure 7-1): (1) small indium-rich clusters are formed upon the mixing of precursors, possibly through intercomplex or intracomplex pathways; (2) these early-stage small clusters are destabilized by the increase of reaction time or growth temperature, and then are transformed into medium-sized clusters; (3) these medium-sized clusters are relatively stable intermediates, and they are persistent throughout the QD growth, likely serving as a continuous supply for the formation of larger InP QDs; (4) with the full consumption of these stable cluster intermediates, the QD growth is completed.

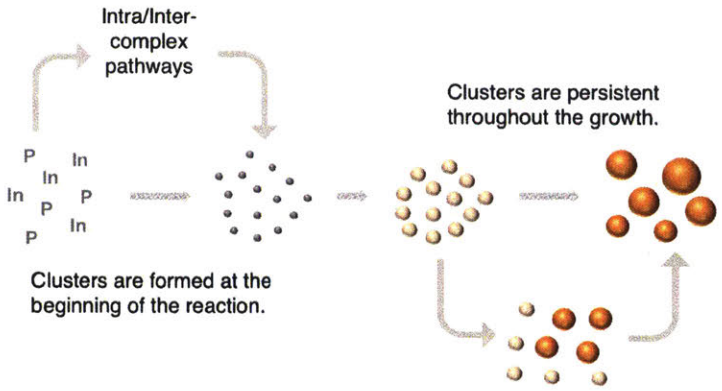

Figure 7-1: Proposed mechanistic picture on the growth of InP QDs.

Third, after investigating the effect of different synthetic parameters, we present strategies to synthesize cluster-free InP QDs with different sizes and narrow size distributions by using weakly associated ligands. These cluster-free QDs allow us to study the QD structure-property relationships. In particular, we apply the mass characterization of these cluster-free QDs to construct a correlation between the first absorption peaks and their extinction coefficients. Accurate molar extinction results are essential in studies concerning nanocrystal size and concentration, and our results are the first demonstration of calculating the extinction coefficient without any assumptions about particle shape and density. In order to improve the size tunability and size distribution of InP QDs, we highlight the importance of the quality control of indium precursors and the novel design of indium-precursor-ligand combinations during the synthesis.

7.2 Outlook

7.2.1 Force field modeling to study the cluster transformation mechanisms

As the role of clusters has been suggested as a continuous supply for the formation of large nanocrystals, the next step is to investigate how the clusters transfer their InP units to QDs at the molecular level. As the atomic sizes of the clusters and QDs already exceed the capability of *ab initio* simulations, reactive force field (ReaxFF) modeling serves as an alternative approach to

obtain this mechanistic understanding. However, there are no available ReaxFF parameter sets for indium.[163] As accurate parameters must be determined for each element or pair of elements, force field parameterizations of indium, indium-oxygen pairs, and indium-phosphorus pairs become necessary. In addition, the parameterized results should be tested with DFT calculations to ensure the accuracy of the ReaxFF potentials.

7.2.2 An integrated core-shell synthesis platform

Ultimately, we would like to synthesize high quality InP-based core-shell structures. As InP QDs are highly sensitive to oxidation, GPC purification in a glove box serves as an ideal solution to purify the QDs and avoid oxidation. A semi-continuous process for the synthesis of InP core-shell QDs is thus proposed which involves the use of HT and HP reactors to synthesize InP cores, followed by the GPC purification to remove excess precursors and ligands. The purified cores are then fed, together with shell precursors, into the HT and HP reactors for the growth of shell structures. To allow for continuous operation, the above syntheses and purification procedures need to be integrated as a full process. The key challenge may be to incorporate multiple GPC columns in parallel to purify the as-synthesized cores in a batch manner, while still maintaining the core and shell syntheses in a continuous manner.

7.2.3 Oxygen-free syntheses of InP QDs

Currently, the synthesis of InP QDs using indium carboxylate chemistry faces two major challenges: quality control and scaling up. Quality-control challenges are due to the synthetic variation and QD oxidation resulting from the hydroxyl/oxide contamination introduced by the indium source and the possible *in situ* reaction of carboxylates during the growth. Scale-up challenges result from the phosphorus precursors being highly pyrophoric. They also produce toxic PH_3 in contact with air. As an alternative approach, indium halides have been proposed to

react with aminophosphine precursors in the presence of amines to produce InP related QDs.[37] As all the reagents used in this protocol are oxygen-free, it eliminates the oxygen contamination problem automatically from the QDs.[38] The phosphorus precursors are also less reactive than the silyl-phosphine analogs and thus more convenient to use. We have demonstrated the flow synthesis of InP QDs using this indium halide approach, but parameter optimization on the core-shell synthesis is still necessary (see Appendix E).

Appendix A

A High Temperature and High Pressure Platform

Experimental Details

Chemicals. Indium acetate (99.99% metals basis) was purchased from Alfa Aesar. Trioctylphoshine (min, 90%) and tris(trimethylsilyl)phosphine (10 wt% in hexane, >98%) were purchased from Strem Chemicals. tris(trimethylsilyl)arsine and other phosphorus or arsenic precursors are synthesized and characterized in Bawendi Lab. Myristic acid (>99%), 1-octadecene (technical grade, 90%), hexane (Laboratory Reagent, ≥95%) and octane (anhydrous, ≥99%) were purchased from Sigma Aldrich. The UV-Vis absorbance measurement of III-V QDs was conducted on an HP 8453 spectrometer.

HT/HP reactors. The system including the two-stage silicon-based chip reactors is similar to that reported previously[53, 55]. Two syringe pumps (Harvard apparatus) were used for solution injections. High-pressure peek tubes and fittings are used to connect reactors and syringes. Other connections, tubes, and devices were made out of type-316 stainless steel, and heating cartridges were made of multipurpose aluminum.

Syntheses of $In(My)_3$. In a Schlenk line, 10 mmol $In(Ac)_3$ (2.93 g) and 30 mmol MA (7.00 g) were mixed in 15 mL 1-octadecene and heated up to 110 °C to form a clear solution under vacuum (< 100 mtorr) for three hours. The reactant solution was maintained under argon and then cooled down to room temperature and white solids precipitated. The solid was washed with

hexane 4 times, vacuum dried overnight and then stored in a N_2-filled glove box. All the glassware involved in the synthesis was baked in an oven at 120 °C overnight prior to the use.

Syntheses of III-V QDs. Caution: phosphorus and arsenic precursors should be handled in an oxygen and moisture free environment since they are pyrophoric and will react with water. The QD syntheses were conducted under high pressure (900 psi, ultra high purity N_2 from Air Gas) with anhydrous octane as the solvent. For the syntheses of InP QDs, the concentration of $In(My)_3$ was 40 mM with 4 vol% TOP as a co-dissolving ligand, and the concentration of phosphorus precursor was 20 mM. For the syntheses of InAs QDs, the concentration of $In(My)_3$ was 60 mM with 4 vol% TOP, and the concentration of arsenic precursor was 20 mM. For all the studies, the total flow rate is set as 60 μL/min. The concentration ratio between indium and phosphorus precursors is adjusted by their flow rates. All the solution preparation was performed in a glove box. Pre-dried stainless steel syringes with valves were used to contain the precursor solutions for the synthesis. All the vials and needles involved in the solution preparation were baked in an oven at 120 °C overnight before being transferred to the glove box.

Appendix B

Early-Stage Indium Phosphide Growth Mechanisms

Table B 1: Comparison of the growth intermediates observed at different boundary conditions in all the AIMD simulations using HF/3-21G. * indicates that B3LYP/LACVP* is the method.

Systems	r_1, r_2 (Å)	t (ps)	Example Intermediates
2 $In(Ac)_3$	$r_1 = r_2 = 8$	24	$[In(Ac)_3]_2$
	$r_1 = 8, r_2 = 5$	17	
3 $In(Ac)_3$	$r_1 = r_2 = 8$	17	$[In(Ac)_3]_3$
	$r_1 = 8, r_2 = 5$	12.5	
$In(Ac)_3 + PH_3$	$r_1 = r_2 = 10$	30	No intermediates
$In(Ac)_3 + PH_3$*	$r_1 = r_2 = 10$	30	No intermediates
$In(Ac)_3 + 8\ PH_3$	$r_1 = r_2 = 8$	24	$In(Ac)_3 \bullet PH_3$
	$r_1 = 8, r_2 = 6$	21	$In(Ac)_2PH_2 \bullet HAc$
	$r_1 = 8, r_2 = 5$	20	$In(Ac)_2PH_2 \bullet HAc$
3 $In(Ac)_3 + 30\ PH_3$	$r_1 = r_2 = 10$	15	$In(Ac)_3 \bullet [In(Ac)_2]_2PH \bullet 2HAc$
	$r_1 = 10, r_2 = 7$	15	$[In(Ac)_3]_3 \bullet PH_3$
5 $In(Ac)_3 + 5\ PH_3$	$r_1 = r_2 = 7.5$	5.5	$[In(Ac)_3]_5$
6 $In(Ac)_3 + 6\ PH_3$	$r_1 = r_2 = 8$	40	$[In(Ac)_3]_3 \bullet [In(Ac)_2]_3P \bullet 3HAc$
	$r_1 = 8, r_2 = 5$	10	$[In(Ac)_3]_6 \bullet PH_3$
7 $In(Ac)_3 + 7\ PH_3$	$r_1 = r_2 = 8.5$	9	$[In(Ac)_3]_6 \bullet In(Ac)_2PH_2 \bullet HAc$
5 $In(^tBuCOO)_3 + 8\ PH_3$	$r_1 = 10, r_2 = 7$	7	$In(^tBuCOO)_2PH_2 \bullet {}^tBuCOOH$
	$r_1 = r_2 = 10$	5.5	$[In(^tBuCOO)_3]_5 \bullet PH_3$
$In(Ac)_3 + P(SiMe_3)_3$	$r_1 = r_2 = 10$	10	No intermediates
6 $In(Ac)_3 + P(SiMe_3)_3$	$r_1 = r_2 = 9$	9	$[In(Ac)_3]_6$
7 $In(Ac)_3 + P(SiMe_3)_3$	$r_1 = r_2 = 11$	12	$In(Ac)_2P(SiMe_3)_2 \bullet AcSiMe_3$

Table B 2: Single point energy comparison using B3LYP/LACVP* and ωB97X-D/LACVP* with geometries optimized at the level of B3LYP/LACVP*.

a) Structures in "intracomplex" dissociation – $In(Ac)_3 + PH_3$

Structures	B3LYP/LACVP*	ωB97X-D/LACVP*
Reactant	0 (reference)	0 (reference)
Intermediate	0.4	-1.0
TS	20.6	18.4
Product	12.5	8.9

Comment: The barrier predicted by ωB97X-D/LACVP* is about 1 kcal/mol lower than that predicted by B3LYP/LACVP* and the reaction energy is about 4 kcal/mol lower than that predicted by B3LYP/LACVP*.

b) Structures in "intracomplex" dissociation – $[In(Ac)_3]_2 + PH_3$

Structures	B3LYP/LACVP*	ωB97X-D/LACVP*
Reactant	0 (reference)	0 (reference)
Intermediate	4.9	2.6
TS	19.7	17.8
Product	12.3	8.5

Comment: The barrier predicted by ωB97X-D/LACVP* is about 2 kcal/mol lower than that predicted by B3LYP/LACVP* and the reaction energy is about 4 kcal/mol lower than that predicted by B3LYP/LACVP*.

c) Structures in "intercomplex" dissociation – $In(Ac)_3 \bullet PH_3 + In(Ac)_3$

Structures	B3LYP/LACVP*	ωB97X-D/LACVP*
Reactant	0 (reference)	0 (reference)
TS	3.8	0.4
Intermediate	-1.0	-6.5
TS	13.0	9.4
Product	8.0	3.0

Comment: The barrier predicted by ωB97X-D/LACVP* is about 2 kcal/mol higher than that predicted by B3LYP/LACVP* and the reaction energy is about 5 kcal/mol lower than that predicted by B3LYP/LACVP*.

Table B 3: Structural and charge comparison between $In(Ac)_3$ and $In(My)_3$ molecules.

Molecule	Method	In Charge	Average O charge	Average In-O distances (Å)
$In(Ac)_3$	HF/3-21G	1.98	-0.81	2.16
	B3LYP/LACVP*	1.98	-0.76	2.15
$In(My)_3$	HF/3-21G	1.98	-0.81	2.16
	B3LYP/LACVP*	1.98	-0.76	2.15

Table B 4: Frequencies of the optimized $In(Ac)_3$ structures (>50 cm^{-1}) using B3LYP/LACVP* and HF/3-21G

Method	Frequencies (cm^{-1})
B3LYP/LACVP*	52.77 69.71 80.79 84.57 88.07 94.27 152.61 179.79 195.94 197.88 201.73 218.78 266.70 321.17 324.05 460.64 461.39 472.49 623.51 629.15 632.50 710.50 714.11 719.12 974.64 978.86 980.86 1043.86 1045.83 1046.99 1086.14 1086.76 1087.29 1410.08 1410.92 1412.61 1480.94 1483.60 1486.66 1495.07 1497.77 1504.11 1519.55 1522.01 1526.23 1585.95 1586.91 1627.08 3073.60 3073.77 3076.38 3140.07 3144.80 3145.26 3186.07 3187.23 3187.59
HF/3-21G	48.85 49.63 65.88 96.11 97.01 122.11 172.14 204.41 204.91 228.34 228.71 250.34 320.17 392.47 392.78 488.61 488.96 506.40 677.49 685.88 687.95 758.64 760.19 776.03 1016.65 1016.89 1019.93 1138.90 1139.31 1142.87 1214.40 1215.89 1216.01 1553.68 1555.17 1566.15 1567.05 1567.96 1579.31 1585.28 1585.88 1597.59 1642.81 1643.16 1644.20 1657.11 1658.33 1670.18 3218.90 3223.67 3225.55 3282.41 3284.91 3291.97 3338.83 3341.38 3342.17

Table B 5: Charge change before and after the first P-H bond dissociation.

Charge	Before dissociation	After dissociation
P	0.08	-0.44
H1	0.10	0.62
In3	1.92	1.83
Other In	1.97~2.12	2.08~2.13

Table B 6: Charge change before and after the second P-H bond dissociation.

Charge	Before dissociation	After dissociation
P	-0.61	-1.15
H2	0.13	0.56
In1	2.02	1.95
In3	1.86	1.89
Other In	2.05 ~ 2.08	2.02 ~ 2.09

Table B 7: Charge change before and after the third P-H bond dissociation.

Charge	Before dissociation	After dissociation
P	-1.19	-1.49
H3	0.19	0.56
In1	1.92	1.95
In2	2.08	1.99
In3	1.97	1.97
In6	1.85	1.73
Other In	2.06~2.11	2.07

Table B 8: Data summary of the 100 optimized $[In(Ac)_3]_2$ complex structures taken from a 10 ps trajectory. (CB – chelating bidentate, PM – partial monodenate, FM – full monodentate, BB – bridging bidentate, CBB – chelating bridging bidentate. Energy unit: kcal/mol)

Struct.	CB	PM	FM	BB	CBB	ΔE	Struct.	CB	PM	FM	BB	CBB	ΔE
1	5	0	1	0	0	22	51	4	0	0	2	0	-14
2	5	0	1	0	0	21	52	4	0	0	2	0	-14
3	6	0	0	0	0	1	53	4	0	0	2	0	-13
4	6	0	0	0	0	1	54	4	0	0	2	0	-14
5	6	0	0	0	0	2	55	4	0	0	2	0	-11
6	6	0	0	0	0	2	56	4	0	0	2	0	-11
7	6	0	0	0	0	0	57	4	0	0	2	0	-14
8	6	0	0	0	0	0(ref.)	58	2	1	0	2	1	-15
9	5	0	0	0	1	-1	59	3	0	1	1	1	8
10	5	0	0	0	1	1	60	4	0	0	1	1	-14
11	5	0	0	0	1	-4	61	4	0	0	1	1	-11
12	3	0	0	1	2	-10	62	4	0	0	1	1	-15
13	3	0	0	1	2	-15	63	4	0	0	1	1	-13
14	4	0	0	0	2	-14	64	4	0	0	1	1	-15
15	4	0	0	1	1	-14	65	4	0	0	1	1	-15
16	4	0	0	1	1	-15	66	4	0	0	1	1	-15
17	4	0	0	2	0	-13	67	4	0	0	1	1	-14
18	4	0	0	1	1	-12	68	4	0	0	1	1	-15
19	3	0	0	2	1	-14	69	4	0	0	1	1	-14
20	3	0	0	2	1	-14	70	4	0	0	1	1	-14
21	3	0	0	2	1	-14	71	4	0	0	1	1	-15
22	3	0	0	1	2	-11	72	2	1	0	2	1	-12
23	3	0	0	2	1	-13	73	2	0	0	4	0	-21
24	3	0	0	1	2	-12	74	2	0	0	4	0	-21
25	2	0	1	2	1	0	75	2	0	0	4	0	-21
26	2	1	0	2	1	-11	76	2	0	0	4	0	-21
27	2	1	0	2	1	-14	77	2	0	0	4	0	-21
28	2	0	1	2	1	-8	78	2	0	0	4	0	-21
29	2	1	0	2	1	-14	79	2	0	0	4	0	-21
30	2	0	1	2	1	-8	80	2	0	0	4	0	-21
31	2	1	0	2	1	-15	81	2	0	0	4	0	-20
32	2	1	0	2	1	-14	82	2	0	0	4	0	-21
33	2	0	1	2	1	-12	83	2	0	0	4	0	-20
34	2	1	0	2	1	-10	84	2	0	0	2	2	-12
35	2	1	0	2	1	-10	85	2	0	0	4	0	-20
36	2	1	0	2	1	-10	86	2	0	0	4	0	-20
37	2	1	0	2	1	-10	87	2	1	0	2	1	-13
38	3	0	0	1	2	-10	88	2	0	0	3	1	-14
39	3	0	0	1	2	-15	89	2	0	0	2	2	-12
40	3	0	0	1	2	-14	90	2	0	0	4	0	-20
41	2	1	0	1	2	-13	91	2	0	0	4	0	-20
42	3	0	0	1	2	-14	92	2	0	0	3	1	-15
43	3	0	0	2	1	-14	93	2	0	0	4	0	-20
44	4	0	0	2	0	-13	94	2	0	0	4	0	-20
45	4	0	0	2	0	-13	95	2	0	0	3	1	-10
46	4	0	0	1	1	-13	96	2	0	0	2	2	-12
47	4	0	0	1	1	-12	97	2	1	0	2	1	-11
48	3	0	1	1	1	1	98	2	1	0	2	1	-12
49	4	0	0	1	1	-13	99	2	1	0	2	1	-13
50	4	0	0	1	1	-14	100	2	1	0	2	1	-12

Table B 9: P-H and O-H bond distances in the transition states

Distance (Å)	Intracomplex-$In(Ac)_3$	Intracomplex-$[In(Ac)_3]_2$	Intercomplex
P-H	1.62	1.64	1.65
O-H	1.34	1.32	1.29

Table B 10: Comparison of the affinity of $[In(Ac)_3]_2$ and $In(Ac)_3$ with one full-monodentate acetate towards PH_3 molecule and H atom. The relative energy is calculated referring to the sum of the energies of individual molecules.

Reaction	n = 1, ΔE (kcal/mol)	n=2, ΔE (kcal/mol)
$[In(Ac)_3]_n$ (mono)+ PH_3 → $[In(Ac)_3]_n$•PH_3	-7	-2
$[In(Ac)_3]_n$ (mono) + H → $[In(Ac)_3]_n$H	-20	-16
$[In(Ac)_3]_n$ (mono)+ PH_3 → $[In(Ac)_3]_nPH_2$•HAc	-8	1

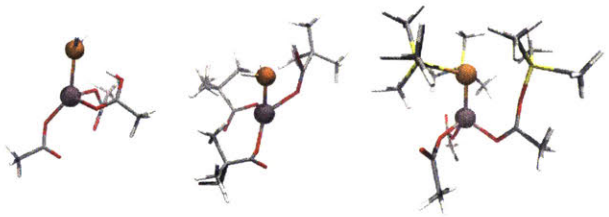

Figure B 1: Example intermediates observed during AIMD runs sampling the interaction between (a) $In(Ac)_3$ and PH_3, (b) $In(^tBuCOO)_3$ and PH_3 and (c) $In(Ac)_3$ and $P(SiMe_3)_3$ molecules.

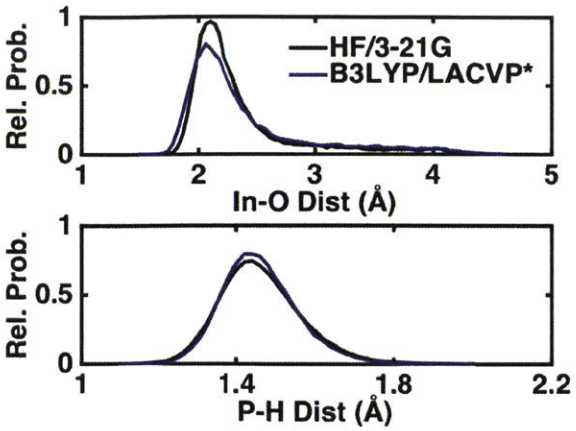

Figure B 2: Comparison of the radial distribution of In-O and P-H distances during two *ab initio* MD runs at HF-321G and B3LYP-LACVP* level of theory. The system contains one $In(Ac)_3$ and one PH_3 molecule.

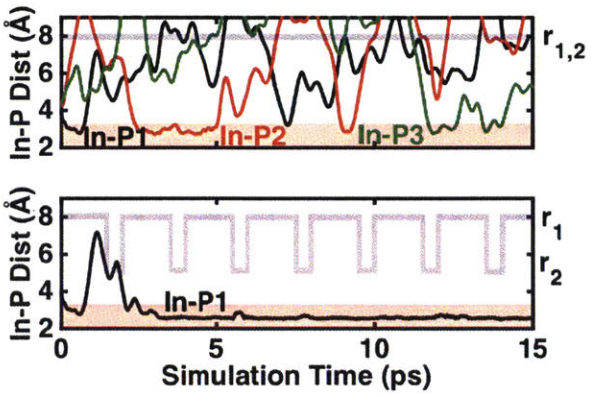

Figure B 3: Comparison of the In-P distance evolution during two AIMD runs with constant boundary condition (top panel) and periodically shrinking boundary condition (bottom panel). The system contains one indium acetate molecule and eight phosphine molecules. Only In-P distances of the reacting phosphine molecules are shown in the figure.

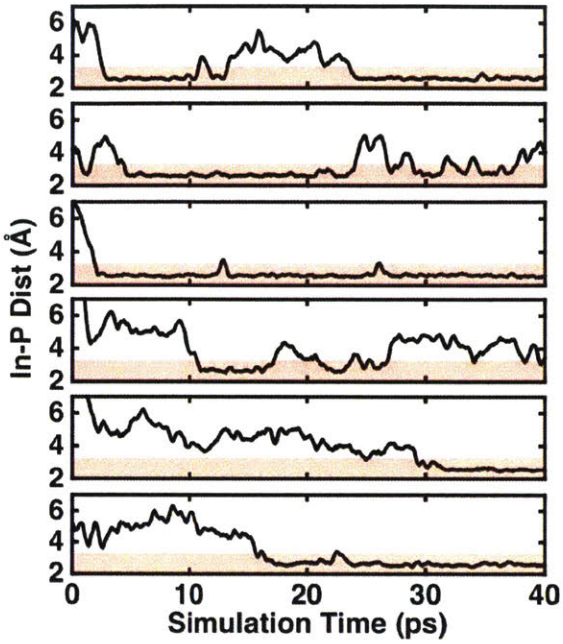

Figure B 4: Evolution of In-P distances during the cluster formation process. Only the six In-P bond distances between the reacting indium and phosphorus precursors precursor are shown. The data were smoothed for clarity.

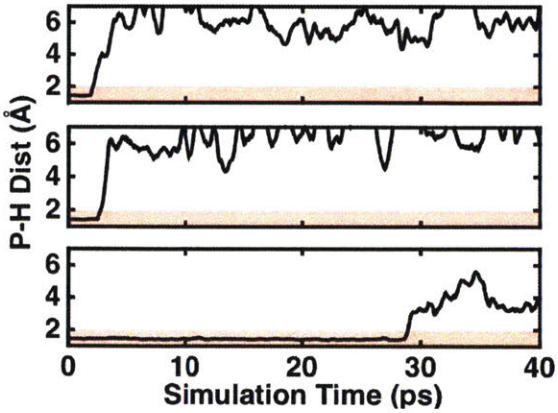

Figure B 5: Evolution of P-H bond distances in the reacting PH_3 molecules during the cluster formation process. The data were smoothed for clarity.

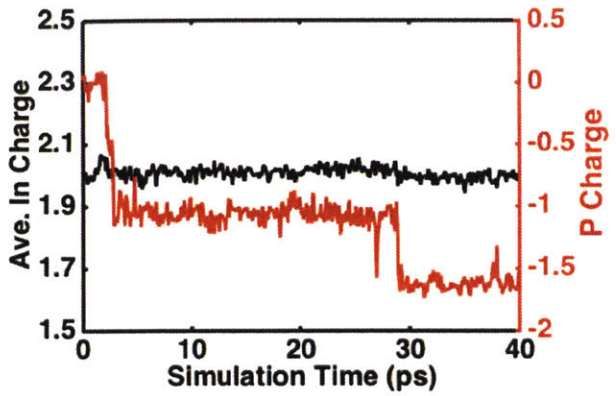

Figure B 6: Evolution of average charge of the six In atoms and the charge of the P atom in the reacting PH_3 molecule during the cluster formation process. Snapshots were taken every 0.1 ps for the NBO charge analysis at the level of B3LYP-LACVP* theory.

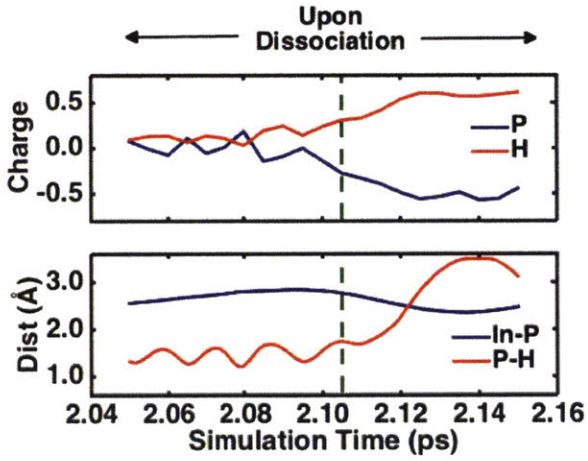

Figure B 7: Charge change of P and H atoms as well as the distance change of In-P and P-H bonds during the first P-H bond dissociation event. The charges are plotted every 5 fs and the distances are plotted every 0.5 fs.

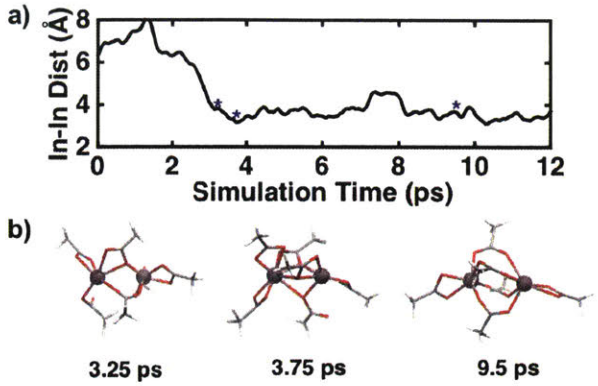

Figure B 8: a) The evolution of In-In distance from an AIMD simulation containing two $In(Ac)_3$ molecules at constant boundary conditions (r_1 = 8Å). b) Example snapshots taken the trajectory indicating the formation of $[In(Ac)_3]_2$ complex with the two indium atoms connected by two, three and four acetates.

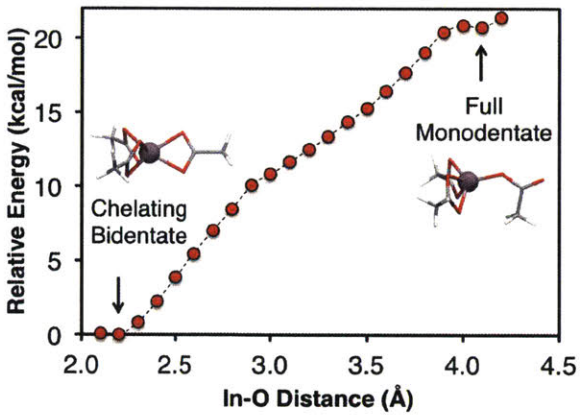

Figure B 9: Reaction pathway obtained from constrained optimization for the transition between a chelating-bidentate acetate to a full-monodentate acetate in $In(Ac)_3$. The labeled structures are local minima after relaxation.

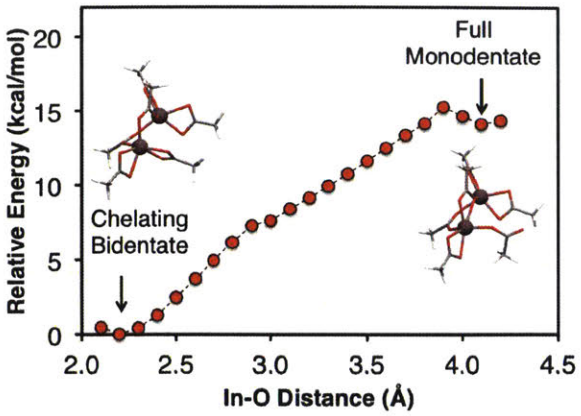

Figure B 10: Reaction pathway obtained from constrained optimization for the transition between a chelating-bidentate acetate to a full-monodentate acetate in $[In(Ac)_3]_2$. The labeled structures are local minima after relaxation.

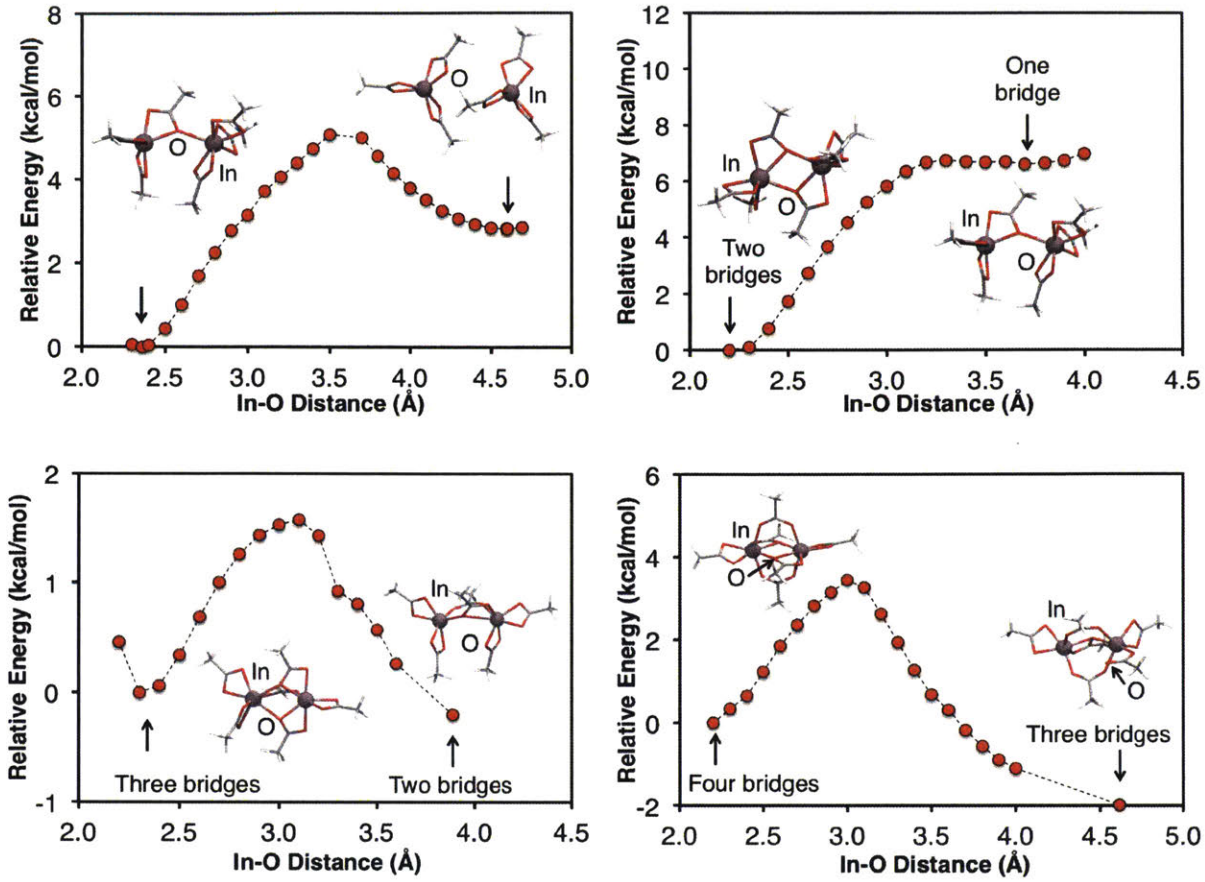

Figure B 11: Reaction pathway obtained from constrained optimization for the transition between $[In(Ac)_3]_2$ complexes with different number of bridges.

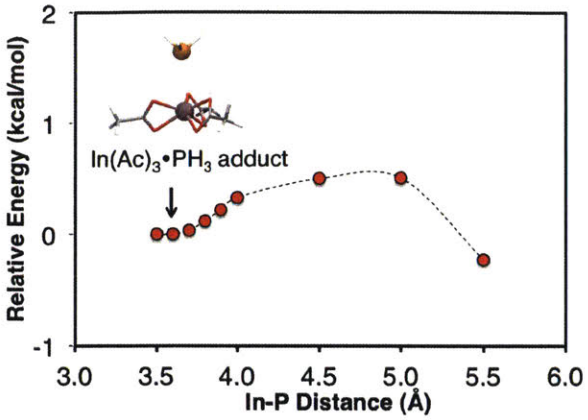

Figure B 12: Reaction pathway for the adduct formation between one PH_3 molecule and one $In(Ac)_3$ molecule obtained from constrained optimization. The labeled structure is a local minimum after relaxation.

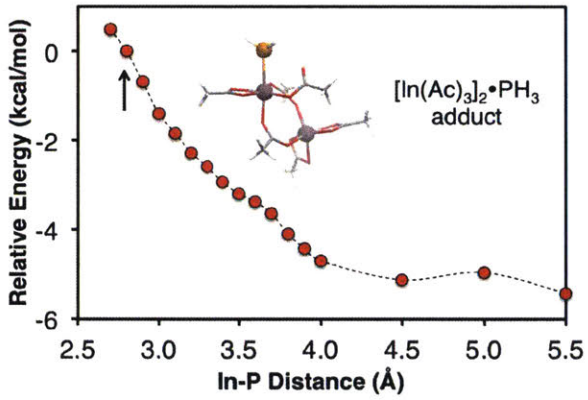

Figure B 13: Reaction pathway for the adduct formation between one PH_3 molecule and one $[In(Ac)_3]_2$ molecule obtained from constrained optimization. The labeled structure is a local minimum after relaxation.

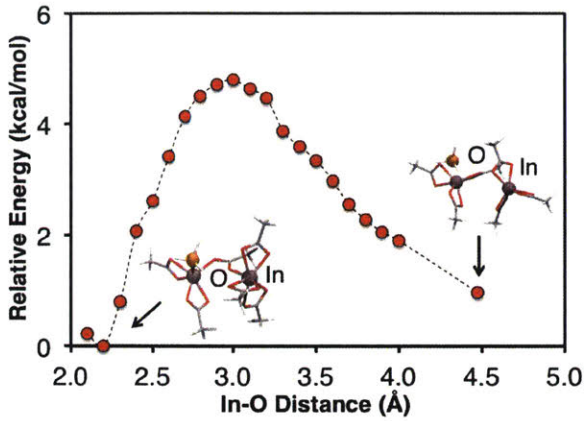

Figure B 14: Reaction pathway for the agglomeration between an $In(Ac)_3 \square PH_3$ adduct and an $In(Ac)_3$ obtained from constrained optimization. The labeled structure is a local minimum after relaxation.

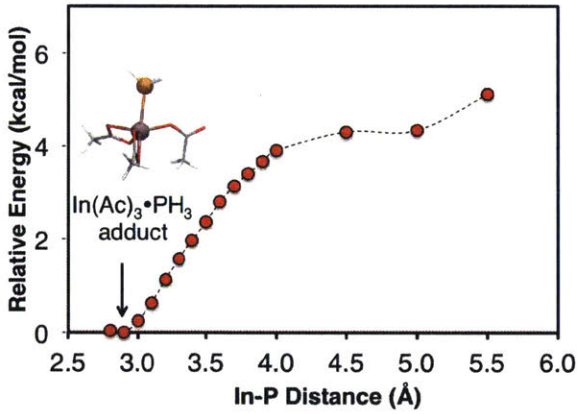

Figure B 15: Reaction pathway for the adduct formation between one PH_3 molecule and one $In(Ac)_3$ molecule with one full monodentate acetate obtained from constrained optimization. The labeled structure is a local minimum after relaxation

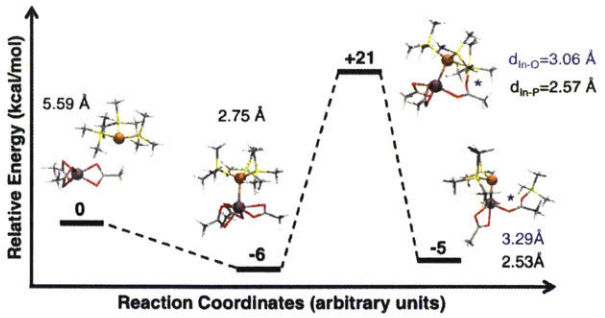

Figure B 18: The dissociation process of the first P-Si bond in the "intracomplex" pathway that is started with one $P(SiMe_3)_3$ molecule and an $In(Ac)_3$ molecule.

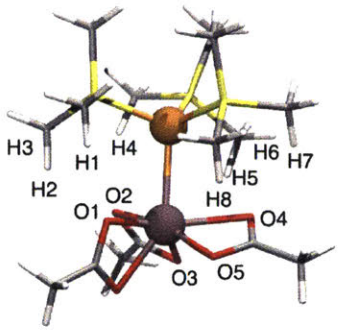

H-O	Distance (Å)
H1-O1	2.55
H2-O1	2.67
H2-O2	2.85
H3-O2	2.99
H4-O2	2.59
H5-O3	2.85
H5-O4	2.81
H6-O4	2.95
H7-O4	2.47
H8-O5	2.63

Figure B 19: Possible C-H...O hydrogen bonding interactions (H-O distance < 3.0 Å) in the $In(Ac)_3 \bullet P(SiMe_3)_3$ adduct.

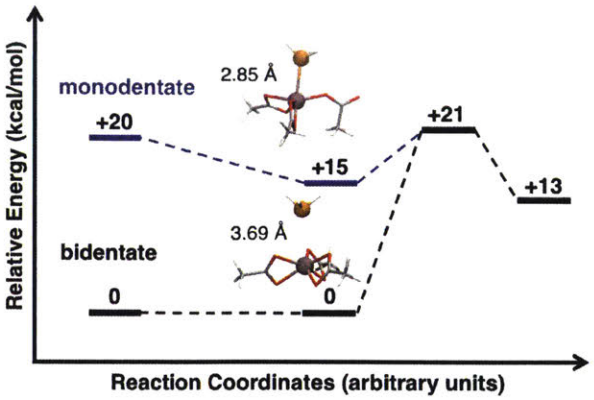

Figure B 16: The dissociation process of the first P-H bond in the "intracomplex" pathway that is started with one PH_3 molecule with either a monodentate or bidentate $In(Ac)_3$ molecule.

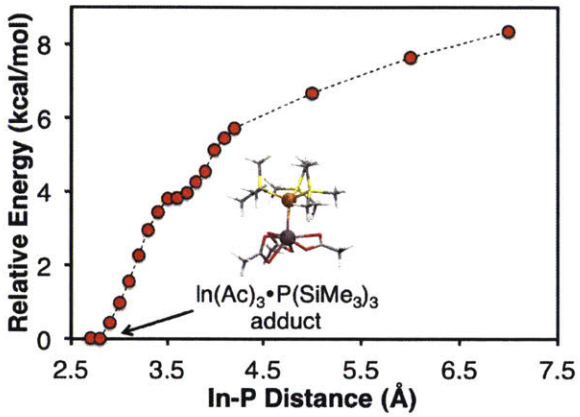

Figure B 17: Reaction pathway for the adduct formation between one $P(SiMe_3)_3$ molecule and an $In(Ac)_3$ molecule obtained from constrained optimization. The labeled structure is a local minimum after relaxation.

Appendix C

Cluster-Mediated Growth of Indium Phosphide Quantum Dots

Experimental Details

Chemicals. Indium acetate (99.99% metals basis) was purchased from Alfa Aesar. Trioctylphosphine (min, 90%), trioctylphosphine oxide (99%) and tris(trimethylsilyl)phosphine (10 wt% in hexane, >98%) were purchased from Strem Chemicals. Myristic acid (>99%), 1-octadecene (technical grade, 90%), toluene (anhydrous, 99.8%), hexane (anhydrous, 95%), *trans*-2-[3-(4-*tert*-Butylphenyl)-2-methyl-2-propenylidene]malononitrile (DCTB) (≥98%), ferrocene (98%) and potassium tert-butoxide (sublimed grade) were purchased from Sigma Aldrich. Toluene-d_8 (D, 99.5%) was obtained from Cambridge Isotope Laboratories, Inc. Bio-Beads S-X1 GPC medium was purchased from Bio-Rad Laboratories, Inc. UV-Vis spectra were taken in Shimadzu UV-3101PC UV-VIS-NIR scanning spectrometer. All the synthetic or analytical procedures of InP QDs were performed under nitrogen or vacuum in a Schlenk line or glove box.

Synthesis of $In(My)_3$. In a typical synthesis, 10.3 mmol $In(Ac)_3$ (3 g) and 31.1 mmol pre-dried MA (7.10 g) were mixed in 40 mL pre-dried 1-octadecene in a glove box. The mixture was transferred to a Schlenk line and heated up to 110 °C to form a clear solution under vacuum (90 mtorr) for three hours. The reactant solution was maintained under argon and then cooled down to room temperature. Protected under argon, the slurry was transferred into the glove box and

washed with anhydrous hexane 6 times. The white solids were vacuum dried overnight, stored in the glove box.

HT/HP synthesis of InP QDs. Caution: Air free handling of $P(SiMe_3)_3$ solution is required since $P(SiMe_3)_3$ is pyrophoric. Similar to previous studies[133], the synthesis of InP QDs was performed at 900 psi with the temperatures ranging from 105 – 300 °C under inert conditions. Anhydrous toluene was chosen as the solvent. In general, indium precursor stock solution was prepared by adding 1.5938 g $In(My)_3$ and 2 mL TOP into 48 mL toluene (40 mM In, 4 vol% TOP). Phosphorus precursor solution was prepared by adding 3.75 mL 10 wt% $P(SiMe_3)_3$ in hexane into 46.25 mL toluene (20 mM P). Two syringe pumps were used to pump indium and phosphorus precursors with identical flow rates. Therefore, the In/P ratio was set as 2 for all conditions.

Calculation of residence time in HT/HP reactors: Calculation of residence time in the HT/HP reactors should include the effect of solvent expansion at high temperatures. According to the NIST website[164], the densities of toluene at 22 °C, 240 °C and 270 °C at 900 psi are 0.8697 g/mL, 0.6415 g/mL and 0.5958 g/mL. Since the fluids are pumped at 22 °C, the residence time can be calculated using the following formula:

$$\tau = \frac{V_{\text{reactor}} / F_{\text{total}}}{\rho_{22°C} / \rho_T}$$

Where V_{reactor} is the heated reactor volume (e.g., μL), F_{total} is the total flow rate (e.g., μL/min), $\rho_{22°C}$ is the density of toluene at 22 °C and ρ_T is the density of toluene at T °C.

Table C 1. Example residence time calculations in a 355 μL rector

Conditions	Residence time / min
30 μL/min, 270 °C	8.1
40 μL/min, 270 °C	6.1
60 μL/min, 270 °C	4.1
20 μL/min, 240 °C	13.1
30 μL/min, 240 °C	8.7
40 μL/min, 240 °C	6.5
60 μL/min, 240 °C	4.4
120 μL/min, 240 °C	2.2
180 μL/min, 240 °C	1.5

Batch syntheses of InP QDs. Caution: Air free handling of $P(TMSi)_3$ solution is required since $P(TMSi)_3$ is pyrophoric. The batch synthesis procedure was adapted from literature[41]. 358.5 mg $In(My)_3$ (0.45 mmoles) was added to 9 mL 1-ODE in a 3-neck flask. The reaction mixture was heated at 110 °C under vacuum for 45 min. The atmosphere was switched to N_2 and the temperature was raised to 150 °C. 93.75 mg $P(TMSi)_3$ (0.375 mmoles) dissolved in 2.25 mL TOP were swiftly injected into the flask and the temperature was raised to 230°C. 1 mL aliquots were taken at 1 min (150 °C) and 14 min (230°C). These samples were transferred into a glove box and purified using GPC before MALDI characterization. As this batch synthesis utilized 1-ODE as the solvent, which permanently damages the GPC column, a freshly packed GPC column was used for both samples.

Purification of InP QDs by GPC. The preparative GPC column was packed inside a glove box following a previous reported procedure[158]. 4 g of Bio-beads were first swollen in anhydrous toluene overnight. All of the swollen beads were then transferred to a glass column with a filter and glass fret disk. After the gel settled down and formed a column with approximately 28 mL volume, a small layer of sand was carefully placed at the top of the column and anhydrous toluene was used to rinse the column. The as-synthesized InP QDs in toluene from the HT/HP

reactor system were first concentrated in a Schlenk line and then transferred into the glove box. A portion of the InP QD sample (less than 1 mL) was then injected into the column with anhydrous toluene as the eluent, and all the purified samples were collected when the elution volume was close to 1/3 of the total volume of the column. The column was carefully rinsed before the next injection. The purified samples were used for further MALDI MS, NMR and STEM characterization.

MALDI Characterization. MALDI-TOF mass data were collected on a Bruker Microflex MALDI-TOF mass spectrometer in the Biopolymers and Proteomics Laboratory in Koch Institute at MIT. DCTB was used as a matrix and the concentration of the stock solution is 78 mM in toluene (i.e., 10 mg in 0.5 mL toluene). Purified InP growth mixtures were diluted so that their absorbance at 310 nm was about 0.05-0.25 AU. The matrix solution and InP solution was mixed in a 1:1 volume ratio to maximize the mass signal detection. The sample-matrix mixture was then spotted onto a MALDI plate in a glove box. The plate was sealed in a home-made box under N_2 and then loaded into the mass spectrometer for characterization. Desorption and ionization of InP growth mixtures were achieved by absorbing pulsed nitrogen laser. For low mass characterization, tripsinogen was used as the external standard (11999 and 23981 Da) to calibrate the spectrometer and the laser intensity was set between 20-30% for sample characterization. The detector gain (linear detector, positive mode) was set as 7.2x. For high mass characterization, albumin (bovine serum, BSA) was used as the external standard (33216 and 66431 Da) for the calibration and the laser intensity was set between 30-40% for sample characterization. The detector gain (linear detector, positive mode) was set as 20.0x. No background subtraction was performed on the spectra. The mass spectra were smoothed with simple average of 10 data points.

NMR analysis of QDs. The quantitative ^{1}H NMR spectra was recorded on Bruker Avance-400 NMR spectrometer with ferrocene as the internal standard and 30 s relaxation delay. ^{31}P NMR spectra were recorded on Varian Inova-500 NMR spectrometer. All of measurements on the air-sensitive InP QDs were performed in a J-Young NMR tube.

Mass Weighing. 1 mL concentrated purified InP QD solution with a known absorption spectra was carefully pumped dry under vacuum. The mass of the dried QD sample was recorded on an electrobalance (MC 215, Sartorius). The mass of each sample was close to 15 mg and the mass values were measured multiple times to ensure accuracy.

STEM Characterization of InP QDs. The scanning transmission electron microscope (STEM) samples were prepared by drop casting the solutions containing the purified InP QDs onto a carbon coated 200-mesh holey TEM copper grid. The copper grid was dried and kept in a dry pumped vacuum specimen box. Afterwards the grid was loaded into a double-tilt sample holder. Aberration corrected scanning transmission electron microscopy (Cs-corrected STEM) images were acquired at LMA-INA-UNIZAR using a high angle annular dark field detector in a FEI XFEG TITAN electron microscope operated at 300 kV equipped with a CETCOR Cs-probe corrector from CEOS Company allowing formation of an electron probe of 0.08 nm.

XPS Characterization of InP QDs. To mimic the conditions used for MALDI characterization, after GPC purification, we drop casted concentrated InP QD samples onto a gold electrode, and used vacuum to remove the solvent. The gold electrode was then stored in a home-made box, sealed under nitrogen and brought to the XPS measurement. XPS measurements were performed on PHI Versaprobe II XPS.

Small clusters observed with different solvents and precursors

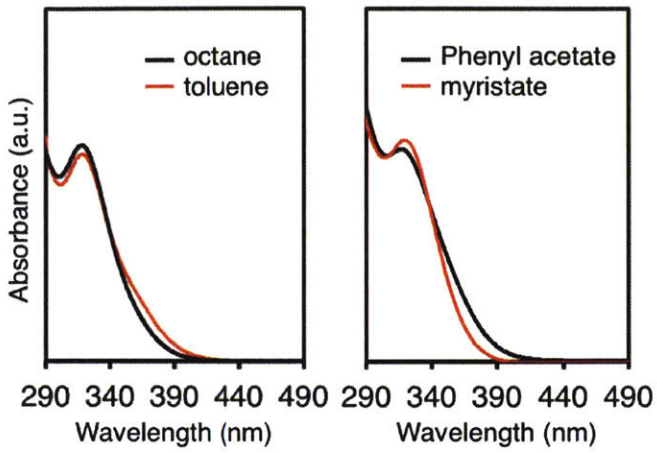

Figure C 1: Formation of clusters with first absorption peak at 320 nm with different solvents (left) and indium precursors (right). The solvent study was performed in a tube reactor at 30 °C. The flow rate of both precursors is set as 20 μL/min. The precursor study was performed in a vial by injecting 1 mL phosphorus into 1 mL indium at 22 °C in a glove box. The aliquot was taken at 10 min for indium myristate, and at 24 hr for indium phenyl acetate.

Evolution of medium clusters at different growth temperatures and times

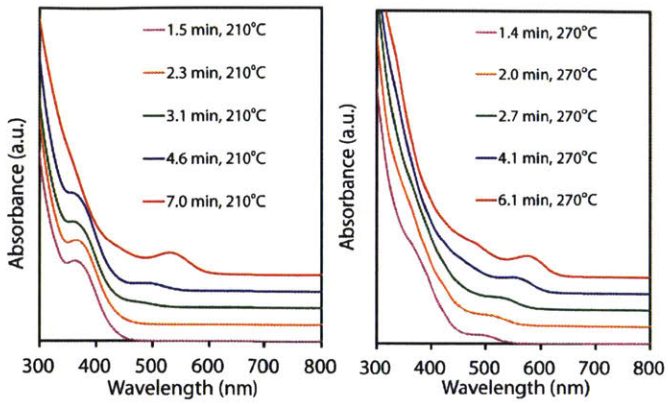

Figure C 2: UV-Vis spectra of InP growth trajectories synthesized at 210 °C and 270 °C under different growth times in the HT/HP tube reactor. The growth time is adjusted by changing the flow rate of the precursors. For growth at 210 °C, the 360 nm absorption features of clusters are not visible after 4.6 minutes of growth. For growth at 270 °C, the absorption features of clusters are not visible after 2.0 minutes of growth.

Example InP QDs synthesized from HT/HP reactors

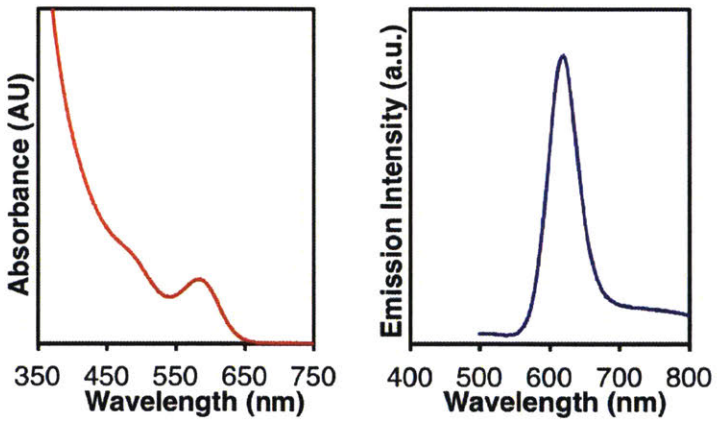

Figure C 3: Example absorption and PL measurement of InP QDs. The corresponding QDs emit at 619 nm and the emission line width (FWHM) is 52 nm. Generally the as-synthesized InP QD exhibit very low quantum yields (fractions of a percent) and show a significant amount of red-shifted trap emission which is in good agreement with other literature on InP core-only QDs.

GPC purification efficiency

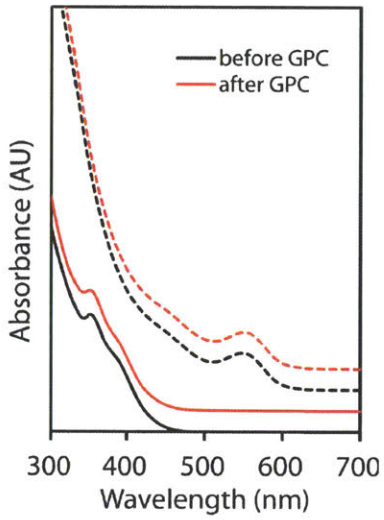

Figure C 4: Example UV-Vis absorption spectra of clusters and QDs before and after GPC purification.

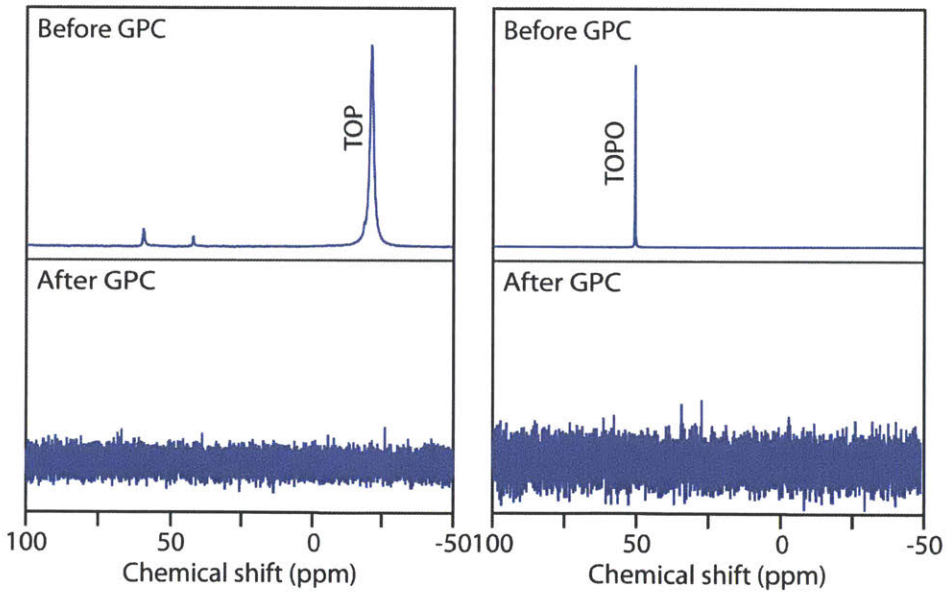

Figure C 5: ^{31}P NMR spectra showing the completely removal of TOP (left) and TOPO (right) in two example samples of InP QDs using GPC.

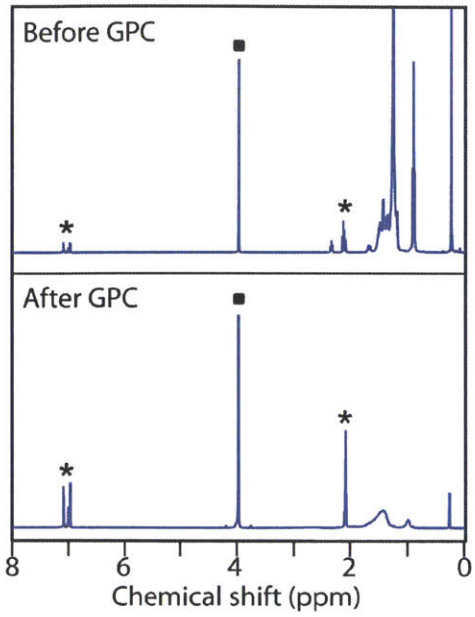

Figure C 6: ^{1}H NMR spectra of InP QDs before and after GPC purification. The asterisks marked in the spectra indicate peaks associated with the toluene solvent. The square indicates the signal from the internal standard ferrocene. After GPC, the proton-to-particle ratio decreased by 94%.

Oxygen-free InP QDs

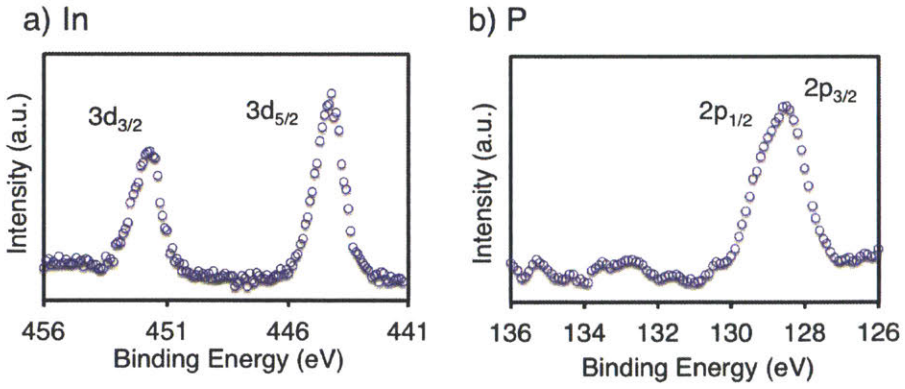

Figure C 7: XPS Characterization of InP QDs. We used XPS to study the oxidation level of InP QDs prepared by the one-solvent protocol. The InP QD sample was synthesized using TOP as coordination ligands and purified by GPC. XPS has been widely used to characterize the

oxidation of phosphorus in InP QDs.

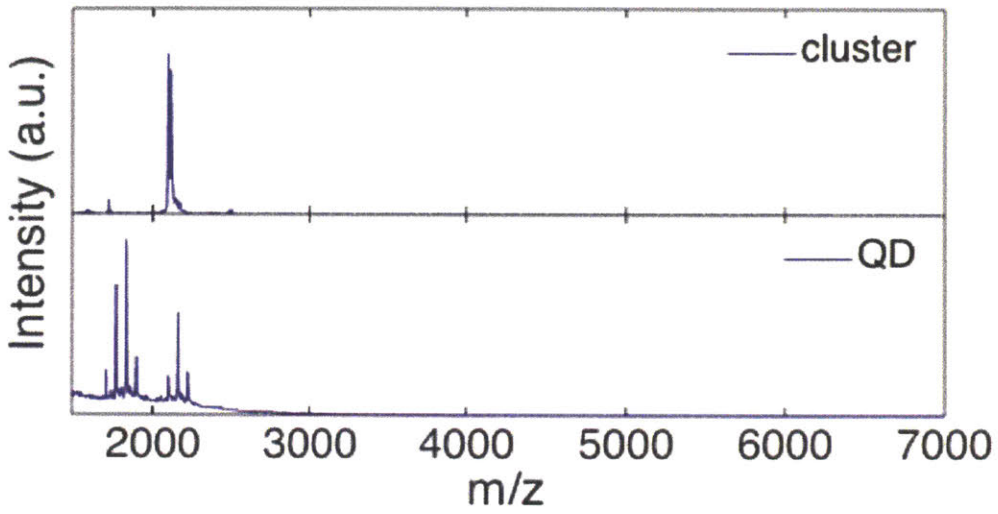

Figure C 8: MALDI low mass (1.5 - 7 kDa) characterization of cluster mixtures and QDs. For the cluster mixture sample, we attribute to observed peaks as indium precursors[133] that are desorbed from the cluster surface due to the thermal heating in the characterization. For the QDs ("cluster-free"), different from the signal of the cluster mixture sample, there is a clear pattern among the peaks and the mass difference between each peak is around 62 Da, which should be two P atoms. Therefore, these signals are attributed to the fragmentation of QDs. As we shown in a), QDs can be fragmented depending on the intensity of laser powers. We have considered the inaccuracy caused by the fragmentation in the calculation of the extinction coefficients.

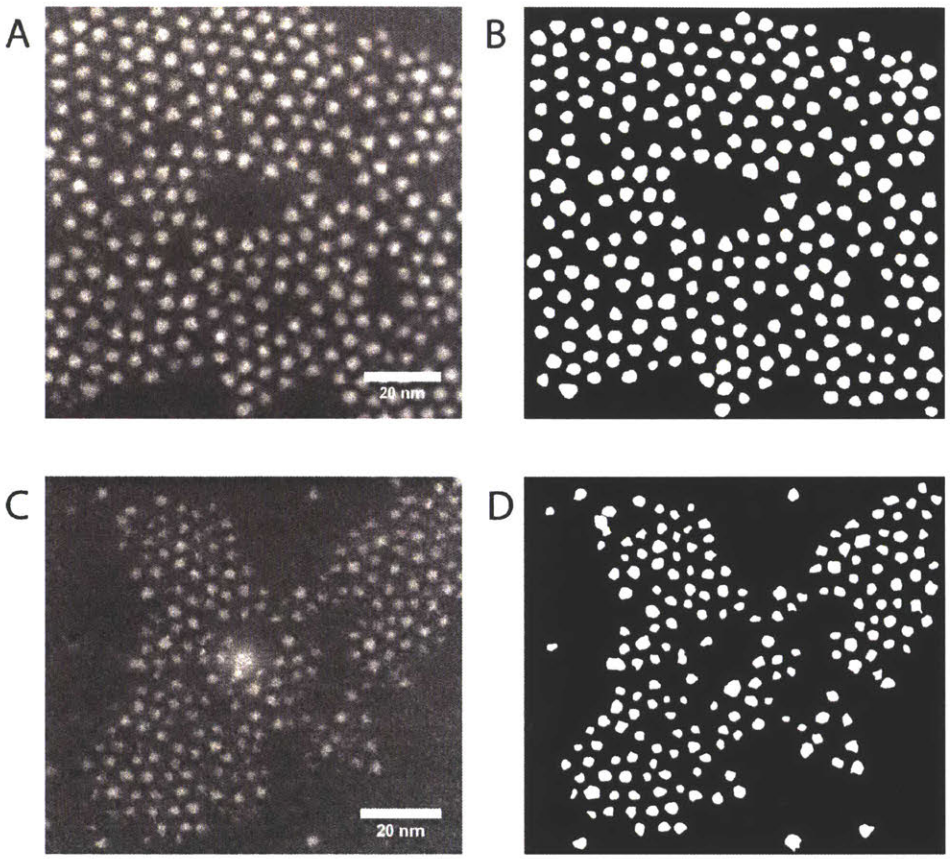

Figure C 9: Size analysis of the particles by STEM-HAADF: the sizes of the particles were analyzed through imageJ.[87] B and D display the binary count mask of the A and C. The average projected area of the InP QDs in A is 10.4 nm^2 based on the analysis of 262 different particles. And the average projected area of InP QDs in C is 5.9 nm^2 based on the analysis of 379 different particles (for the InP sample shown in C, another image with the same magnification is also analyzed, but not displayed).

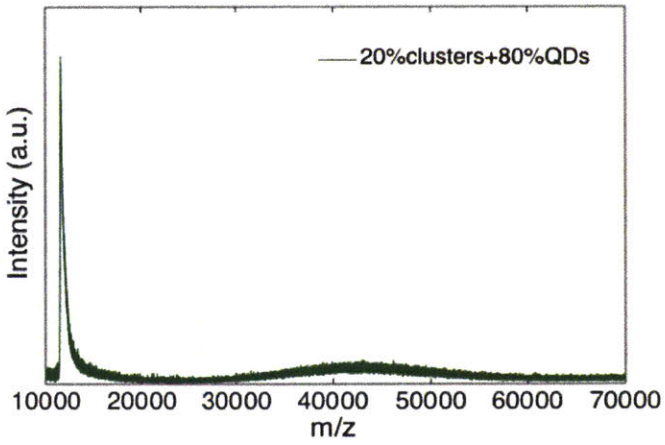

Figure C 10: MALDI Characterization of cluster and QD mixtures. The clusters are intentionally mixed with QDs. The absorbance at 310 nm of the added clusters is a quarter of that of the added QDs.

Appendix D

Effect of Water

Experimental Details

Chemicals. Indium acetate (99.99% metals basis) was purchased from Alfa Aesar. Trioctylphoshine(min, 90%), trioctylphosphine oxide (99%), tris(trimethylsilyl)phosphine (10 wt% in hexane, >98%) and trimethyl indium (98%) were purchased from Strem Chemicals. Hexane (extra dry, 99.9%) was purchased from Acros Organics. Myristic acid (>99%), 1-octadecene (technical grade, 90%), hexane (Laboratory Reagent, ≥95%), octane (anhydrous, ≥99%), dichloromethane (anhydrous, ≥99.8%), ethanol (anhydrous), and potassium tert-butoxide (sublimed grade) were purchased from Sigma Aldrich. The UV-Vis absorbance measurement of InP QDs was conducted on an HP 8453 spectrometer. FT-IR characterization of the $In(My)_3$ precursors was collected on Nicolet 6700 FT-IR instrument (Thermo Scientific). The ESI mass spec data were collected on Bruker APEXIV 4.7t FT-ICR-MS (Fourier-Transform Ion Cyclotron Resonance Mass Spectrometer) equipped with Bruker APOLLO ESI source. HR-TEM images were collected using a JEOL 2010 operating at 200 kV. XRD data were collected using Rigaku Smartlab in a capillary.

HT/HP reactors. The system including silicon-based chip reactors (2-stage and 3-stage) is similar to that reported previously[53, 55]. The tube reactors were made out of smooth-bore seamless stainless steel tubes (type 316, ID 0.022 inch, purchased from McMaster-Carr). Two syringe pumps (Harvard apparatus) were used for solution injections. All connections, tubes, and devices were made out of type-316 stainless steel, and heating cartridges were made of

multipurpose aluminum. The heated volumes of the individual stages were comparable for the two-stage chip and tube reactor systems. In a typical synthesis, the flow rates of the indium and phosphorus precursors were both set as 30 μL/min, with a residence time at each stage 2~3 min.

Syntheses of $In(My)_3$. Caution: $In(CH_3)_3$ is highly pyrophoric and reactive towards moistrure. It should be handled in an air and moistrure free enviroment with great care. Generally, the procedure to synthesize $In(Ac)_3$-derived $In(My)_3$ is as follows: in a Schlenk line, 10 mmol $In(Ac)_3$ (2.93 g) and 30 mmol MA (7.00 g) were mixed in 15 mL 1-octadecene and heated up to 110 °C to form a clear solution under vacuum (< 100 mtorr) for three hours. The reactant solution was maintained under argon and then cooled down to room temperature and white solids precipitated. The solid was washed with hexane 4 times, vacuum dried overnight and then stored in a N_2-filled glove box. The procedure for $In(CH_3)_3$-derived $In(My)_3$ is as follows: in a N_2-filled glove box, 6 mmol $In(CH_3)_3$ (1.00 g) and 19 mmol MA (4.30 g) were dissolved in 20 mL anhydrous diethyl-ether individually. Droplets of the $In(CH_3)_3$ solution were added to the MA solution. The mixture was stirred for an hour along with bubble formation. The solution was sealed under N_2 and stored at -20 ℃ overnight. Afterwards it was vacuum dried, washed with anhydrous hexane 4 times, vacuum dried overnight and then stored in a N_2-filled glove box. All the glassware involved in the synthesis was baked in an oven at 120 °C overnight prior to the use.

Syntheses of InP QDs. Caution: $P(TMSi)_3$ solution should be handled in an oxygen and moisture free enviroment since it is pyrophoric and will react with water. InP QD syntheses were conducted under high pressure (900 psi, ultra high purity N_2 from Air Gas) with anhydrous octane as the solvent to enhance mixing in the flow reactors. For all the studies, the concentration of $In(My)_3$ was 40 mM in octane with 4 vol% trioctyl-phosphine (TOP) as a co-dissolving

ligand, and the concentration of $P(TMSi)_3$ was 20 mM in octane. The flow rates of the indium precursors and phosphorus precursrs were both set at 30 μL/min. All the solution preparation was performed in a glove box. Pre-dried stainless steel syringes with valves were used to contain the precursor solutions for the synthesis. All the vials and needles involved in the solution preparation were baked in an oven at 120 °C overnight before being transfered to the glove box.

Water Measurement. Water content was measured using KF on a C20 Coulometric KF Titrator (Mettler Toledo). The titration reagent was HYDRANAL®-Coulomat AG-H, purchased from Sigma Aldrich. Water content measurements were conducted on the chemicals involved in the synthesis of $In(My)_3$ and InP QDs except $In(Ac)_3$, $In(CH_3)_3$, TOP and $P(TMSi)_3$ due to solubility and instrument compatibility issues. Before the titration, all the solutions were kept under an inert atmosphere. Generally, 1 mL of the sample was injected to the KF titrator, and the measurement was repeated 2~3 times. The direct measurement results were in the unit of ppm and we converted it to (water/$In(My)_3$) for illustration purposes (see section C in SI). The procedures to measure the water content were straightforward. For the case of $In(My)_3$, it was mixed with octane in a glove box first. The KF titration was conducted outside of the glove box after the solution had been heated up by a heat gun due to the low solubility of $In(My)_3$ in octane at room temperature. Samples that were doped with additional water were first stirred overnight. Part of the solution was used for the measurement while part of it was used for QD synthesis after addition of TOP. The doped water amount plus the original water amount in the solution matched well with the measured water amount.

Base Addition. Bases were added directly to the 40 mM $In(My)_3$-TOP-octane solution, which had been stirred overnight before the InP QD synthesis. KO^{t}Bu was chosen due to the large pKa of its conjugate acid, although it is a solid base. Attention was paid to make sure the whole

operation was in an inert environment. For the case of KO^{t}Bu, solids were filtered out after stirring overnight followed by QD synthesis

Particle concentration estimation

We used the absolute absorbance at 310 nm to qualitatively compare the reaction yield for the InP synthesis. We also applied Beer's Law to approximate the particle concentration at the first absorption peak. The molar extinction coefficient was estimated based on the sizing curve of InP QDs with respect to the first absorption peak and the relationship between the particle size and molar particle extinction coefficient from Xie et al.'s study.[134] The precursors concentration was 20 mM $In(My)_3$ and 10 mM $P(TMSi)_3$ during our synthesis. The as-synthesized InP QDs were diluted ~40 times for the absorbance measurement. The light path was 1 cm.

Table D 1: Absolute absorbance at 310 nm and particle concentration estimation at different water contents and growth time.

water/$In(My)_3$	0.015		0.142	
(mol/mol)	2-stage reactor	3-stage reactor	2-stage reactor	3-stage reactor
A_{310}/a.u.	3.0	3.1	2.8	3.1
λ_{max}/nm	600	620	547	551
A_{max}/a.u.	0.11	0.13	0.31	0.29
D_{max}/nm	3.3	3.7	2.5	2.5
$c_{max} \times 10^3$/mM	4	3	36	31

* A_{310} is the absolute absorbance at 310 nm, λ_{max} is the wavelength at the first absorption peak, A_{max} is the absolute absorbance at the first absorption peak, D_{max} is the calculated particle size based on the first absorption peak and c_{max} is the calculated the particle concentration. For a two-stage reactor, the temperature of the first stage is 130 °C while the temperature of the second stage is 270 °C; for a three-stage reactor, the temperature of the first and second stage is 130 °C and 220 °C while the temperature of the third stage is 270 °C.

Water Measurement Results

We measured the water content of different batches of $In(My)_3$ (Table S2) by Karl Fischer titration (C20 Coulometric KF Titrator from Mettler Toledo). The titration reagent was

HYDRANAL®-Coulomat AG-H (Sigma Aldrich). The concentration of $In(My)_3$ was 40 mM in solution in all measurements. The direct measurement results were in the unit of ppm, which was converted to the molar ratio between water and $In(My)_3$. For batch S1 and S5, the ODE and MA used were dried and stored in a glove box. The $In(Ac)_3$ used was newly purchased and stored in a glove box. For batch S3 and S6, ODE and MA were used as received and $In(Ac)_3$ was newly purchased and stored in a desiccator. For S4, ODE and MA were used as received and $In(Ac)_3$ was stored in a desiccator for over half a year. For each sample, the water content was measured 2~3 times and the average value was reported. The measured water content did not vary significantly for samples prepared on different days.

Table D 2: Water measurement for different batches of $In(My)_3$

$In(My)_3$ (40mM)	Treatment	Water content (ppm) (water/$In(My)_3$ (mol/mol))
S1	Purified and dried (in anhydrous octane)	63 (0.065)
S2 (via $In(CH_3)_3$)	Purified and dried (in anhydrous octane)	15 (0.015)
S3	Purified and dried (in anhydrous octane)	83 (0.085)
S4	Purified and dried (in anhydrous octane)	178 (0.183)
S5	100mM in ODE after synthesis (diluted in anhydrous octane)	160 (0.164)
S6	100mM in ODE after synthesis (diluted in anhydrous octane)	184 (0.189)
S7 (via $In(CH_3)_3$)	Purified and dried (in anhydrous octane)	23 (0.024)

We also measured the water content of different chemicals associated with $In(My)_3$ and InP QD synthesis by Karl Fisher (Table S3). $In(Ac)_3$ was attributed as the water source based on our water measurement results of other associated chemicals including ODE and MA for the $In(My)_3$

synthesis, hexane (on bench) for the purification and anhydrous octane as the carrier solvent for the K-F measurement.

Table D 3: Water measurement for all the chemicals associated with $In(My)_3$ and InP synthesis

Materials	Water content (ppm)
ODE (on bench)	12.4
ODE (at synthesis condition)	8.8
Anhydrous octane in glove box	2.5
Hexane (on bench)	13.4
MA in bench hexane (90 mM)	13.9
MA* in anhydrous octane (90 mM)	3.5
Anhydrous hexane in glove box	1.4
Anhydrous diethyl ether in glove box	69

* MA was heated to the synthesis condition under vacuum for 2~3 hours and then transferred and stored in the glove box.

Effect of Molecular Sieves

We investigated the effect of the molecular sieve treatment to the indium precursors on the growth of InP QDs. K-F titration showed an increase of water content after the treatment. The increased water content can only be explained as the incomplete removal of water during the activation of molecule sieves, although the molecular sieves we prepared were able to dry common solvents such as toluene and THF, and we have prepared the molecular sieves in a standard way (dried under vacuum oven at 180 °C overnight). Nevertheless, the increasing amount of water is not sufficient to explain the drastic blue shift of the absorption spectrum. We attribute the effect of molecule sieves to its basicity, as they have been observed to act as solid base in non-aqueous media.[165] With a longer time of treatment, more indium precursors have been hydrolyzed, thus resulting in a blue shift. This observation is in agreement with our hypothesis in the main text. The same molecular sieve effect was observed for $In(My)_3$ synthesized in different batches and in both reactor systems.

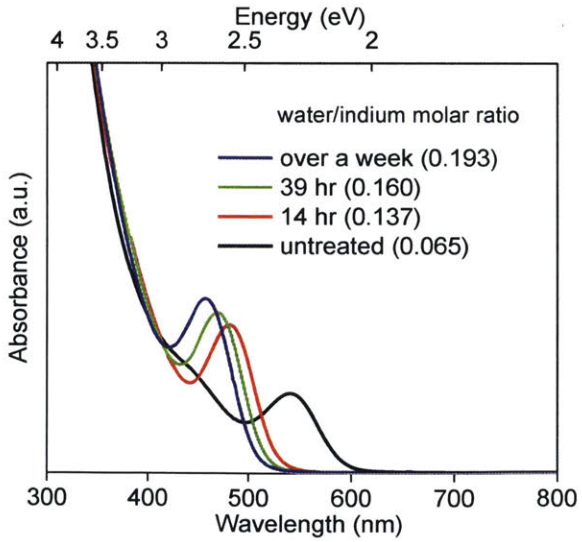

Figure D 1: Absorption spectra of InP QDs using $In(My)_3$ solutions (batch S1) treated with molecular sieves for different times. The 2-stage chip reactor system was used in this study.

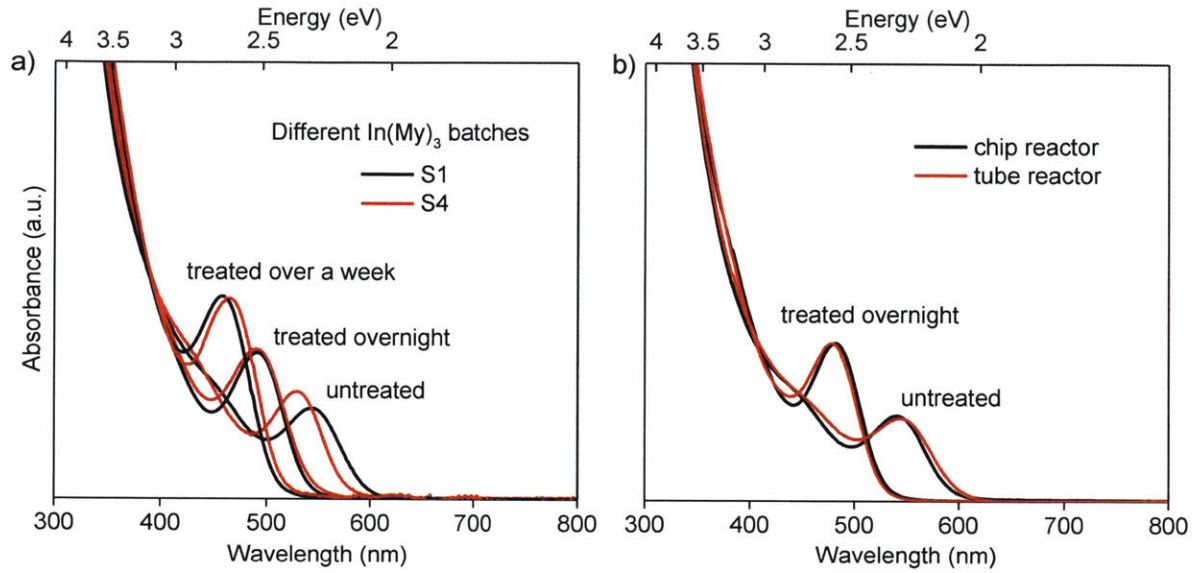

Figure D 2: Absorption spectra of InP QDs using: a) different batches of $In(My)_3$ solutions treated with molecular sieves for different times in the chip reactor system; b) two and chip reactor systems with $In(My)_3$ from batch S1.

Characterization of Precursors and QDs

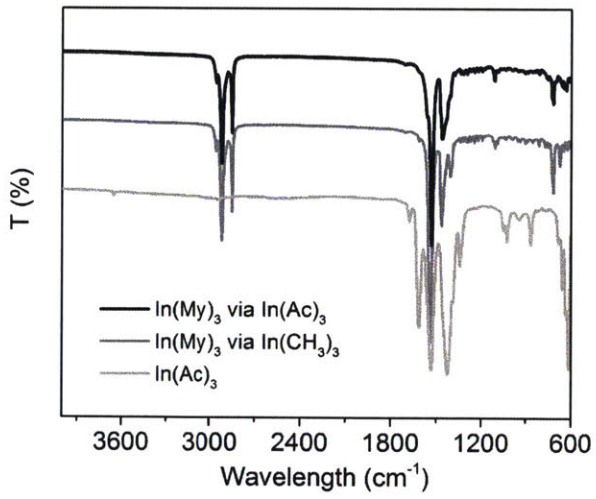

Figure D 3: FT-IR characterization of $In(Ac)_3$ derived $In(My)_3$, $In(CH_3)_3$ derived $In(My)_3$ and $In(Ac)_3$. Spectra are offset for clarity.

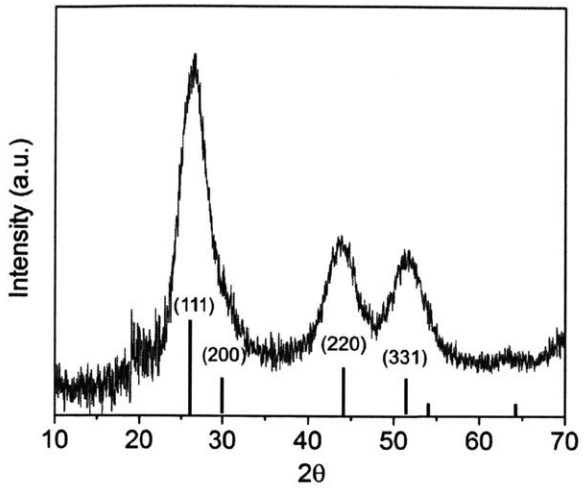

Figure D 4: Capillary XRD measurement of InP QDs with absorption peak at 547 nm. For the XRD measurement, InP QDs were purified and dissolved in octane. Both the sample solution and the solvent signals were collected. The final data was processed in a HighScore Plus software and the reference in the XRD spectra is from source: ICDD 00-032-0452.

Effect of Ligands

Experimental details related to the chemical for the syntheses of cluster-free QDs, and the reactors in use can be found in Appendix C.

HT/HP synthesis of cluster-free InP QDs. The synthesis of cluster-free InP QDs was performed in the 355 μL tube reactor system at 270 °C and 8.1 min. The concentration of indium and phosphorus precursor is set as 40 mM and 20 mM in toluene respectively. Their flow rates are set as the same (15 μL/min). 1-4 vol% TOP or equivalent molar amount of TOPO were added into the $In(My)_3$ solution to tune the absorption spectra. All precursor-handling processes

were carried out in a glove box. Here are the details of the experimental conditions we have used:

Table D 4: Experimental details to synthesize cluster-free InP QDs

First absorption peak (nm)	Surfactant Addition
520.5	4 equiv. % TOPO
531.0	2 equiv. % TOPO
546.5	1 vol% TOP + 1 equiv. % TOPO
570.5	4 vol% TOP
579.5	4 vol% TOP

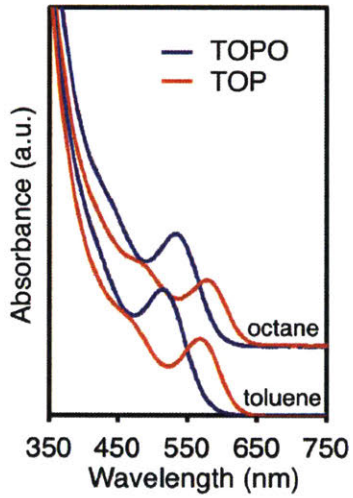

Figure D 5: Effect of TOP and TOPO in adjusting the QD sizes in different solvents. The 355 μL tube reactor is used for the syntheses. The flow rate of indium and phosphorus precursor is set as 20 μL/min. The temperature is set as 270 °C. 4 vol% TOP is added into the indium precursor. An equivalent amount of TOPO is used as comparison.

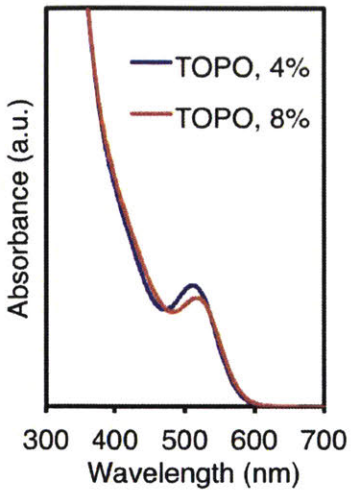

Figure D 6: Effect of TOPO in adjusting QD sizes. The flow rate of In and P precursor is set as 15 μL/min. The temperature is set as 270 °C for the 355 μL tube reactor. In a typical synthesis, 4 vol% TOP is added to the indium precursor solution. Here, the same molar amount of TOPO (labeled as 4%) and its doubled amount (labeled as 8%) are added to indium precursor solutions.

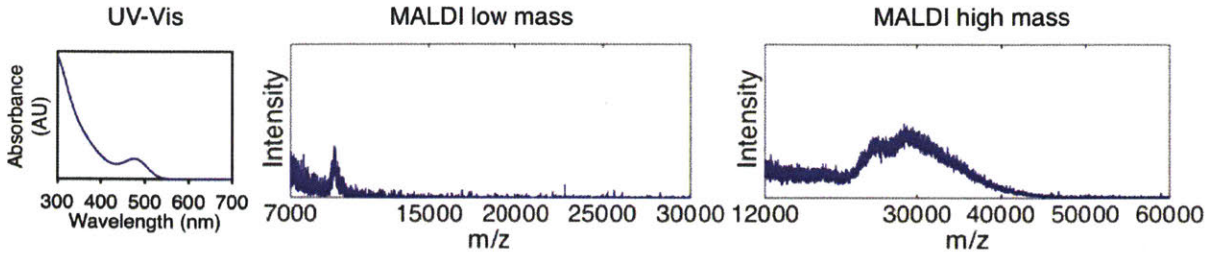

Figure D 7: UV-Vis and MALDI characterization of InP QDs synthesized with the addition of 5 mg base into the 5 mL indium precursor containing 4 vol% TOP in toluene.

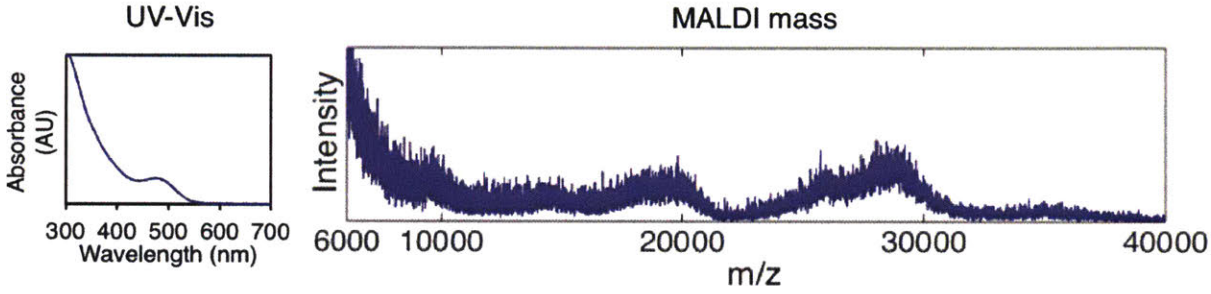

Figure D 8: UV-Vis and MALDI characterization of InP QDs synthesized with the addition of 15 μL amine into the 5 mL indium precursor containing 4 vol% TOP in toluene.

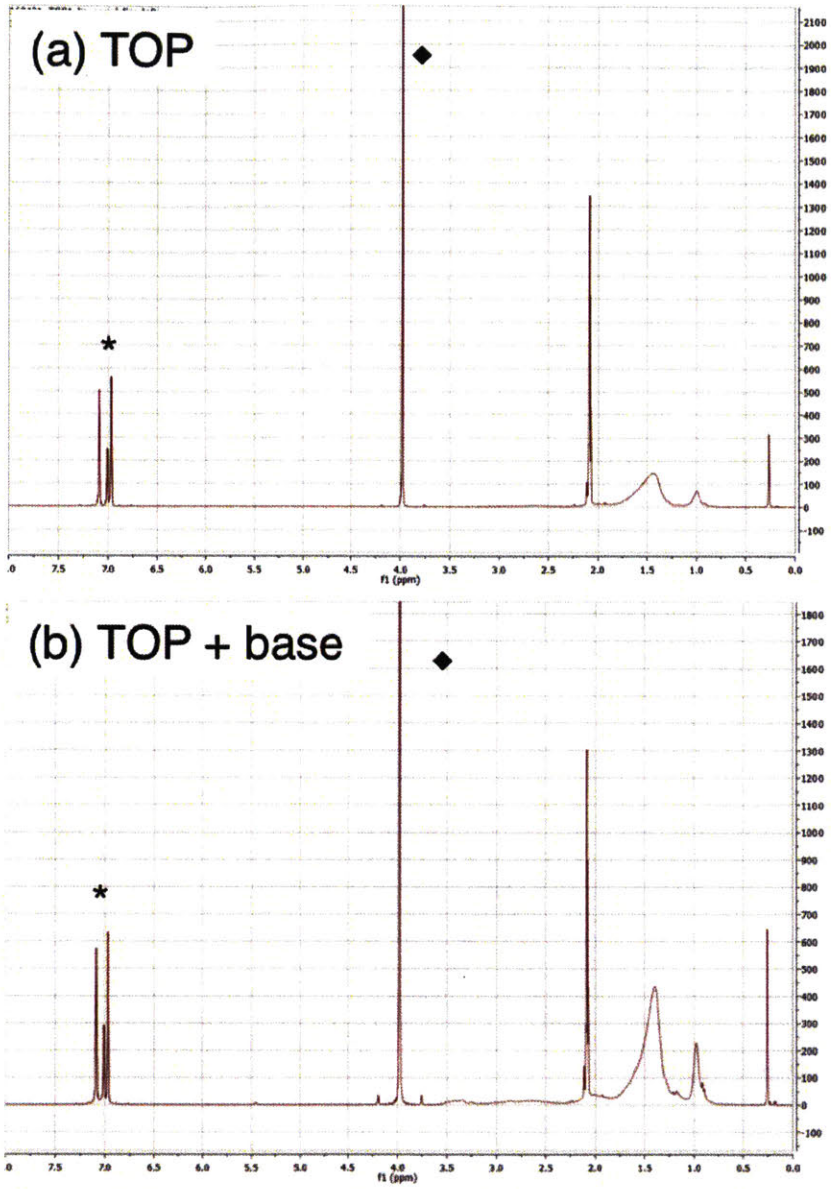

Figure D 9: ^{1}H NMR comparison of QDs synthesized with TOP and TOP-base mixtures. * is the signal of solvent and ◆ indicates the signal of internal standard. The broad peaks between 2.5 and 3.5 ppm were attributed to the OH groups bonded to the nanocrystal surfaces.

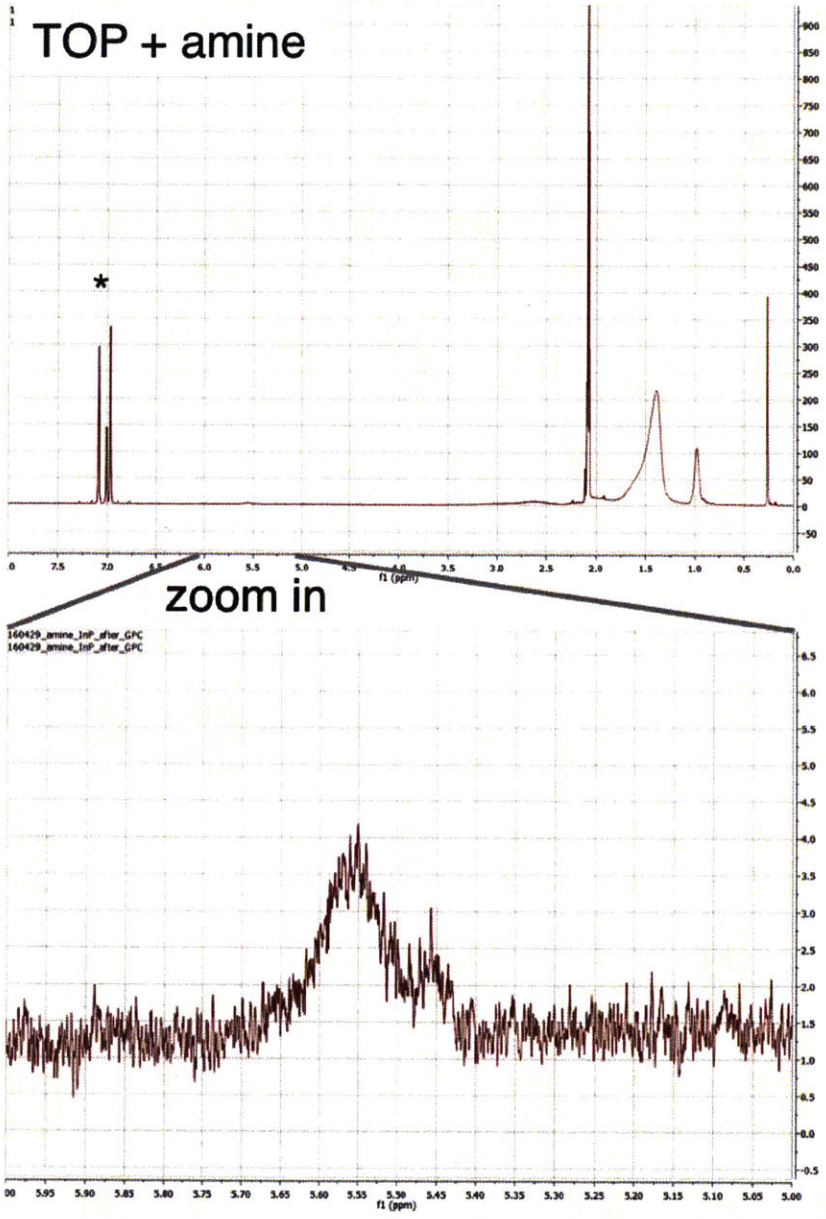

Figure D 10: ^{1}H NMR comparison of QDs synthesized with TOP and TOP-amine mixtures. * is the signal of solvent. The broad peak between 5 and 6 ppm were attributed to hydrogen atoms from C=C bonds which only exist in amines in the reagents used for the QD syntheses. Therefore, we speculate that some of the amines have bonded to the nanocrystal surfaces.

Quantification of extinction coefficients, inorganic core mass and the number of InP units per particle in the core

(1) The extinction coefficient at 310 nm (ε) is calculated according to the following formula:

$$\varepsilon = \frac{\lambda}{(m_1 - m_2)/m_M / V}$$

Where λ is the measured absolute absorbance at 350 nm of the QD solution, m_1 is the total dried mass of the above QD solution together with the measurement bottle, m_2 is the mass of the bottle, m_M is the average mass of the QDs measured through MALDI-TOF MS, V is the volume of the QD solution. To calculate the propagation error of the extinction coefficient calculation, the following formula is used:

$$\Delta\varepsilon = \sqrt{(\frac{\partial\varepsilon}{\partial\lambda})^2\Delta\lambda^2 + (\frac{\partial\varepsilon}{\partial m_1})^2\Delta m_1^2 + (\frac{\partial\varepsilon}{\partial m_2})^2\Delta m_2^2 + (\frac{\partial\varepsilon}{\partial m_M})^2\Delta m_M^2}$$

$\Delta\lambda$, Δm_1 and Δm_2 are the standard deviation calculated from multiple measurements.

For the MALDI mass, Δm_M is determined through

$$\Delta m_M = \sqrt{(m_{M,L} - \overline{m_M})^2 + (m_{M,H} - \overline{m_M})^2}$$

Where $m_{M,L}$ is the average mass obtained for the QD ensemble at the lowest laser power possible and $m_{M,H}$ is the average mass obtained for the QD ensemble at the lowest laser power plus 5% more laser power.

(2) After the GPC purification, since we only observed bound myristate signal from ^{1}H NMR spectra and no signal from the ^{31}P NMR spectra, the structure of the InP QDs can be written as $In_xP_y(My)_z$. The In_xP_y part was considered as the inorganic core, which should be observed in the

STEM-HAADF images. Myristate is considered as the only ligand on the QD surface, which is also attributed as the only proton source on the nanoparticle.

The ligand population on the particle was calculated based on ^{1}H NMR (with ferrocene as the internal standard) and the extinction coefficient described above. The total concentration of ligands was determined by the ^{1}H NMR peak integrals; the QD concentration is measured by UV-Vis absorption spectra and the calculated extinction coefficient. By dividing these two numbers, the ligand/QD ratio in each sample can be obtained.

The volume of the inorganic core ($V_{\text{inorganic}}$) is determined through the following formula:

$$V_{\text{inorganic}} = \frac{m_{\text{M}} - N_{\text{L}} \times M_{[\text{MA}]}}{\rho_{\text{InP}}}$$

Where N_{L} is the ligand population on the nanoparticle, ρ_{InP} is the density of InP bulk crystals and $M_{[\text{MA}]}$ is the molecular weight of myristate. Different estimated projected areas corresponding to this inorganic core volume can be obtained depending the shape of the nanoparticle.

If assuming spherical shape, $S_{\text{spherical}} = \pi r^2 = \pi(\frac{3}{4\pi} V_{\text{inorganic}})^{2/3}$

If assuming tetrahedron shape, $S_{\text{tetrahedron}} = \frac{\sqrt{3}}{4} a^2 = \frac{\sqrt{3}}{4}(6\sqrt{2} V_{\text{inorganic}})^{2/3}$

In this work, these two projected areas are used to compare against that obtained from STEM analysis.

(3) The number of InP units ($N_{[\text{InP}]}$) in a particle is determined through the following formula:

$$N_{[\text{InP}]} = \frac{m_{\text{M}} - N_{\text{L}} \times M_{[\text{MA}]} - N_{\text{L}} / 3 \times M_{[\text{In}]}}{M_{[\text{InP}]}}$$

Where $M_{[In]}$ is the molecular weight of an indium atom. To balance the charge of all the myristate ligand, the QDs should have an indium rich surface. By subtracting out those extra indium atoms, a neutral inorganic core made out of InP units could be obtained. Regarding the error propagation, using a similar method as described above, $\Delta N_{[InP]}$ can be quantified using Δm_M and ΔN_L. A 5% error is estimated for the ligand population quantification process, giving $\Delta N_L = 0.05 N_L \sqrt{2}$.

(4) The extinction coefficients per InP unit (ε') for a particle is determined through the following formula:

$$\varepsilon' = \frac{\varepsilon}{N_{[InP]}}$$

Regarding the error propagation, using a similar method as described above, $\Delta\varepsilon'$ can be quantified using $\Delta\lambda$, Δm_1 , Δm_2 , Δm_M and ΔN_L .

Table D 5: Ligand population, inorganic core mass and projected areas assuming different shapes of InP QDs with different first absorption peaks

First absorption peak (nm)	Particle mass (kDa)	Ligand population	Inorganic core mass (kDa)	Projected area (spherical shape,nm^2)	Projected area (tetrahedron shape,nm^2)	In/P ratio	Extinction coefficients at 350 nm ($M^{-1}cm^{-1}$)
520.5	46.5	111	21.3	4.6	6.8	1.32	2.2×10^5
531.0	55.0	130	25.5	5.2	7.7	1.31	3.1×10^5
546.5	70.5	157	34.8	6.3	9.4	1.27	3.8×10^5
570.5	89.0	185	47.0	7.7	11.5	1.22	5.8×10^5
579.5	99.0	201	53.3	8.4	12.6	1.21	8.7×10^5

To compare the QD optical property with the bulk InP property, we first calculated the average extinction coefficient per InP unit at 310 nm from our five QD samples, which is 5135 $M^{-1}cm^{-1}$. As a result, the absorption cross section can be calculated according to ref. 21, using

$$C_{abs,QD} = \frac{2303\varepsilon_{310}}{N_A}$$

We obtained the absorption cross section ($C_{abs,QD}$) as **1.96×10^{-17} cm^2**.

According to Aspnes and Studna's work[166], the absorption coefficient of the bulk InP at 310nm is 7.0×10^5 cm^{-1}. We obtained the absorption cross section of bulk InP material using the following formula:

$$C_{abs,bulk} = \frac{\alpha_{310}}{N}$$

Where the atomic number density is N = 3.96×10^{22}cm^3. Therefore, the absorption cross section of bulk InP material ($C_{abs,bulk}$) is equal to **1.77×10^{-17}cm^2**. As a result, our InP QD optical property at 310 nm and bulk InP property are very similar (**10%** absorption cross section difference).

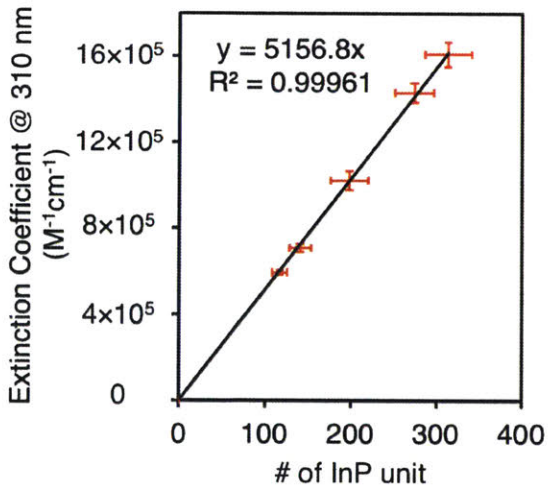

Figure D 11: Relation between InP units per particle and their extinction coefficients with error bars calculated using methods described above.

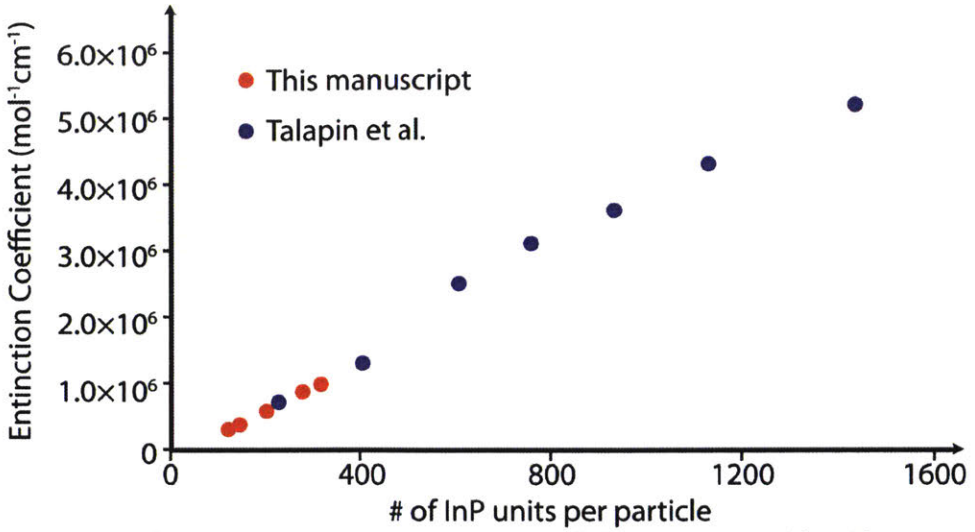

Figure D 12: Comparison between the extinction coefficients measured in this manuscript and the ones from Talapin et al[23]. The number of InP units per particle in Talapin's work was calculated by assuming that: (1) the particles are spherical in shape; (2) the In-to-P-ratio equals to 1 (the QDs are passivated by neutral ligands such as TOP and TOPO); (3) the density of the particles is the same as the bulk materials.

Effect of Solvents

Electrospray ionization mass spectrometry. The water contaminated $In(My)_3$ was characterized using Electrospray Ionization (ESI) mass spectrometry in both positive and negative ionization modes. The mass spec data were collected on Bruker APEXIV 4.7t FT-ICR-MS (Fourier-Transform Ion Cyclotron Resonance Mass Spectrometer) equipped with Bruker APOLLO ESI source. The characterization mixture consisted of 1:1 molar ratio $In(My)_3$: TOPO (15 mM) dissolved in dichloromethane and ethanol (30 vol%). TOPO was used to dissolve $In(My)_3$ in dichloromethane due to its higher purity than TOP in order to obtain a cleaner spectrum (The concentration of our sample was much higher than standard ESI samples in order

to obtain a strong signal. Before and after the characterization, the instrument should be cleaned with acetonitrile for more than ~5 times to prevent clogging). To minimize contamination from oxygen or moisture in the atmosphere, sample preparation was conducted in a glove box or in an inert atmosphere. The sample was treated as air-sensitive and the measurement was conducted in the MIT-Department of Chemistry Instrument Facility (DCIF). The large molecular sizes suggest that that $In(My)_3$ may participate in polynuclear[50] complexes with TOPO. The presence of TOPO is consistent with the need for TOPO to dissolve $In(My)_3$ into dichloromethane and similar phenomena have been observed for cadmium carboxylate precursors[167].

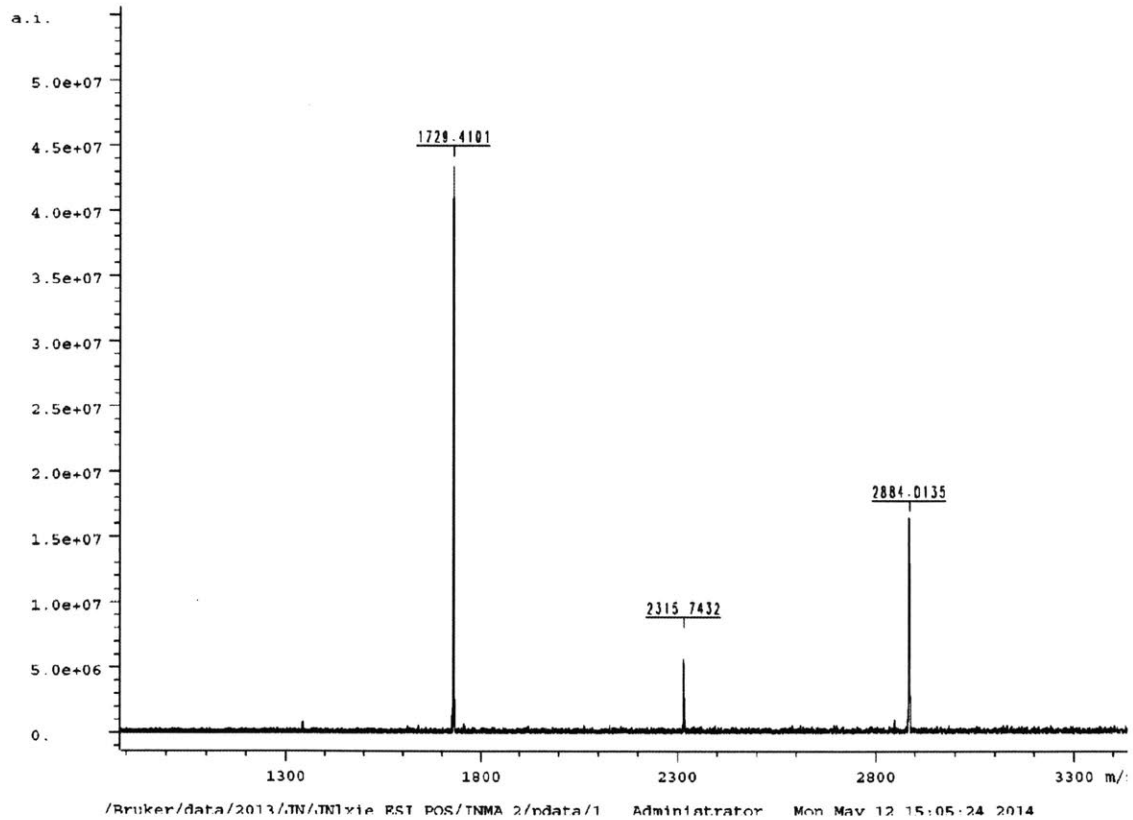

Figure D 13: Positive ESI mass spectrometry data of the $In(My)_3$ precursors which was co-dissolved with trioctylphoshine oxide in dichloromethane with 30 vol% ethanol.

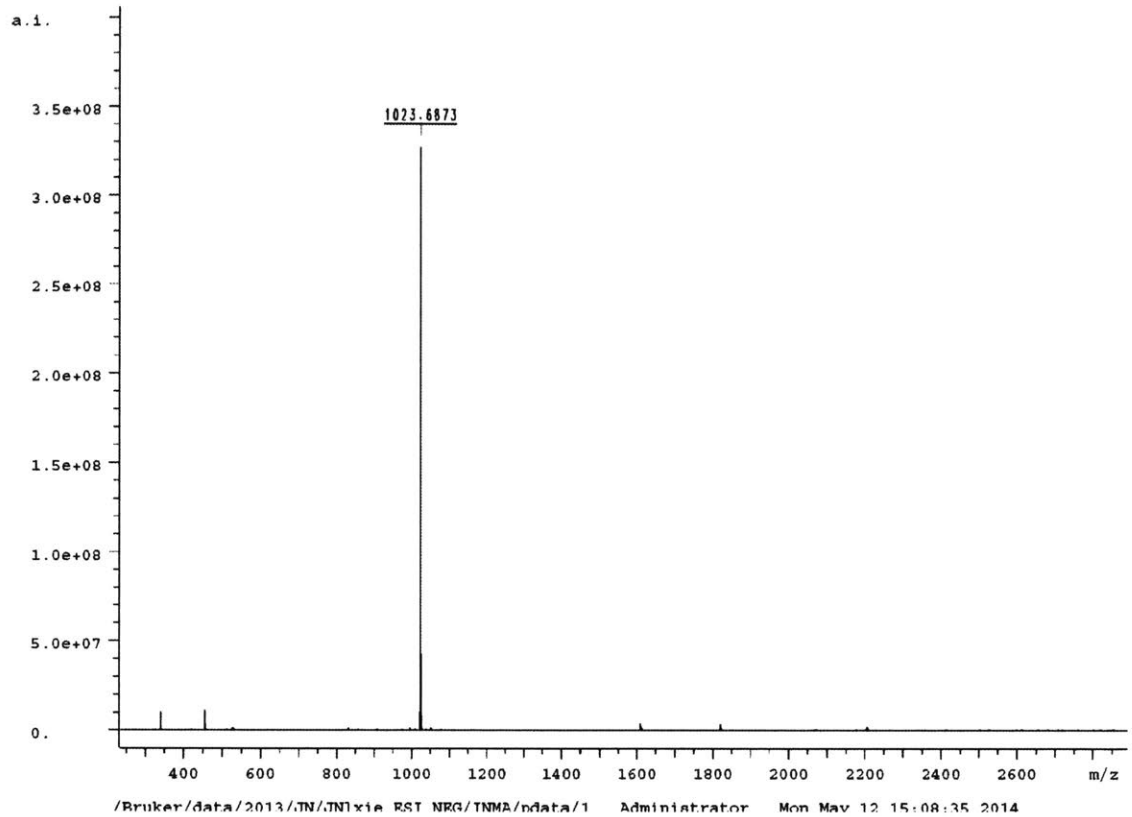

Figure D 14: Negative ESI mass spectrometry data of the $In(My)_3$ precursor which was co-dissolved with trioctylphoshine oxide in dichloromethane with 30 vol% ethanol.

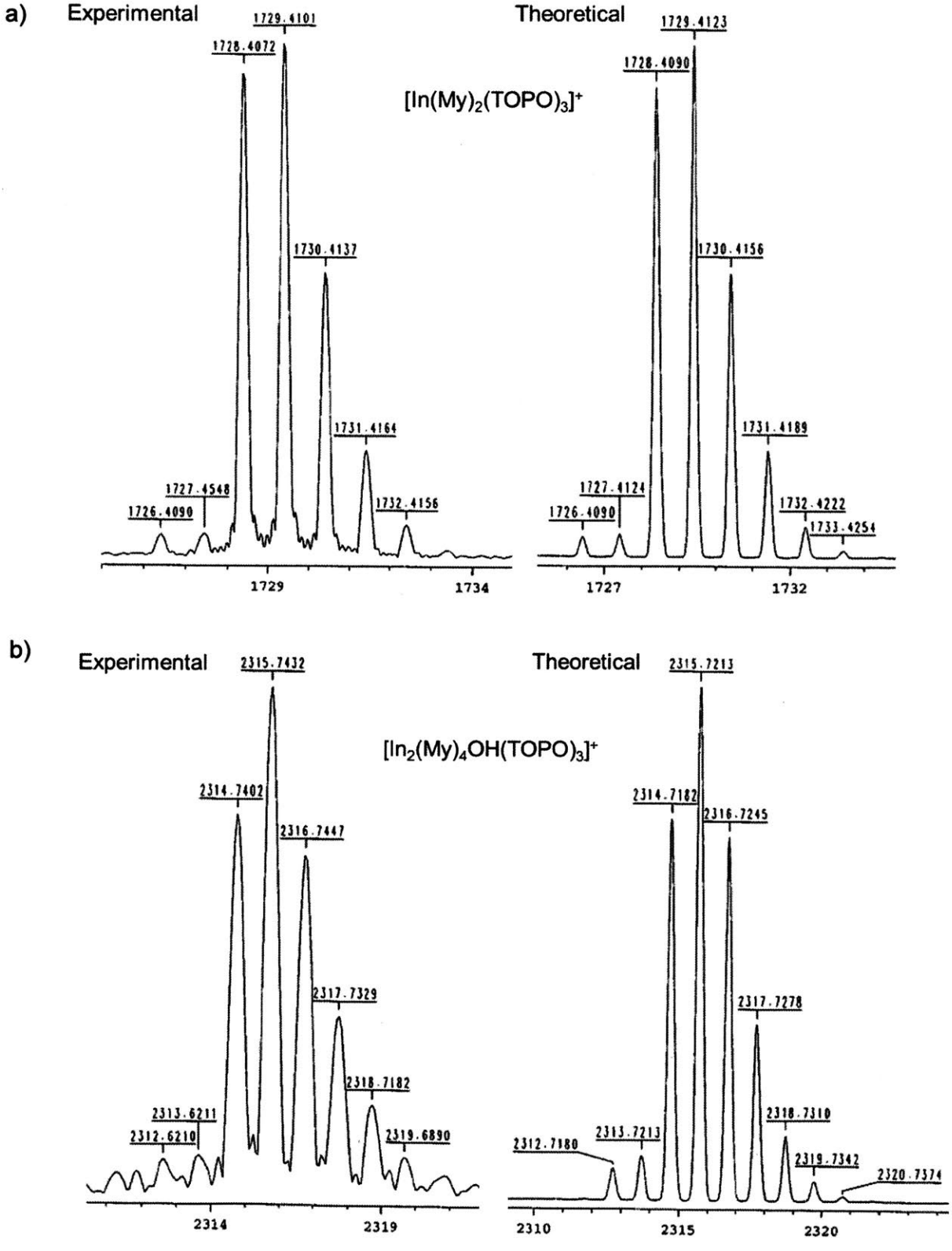
a)
Experimental
Theoretical
[In(My)2(TOPO)3]+
1729.4101
1728.4072
1730.4137
1731.4164
1727.4548
1726.4090
1732.4156
1729.4123
1728.4090
1730.4156
1731.4189
1727.4124
1726.4090
1732.4222
1733.4254
1729
1734
1727
1732
b)
Experimental
Theoretical
[In2(My)4OH(TOPO)3]+
2315.7432
2314.7402
2316.7447
2317.7329
2318.7182
2313.6211
2312.6210
2319.6890
2315.7213
2314.7182
2316.7245
2317.7278
2318.7310
2312.7180
2313.7213
2319.7342
2320.7374
2314
2319
2310
2315
2320

c)

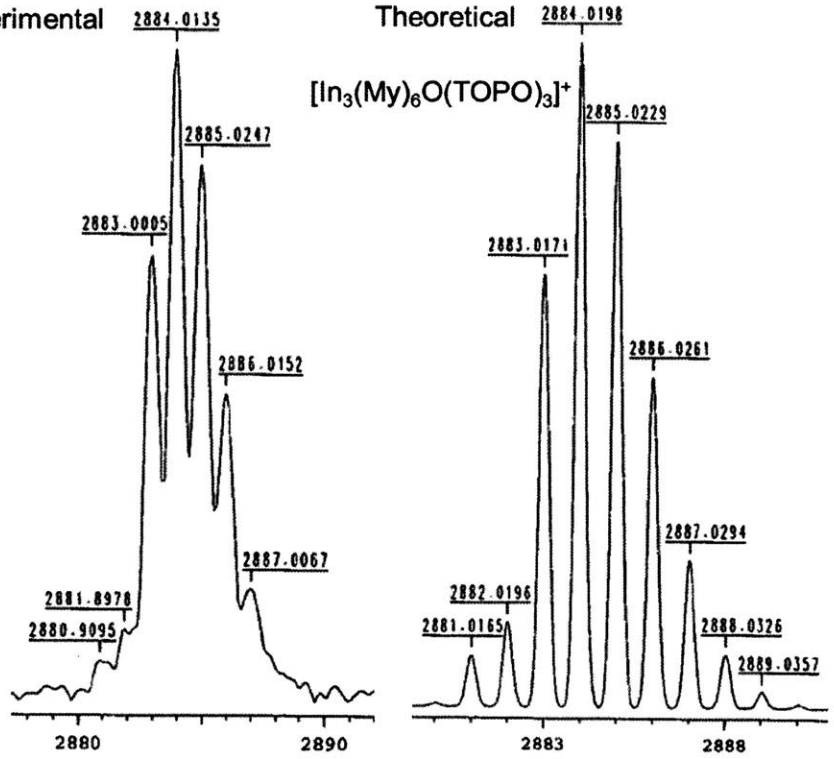
Experimental
2884.0135
2885.0247
2883.0005
2886.0152
2887.0067
2881.8978
2880.9095
2880
2890
Theoretical
2884.0198
[In3(My)6O(TOPO)3]+
2885.0229
2883.0171
2886.0261
2887.0294
2882.0196
2881.0165
2888.0326
2889.0357
2883
2888

d)

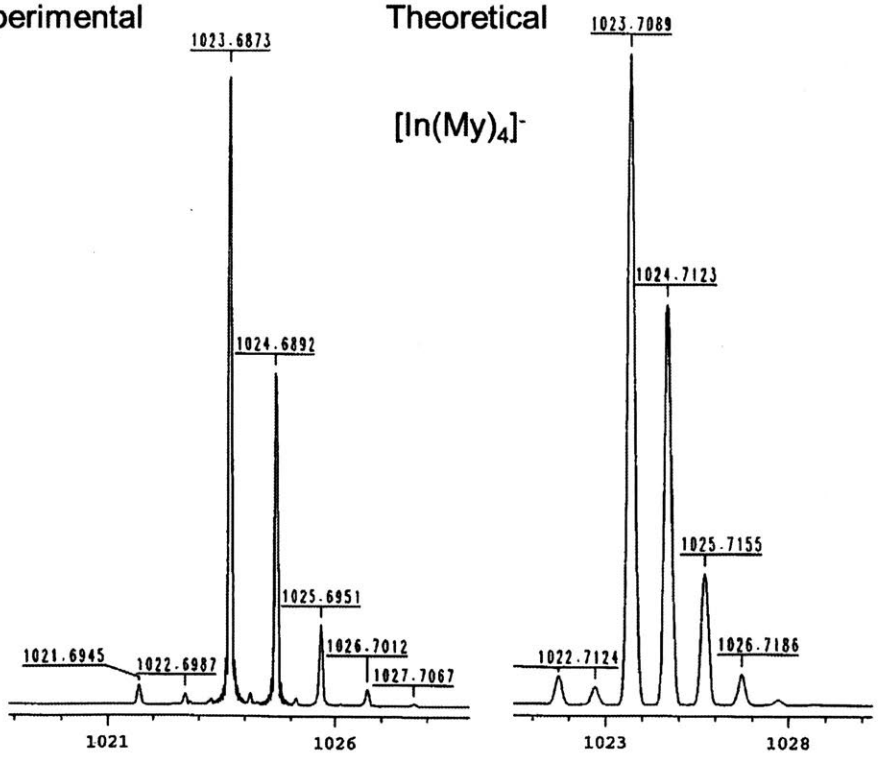
Experimental
1023.6873
1024.6892
1025.6951
1026.7012
1021.6945
1022.6987
1027.7067
1021
1026
Theoretical
1023.7089
[In(My)4]-
1024.7123
1025.7155
1022.7124
1026.7186
1023
1028

Figure D 15: Representative peaks from the ESI mass spectrum of the water contaminated $In(My)_3$ precursor which was co-dissolved with trioctylphoshine oxide in dichloromethane with 30 vol% ethanol.

Table D 6: Physical properties and measured water contents of solvents

Properties	octane	heptane	toluene	*o*-xylene
Boiling temp. (°C)	125-126	121	111	139
Density (g/ml)	0.70	0.72	0.87	0.86
Viscosity (cP @ 20 °C)	0.54	0.47	0.59	0.81
Dielectric constant (20 °C)	2.0	2.1	2.4	2.6
Polarity index (Burdick & Jackson)	0.1	0.1	2.4	2.5
Water content (ppm)	7.3	2.1	4.1	3.9

* The water content of 40 mM $In(My)_3$ dissolved in octane is measured as 68.3 ppm.

Appendix E

Oxygen-free Syntheses

This oxygen free protocol involves the use of indium halides such as indium chloride as the indium source and tris(dimethylamino)phosphine as the phosphorus source. Primary amines such as oleylamine are necessary solvents and ligands to promote the reaction. To improve the size distributions, a larger amount of zinc chloride is need. The addition of zinc source also results in the formation of small InP QDs. I first tried to reproduce the batch syntheses results from literature[37]. Through trial and error, it is found that the use of thick needles to inject phosphorus precursors into of the In-Zn-amine mixtures gives the best quality of QDs (Figure E 1).

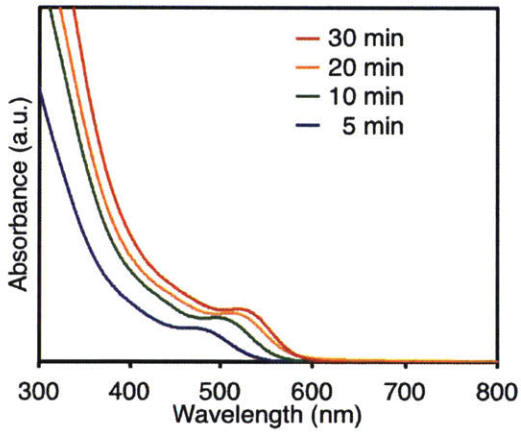

Figure E 1: An example batch synthesis of InP QDs using the oxygen-free protocol. 0.45 mL $P(NEt_2)_3$ (97%, Sigma Aldrich) was injected into the pre-degassed indium-zinc-oleylamine mixtures at 180 °C. The mixture consists of 100 mg $InCl_3$ (anhydrous, 99.99%, Alfra Aesar), 300 mg $ZnCl_2$ (anhydrous, 98+%, Alfra Aesar) and 5 mL oleylamine (technical grade, 70%, Sigma Aldrich).

I have also implemented the synthesis in flow, and produced InP QDs with comparable quality as those produced by batch methods (Figure E 2). Same In, Zn and P ratios are chosen as the batch synthesis. Indium and zinc sources are preheated to 50 °C to allow their dissolution in oleylamine for the flow operation. The phosphorus precursors are dissolved in 1-ODE in a 1:1 volume ratio to prevent corrosion towards the syringe O-rings. A relatively large flow rate, i.e. 125 μL/min for In-Zn-oleylamine mixture and 25 μL/min for P-ODE mixture are used to enhance the mixing. Stainless steel tubes with inner diameter as 500 um and stainless mixing tee with inner diameter as 250 um are chosen to enhance the mixing as well. The tube reactor volume is 2.8 mL. As the synthesis also generates low-boiling-point side products (likely to be Et_2NH), to avoid gas formation, a 500 psi pressure is applied at the downstream of the reactor. It is found that primary amines such as oleylamine, octylamine and hexylamine can all be used as solvents and ligands.

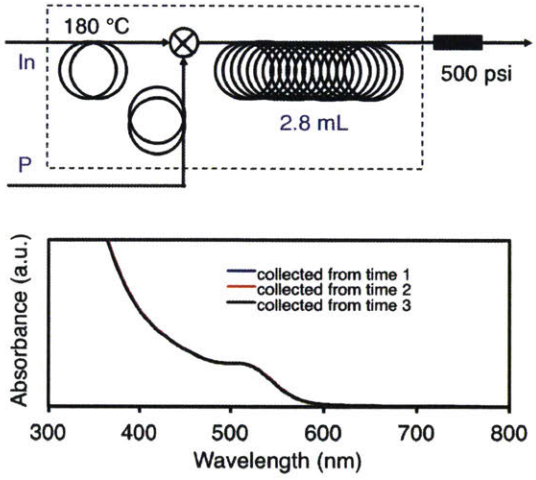

Figure E 2: Flow synthesis of InP QDs using the oxygen-free protocol. The system is under steady state operation indicated by the unchanged spectra collected as different growth times.

Appendix F

Ultra high temperature syntheses of InP QDs

Given that flow reactors could provide larger parameter space as compared to batch flasks, we explored the synthesis of InP QDs at extra high temperature (up to 430 °C) with the goal of making large InP nanoparticles. The hypothesis is that if we could provide higher energy to the system, the barrier for particles to grow via coalescence or ripening may be easier to overcome. Both absorption spectra and TEM images have shown the increase of the particle size with the increase of temperature (Figure F 1); however, as compared to the large particles obtained using excess acids (abs ~ 650 nm, D ~ 4.3 nm), the nanoparticle size is much bigger (abs ~ 600 nm, D > 5nm). XRD results showed no difference in the peak line width for different sizes of nanoparticles, indicating that although the size of nanoparticles has increased, the crystal structure was not well-annealed (Figure F 2). Clearly, the high temperature operation enhances the aggregation of the nanoparticles, but the particles are not well crystallized possibly due to the surface oxides on the nanoparticle surface.

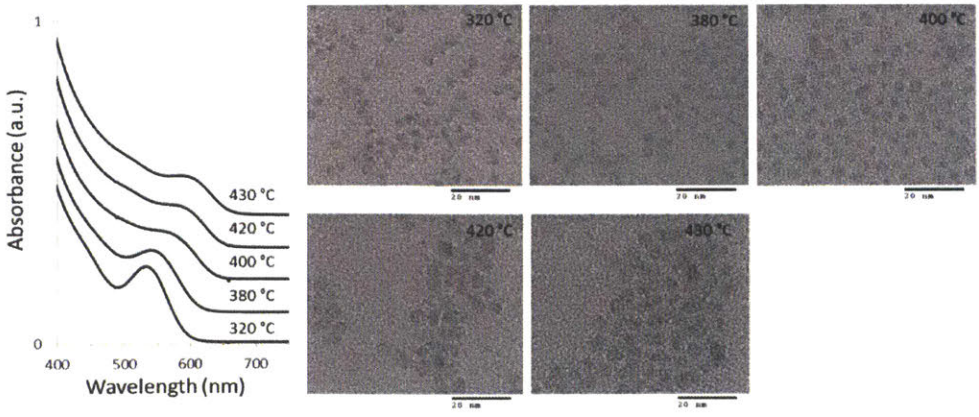

Figure F 1: Absorption spectra and TEM images of InP QDs synthesized at extra high temperature. The temperature of the first stage was fixed at 130 °C and the temperature of the second stage was varied. A 2-stage stainless steel tube reactor was used for this study.

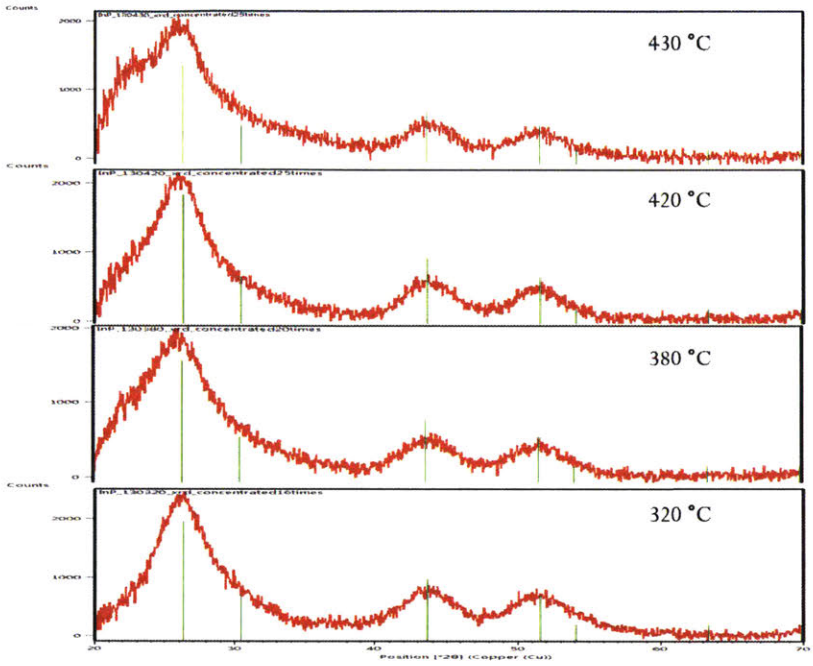

Figure F 2: Capillary XRD of InP QDs obtained with a two-stage tube reactor. The temperature of the first stage was fixed at 130 °C and the temperature of the second stage was varied. A 2-stage stainless steel tube reactor was used for this study.

Appendix G

Implementation of Dimer Method

The dimer method is a Hessian-free local saddle-point search algorithm, and therefore is especially appropriate for transition state searches of large systems. I have implemented both the dimer method and the improved dimer method in MATLAB. Figure G 1 illustrates the general algorithm for these dimer methods. The translation and rotation directions and steps/angles are important design parameters. Generally, the rotation direction ($\boldsymbol{\Theta}$) should lead to a maximum overlap with the eigenvector corresponding to the lowest eigenvalue. The rotation angle (φ) should lead to a minimum curvature in the plane spanned by $\boldsymbol{N}$ and $\boldsymbol{\Theta}$. The translation direction ($\boldsymbol{N}^*$) should be the inverted force component along the dimer. And the translation step (d) should be predefined or self-adjusted during the search.

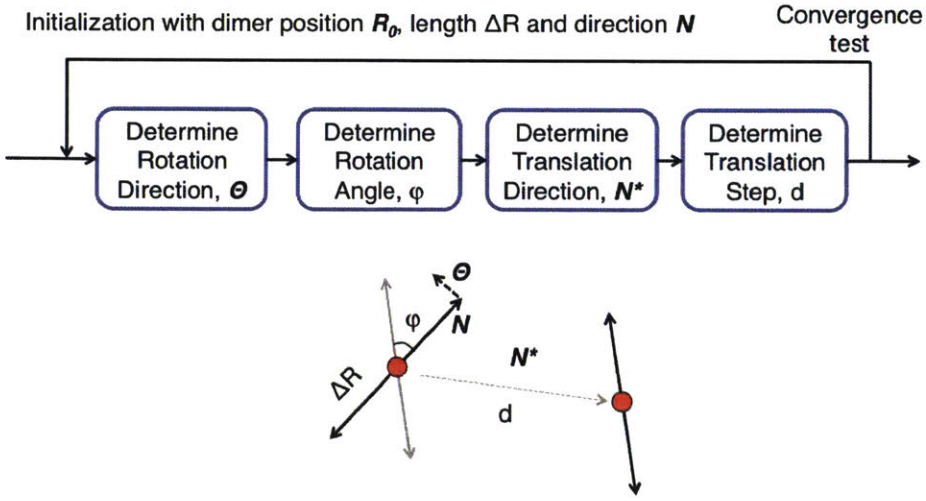

Figure G 1. The general algorithm of dimer methods.

The detailed algorithms of the dimer method and the improved dimer method I implemented are shown below:

a. Dimer method

The dimer position is first defined as

$$R_1 = R_0 + \Delta R\mathrm{N}$$
$$R_2 = R_0 - \Delta R\mathrm{N}$$

Where N is the unit vector along the dimer axis, R_0 is the dimer middle point, and ΔR is half of the dimer length. R_0, ΔR and N are initial parameters. To decide the rotation direction Θ (a unit vector), two methods are used: the steepest descent or conjugate gradient method. In the steepest descent method, the rotation plane is spanned by $F^{\perp}$ and N, and the rotation direction is within this plane and perpendicular to N. Here,

$$\Theta = \frac{F^{\perp}}{\left\|F^{\perp}\right\|}, \text{ where } F^{\perp} = F_1^{\perp} - F_2^{\perp} \text{ and } F_i^{\perp} = F_i - (F_i \cdot N)N, i = 1,2$$

In the conjugate gradient method, the first step is still performed using the steepest descent method. But for the subsequent iterations, the rotation direction is decided from the current force and the force at the previous iteration. For example, at the jth iteration,

$$\Theta_j = \frac{G_j^{\perp}}{\left\|G_j^{\perp}\right\|}, \text{ where } G_{j,j=1}^{\perp} = F_j^{\perp} \text{ and } G_{j,j\neq 1}^{\perp} = F_j^{\perp} + \gamma_j G_{j-1}^{\perp} \left(\gamma_j = \frac{(F_j^{\perp} - F_{j-1}^{\perp}) \cdot F_j^{\perp}}{F_j^{\perp} \cdot F_j^{\perp}}\right)$$

After determining the rotation direction, the rotation angle (φ) needs to be specified. I denote the preferable rotation angle as $\varphi_{\min}$ and here is the method to specify $\varphi_{\min}$.

$$\varphi_{\min} = -\frac{1}{2}\arctan\left(\frac{2f}{f'}\right) - \frac{\delta\varphi}{2} \quad (\delta\varphi \text{ is a small angle})$$

$$\text{Where, } f = \frac{[(F_1 - F_2)^T \cdot \Theta]_{\varphi=\delta\varphi} + [(F_1 - F_2)^T \cdot \Theta]_{\varphi=0}}{2} \text{ and } f' = \frac{[(F_1 - F_2)^T \cdot \Theta]_{\varphi=\delta\varphi} - [(F_1 - F_2)^T \cdot \Theta]_{\varphi=0}}{2}$$

With Θ and $\varphi_{\min}$, the new dimer position after rotation can be obtained.

$$R_{1/2}(\varphi_{\min}) = R_0 \pm \Delta R(N\cos\varphi_{\min} + \Theta\sin\varphi_{\min})$$

After the rotation step, the dimer midpoint needs to be translated along a modified force $f^{\dagger}$, where the force component along the dimer axis is inverted. Depending on whether the curvature along the dimer axis is positive or negative, the modified forces have different formula. Similarly, both steepest descent method and the conjugate gradient method can be used to determine this modified force and thus the translation direction (a unit vector, N^*). In the steepest descent method,

$$f^{\dagger} = -(F_0^T \cdot N)\cdot N \text{, if } C_N > 0$$

$$f^{\dagger} = F_0 - 2(F_0^T \cdot N)\cdot N \text{, if } C_N < 0$$

Where, F_0 is the force at the dimer middle point which can be evaluated independently, or approximately by forces or energies at the two dimer end points; C_N is the local curvature and can be approximated using forces or energies

$$C_N \approx \frac{(F_2 - F_1)^T \cdot N}{2\Delta R} \approx \frac{E_1 + E_2 - 2E_0}{\Delta R^2}$$

The translation direction thus is

$$N^* = \frac{f^{\dagger}}{\left\|f^{\dagger}\right\|}$$

In the conjugated gradient method, the translation direction at the jth iteration can be decided as

$$N^* = \frac{g_j^{\dagger}}{\left\|g_j^{\dagger}\right\|}, \text{ where } g_{j,j=1}^{\dagger} = f_j^{\dagger} \text{ and } g_{j,j\neq 1}^{\dagger} = f_j^{\dagger} + \lambda_j g_{j-1}^{\dagger} \left(\lambda_j = \frac{(f_j^{\dagger} - f_{j-1}^{\dagger})\cdot f_j^{\dagger}}{f_j^{\dagger}\cdot f_j^{\dagger}}\right)$$

After determining the dimer translation direction, the translation step (d) also needs to be specified. We denote the preferable translation step length as $d_{\max}$ and it can be calculated as

$$d_{\max} = -\frac{(\mathrm{f}^{\dagger}|_{d=\delta d} + \mathrm{f}^{\dagger}|_{d=0})^{T} \cdot \mathrm{N}^{*} / 2}{(\mathrm{f}^{\dagger}|_{d=\delta d} - \mathrm{f}^{\dagger}|_{d=0})^{T} \cdot \mathrm{N}^{*} / \delta d} + \frac{\delta d}{2} \quad (\delta d \text{ is a small length})$$

With N^{*} and $d_{\max}$, the new dimer position after translation can be obtained.

$$\mathrm{R}_{1/2,new} = \mathrm{R}_{1/2} + d_{\max}\mathrm{N}^{*}$$

To check the convergence of the method, the local curvature can be evaluated to decide whether it is a saddle point.

b. Improved Dimer method

The major modification in the improved dimer method compared to the original dimer method is summarized below:

(1) Rotation angle

$$\varphi = \frac{\pi}{4} \text{ or } \varphi = \frac{1}{2}\arctan(\frac{b_1}{a_1})$$

Where, $a_1 = \dfrac{\dfrac{\partial C_x}{\partial \varphi}|_{\varphi=0}\cos(2\varphi_1) - \dfrac{\partial C_x}{\partial \varphi}|_{\varphi=\varphi_1}}{2\sin(2\varphi_1)}$, $b_1 = 0.5\dfrac{\partial C_x}{\partial \varphi}|_{\varphi=0}$ and $\varphi_1 = 0.5\arctan(\dfrac{-\partial C_x / \partial \varphi|_{\varphi=0}}{2C_x|_{\varphi=0}})$.

C_x is the local curvature and can be approximated as

$$C_x = \frac{a_0}{2} + a_1\cos(2\varphi) + b_1\sin(2\varphi), \text{ where } a_0 = 2(C_x|_{\varphi=0} - a_1)$$

(2) Translation step

$$d = \frac{0.5(\mathrm{N}^{*,T}\mathrm{f}^{\dagger})}{|C_x|_{\varphi=0}|}$$

But when $d = \frac{0.5(\mathrm{N}^{*T}\mathrm{f}^{\dagger})}{|C_x|_{\varphi=0}|} < 0.01$, $d = 0.01$, or when $d = \frac{0.5(\mathrm{N}^{*T}\mathrm{f}^{\dagger})}{|C_x|_{\varphi=0}|} > 0.1$, $d = 0.1$

I tested the improved dimer method for TS search on Muller, LEPS-I and LEPS-II surfaces. As these surfaces all contain two variables, the initial dimer orientation is chosen as (1, 0). The maximum iteration number is set as 2000. The steepest descent method is used for the search for both rotation direction and translation direction. I also tested the use of the conjugated gradient method and it does not improve the TS search efficiency. The TS search fails if the iteration number exceeds 2000 or the calculation converges to non-saddle point. The convergence is achieved if the dimer middle point does not move within 10^{-8}.

I performed a simple study on the effects of initial guesses on the TS search efficiency, as shown in Figure G 2. As expected, when the initial guess is close to the TS, the improve dimer method is efficient in finding the right TS. The choice of initial guess can heavily bias the final outcome.

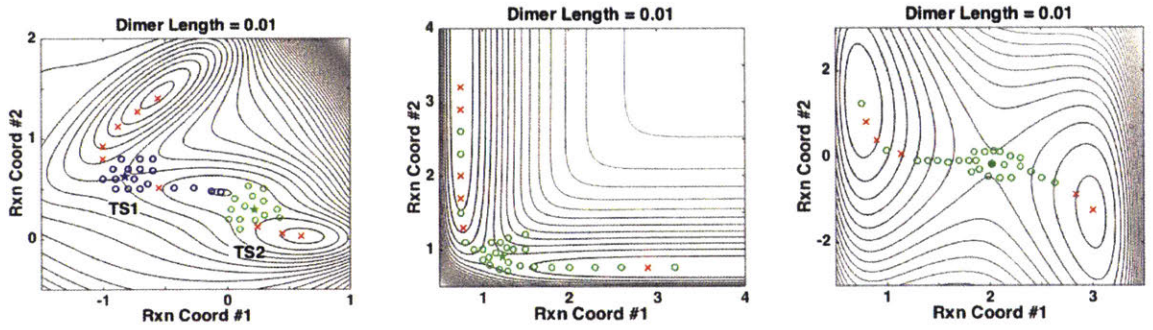

Figure G 2: TS search using (left) Muller surface, (middle) LEPS-I surface and (right) LEPS-II surface with the improved dimer method given the dimer length (dR) as 0.01. Blue/green open circles indicate that initial guesses starting at these points converged to the blue/green-star-shaped transition state respectively. Red crosses indicate failed TS search.

I also studied the change of dimer length on the TS search efficiency on these three surfaces (Table G 1-3). On all these surfaces, an optimal dimer length exists (0.005 for Muller, 0.01 for LEPS-I and LEPS-II) where the TS search is the most efficient.

Table G 1: Effect of dimer length on the Muller surface (41 initial guesses)

dR	TS1	TS2	Not TS
0.5	6	3	32
0.3	17	8	16
0.1	18	13	10
0.05	17	14	10
0.01	18	14	9
0.005	20	14	7
0.001	19	14	8

Table G 2: Effect of dimer length on the LEPS-I surface (33 initial guesses)

dR	TS	Not TS
0.5	17	16
0.3	25	8
0.1	24	9
0.05	25	8
0.01	27	6
0.005	24	9
0.001	22	11

Table G 3: Effect of dimer length on the LEPS-II surface (30 initial guesses)

dR	TS	Not TS
0.5	24	6
0.3	23	7
0.1	25	5
0.05	22	8
0.01	25	5
0.005	23	7
0.001	24	6

Reference

1. Alfassi, Z.; Bahnemann, D.; Henglein, A., Photochemistry of Colloidal Metal Sulfides. 3. Photoelectron Emission from Cadmium Sulfide and Cadmium Sulfide-Zinc Sulfide Cocolloids. *J. Phys. Chem.* **1982**, *86*, 4656-4657.
2. Rossetti, R.; Brus, L., Electron-Hole Recombination Emission as a Probe of Surface Chemistry in Aqueous Cadmium Sulfide Colloids. *J. Phys. Chem.* **1982**, *86*, 4470-4472.
3. Rossetti, R.; Nakahara, S.; Brus, L. E., Quantum Size Effects in the Redox Potentials, Resonance Raman Spectra, and Electronic Spectra of Cds Crystallites in Aqueous Solution. *J. Chem. Phys.* **1983**, *79*, 1086-1088.
4. Ekimov, A. I.; Efros, A. L.; Onushchenko, A. A., Quantum Size Effect in Semiconductor Microcrystals. *Solid State Commun.* **1985**, *56*, 921-924.
5. Xie, R.; Battaglia, D.; Peng, X., Colloidal Inp Nanocrystals as Efficient Emitters Covering Blue to near-Infrared. *J. Am. Chem. Soc.* **2007**, *129*, 15432-15433.
6. Guzelian, A. A.; Banin, U.; Kadavanich, A. V.; Peng, X.; Alivisatos, A. P., Colloidal Chemical Synthesis and Characterization of Inas Nanocrystal Quantum Dots. *Appl. Phys. Lett.* **1996**, *69*, 1432-1434.
7. Murray, C. B.; Norris, D. J.; Bawendi, M. G., Synthesis and Characterization of Nearly Monodisperse Cde (E = Sulfur, Selenium, Tellurium) Semiconductor Nanocrystallites. *J. Am. Chem. Soc.* **1993**, *115*, 8706-8715.
8. Jasieniak, J.; Califano, M.; Watkins, S. E., Size-Dependent Valence and Conduction Band-Edge Energies of Semiconductor Nanocrystals. *ACS Nano* **2011**, *5*, 5888-5902.
9. Weidman, M. C.; Beck, M. E.; Hoffman, R. S.; Prins, F.; Tisdale, W. A., Monodisperse, Air-Stable Pbs Nanocrystals Via Precursor Stoichiometry Control. *ACS Nano* **2014**, *8*, 6363-6371.
10. Hines, M. A. S., G.D., Colloidal Pbs Nanocrystals with Size-Tunable near-Infrared Emission: Observation of Post-Synthesis Self-Narrowing of the Particle Size Distribution. *Adv. Mater.* **2003**, *15*, 6.
11. Talapin, D. V.; Lee, J.-S.; Kovalenko, M. V.; Shevchenko, E. V., Prospects of Colloidal Nanocrystals for Electronic and Optoelectronic Applications. *Chem. Rev.* **2010**, *110*, 389-458.
12. Carey, G. H.; Abdelhady, A. L.; Ning, Z.; Thon, S. M.; Bakr, O. M.; Sargent, E. H., Colloidal Quantum Dot Solar Cells. *Chem. Rev.* **2015**, *115*, 12732-12763.
13. Medintz, I. L.; Uyeda, H. T.; Goldman, E. R.; Mattoussi, H., Quantum Dot Bioconjugates for Imaging, Labelling and Sensing. *Nat. Mater.* **2005**, *4*, 435-446.
14. Wood, V.; Bulović, V., Colloidal Quantum Dot Light-Emitting Devices. *Nano Rev.* **2010**, *1*, 5202.
15. Chen, O.; Wei, H.; Maurice, A.; Bawendi, M.; Reiss, P., Pure Colors from Core–Shell Quantum Dots. *MRS Bull.* **2013**, *38*, 696-702.
16. Allen, P. M.; Liu, W.; Chauhan, V. P.; Lee, J.; Ting, A. Y.; Fukumura, D.; Jain, R. K.; Bawendi, M. G., Inas(Zncds) Quantum Dots Optimized for Biological Imaging in the near-Infrared. *J. Am. Chem. Soc.* **2010**, *132*, 470-471.
17. Wells, R. L.; Pitt, C. G.; McPhail, A. T.; Purdy, A. P.; Shafieezad, S.; Hallock, R. B., The Use of Tris(Trimethylsilyl)Arsine to Prepare Gallium Arsenide and Indium Arsenide. *Chem. Mater.* **1989**, *1*, 4-6.

18. Wells, R. L.; Aubuchon, S. R.; Kher, S. S.; Lube, M. S.; White, P. S., Synthesis of Nanocrystalline Indium Arsenide and Indium Phosphide from Indium(Iii) Halides and Tris(Trimethylsilyl)Pnicogens. Synthesis, Characterization, and Decomposition Behavior of I3in.Cntdot.P(Sime3)3. *Chem. Mater.* **1995**, *7*, 793-800.
19. Olshavsky, M. A.; Goldstein, A. N.; Alivisatos, A. P., Organometallic Synthesis of Gallium-Arsenide Crystallites, Exhibiting Quantum Confinement. *J. Am. Chem. Soc.* **1990**, *112*, 9438-9439.
20. Micic, O. I.; Curtis, C. J.; Jones, K. M.; Sprague, J. R.; Nozik, A. J., Synthesis and Characterization of Inp Quantum Dots. *J. Phys. Chem.* **1994**, *98*, 4966-4969.
21. Guzelian, A. A.; Katari, J. E. B.; Kadavanich, A. V.; Banin, U.; Hamad, K.; Juban, E.; Alivisatos, A. P.; Wolters, R. H.; Arnold, C. C.; Heath, J. R., Synthesis of Size-Selected, Surface-Passivated Inp Nanocrystals. *J. Phys. Chem.* **1996**, *100*, 7212-7219.
22. Mićić, O. I.; Nozik, A. J., Spectroscopy of Isolated and Assembled Semiconductor Nanocrystalssynthesis and Characterization of Binary and Ternary Iii–V Quantum Dots. *J. Lumin.* **1996**, *70*, 95-107.
23. Talapin, D. V.; Gaponik, N.; Borchert, H.; Rogach, A. L.; Haase, M.; Weller, H., Etching of Colloidal Inp Nanocrystals with Fluorides: Photochemical Nature of the Process Resulting in High Photoluminescence Efficiency. *J. Phys. Chem. B* **2002**, *106*, 12659-12663.
24. Battaglia, D.; Peng, X., Formation of High Quality Inp and Inas Nanocrystals in a Noncoordinating Solvent. *Nano Lett.* **2002**, *2*, 1027-1030.
25. Xu, S.; Kumar, S.; Nann, T., Rapid Synthesis of High-Quality Inp Nanocrystals. *J. Am. Chem. Soc.* **2006**, *128*, 1054-1055.
26. Li, L.; Reiss, P., One-Pot Synthesis of Highly Luminescent Inp/Zns Nanocrystals without Precursor Injection. *J. Am. Chem. Soc.* **2008**, *130*, 11588-11589.
27. Xu, S.; Ziegler, J.; Nann, T., Rapid Synthesis of Highly Luminescent Inp and Inp/Zns Nanocrystals. *J. Mater. Chem.* **2008**, *18*, 2653-2656.
28. Lim, J.; Bae, W. K.; Lee, D.; Nam, M. K.; Jung, J.; Lee, C.; Char, K.; Lee, S., Inp@Znses, Core@Composition Gradient Shell Quantum Dots with Enhanced Stability. *Chem. Mater.* **2011**, *23*, 4459-4463.
29. Kim, S., et al., Highly Luminescent Inp/Gap/Zns Nanocrystals and Their Application to White Light-Emitting Diodes. *J. Am. Chem. Soc.* **2012**, *134*, 3804-3809.
30. Lim, J.; Park, M.; Bae, W. K.; Lee, D.; Lee, S.; Lee, C.; Char, K., Highly Efficient Cadmium-Free Quantum Dot Light-Emitting Diodes Enabled by the Direct Formation of Excitons within Inp@Znses Quantum Dots. *ACS Nano* **2013**, *7*, 9019-9026.
31. Cao, Y.-W. B., Uri, Synthesis and Characterization of Inas/Inp and Inas/Cdse Core/Shell Nanocrystals. *Anew. Chem. Int. Ed.* **1999**, *38*, 3.
32. Cao; Banin, U., Growth and Properties of Semiconductor Core/Shell Nanocrystals with Inas Cores. *J. Am. Chem. Soc.* **2000**, *122*, 9692-9702.
33. Kim, S.-W.; Zimmer, J. P.; Ohnishi, S.; Tracy, J. B.; Frangioni, J. V.; Bawendi, M. G., Engineering Inasxp1-X/Inp/Znse Iii–V Alloyed Core/Shell Quantum Dots for the near-Infrared. *J. Am. Chem. Soc.* **2005**, *127*, 10526-10532.
34. Xie, R.; Chen, K.; Chen, X.; Peng, X., Inas/Inp/Znse Core/Shell/Shell Quantum Dots as near-Infrared Emitters: Bright, Narrow-Band, Non-Cadmium Containing, and Biocompatible. *Nano Res.* **2008**, *1*, 457-464.

35. Liu, W.; Lee, J.-S.; Talapin, D. V., Iii–V Nanocrystals Capped with Molecular Metal Chalcogenide Ligands: High Electron Mobility and Ambipolar Photoresponse. *J. Am. Chem. Soc.* **2013**, *135*, 1349-1357.
36. Song, W.-S.; Lee, H.-S.; Lee, J. C.; Jang, D. S.; Choi, Y.; Choi, M.; Yang, H., Amine-Derived Synthetic Approach to Color-Tunable Inp/Zns Quantum Dots with High Fluorescent Qualities. *J. Nanopart. Res.* **2013**, *15*, 1-10.
37. Tessier, M. D.; Dupont, D.; De Nolf, K.; De Roo, J.; Hens, Z., Economic and Size-Tunable Synthesis of Inp/Zne (E = S, Se) Colloidal Quantum Dots. *Chem. Mater.* **2015**, *27*, 4893-4898.
38. Kim, K. Y., Dongsuk; Choi, Hyekyoung; Tamang, Sudaran; Ko, Jae-Hyeon; Kim, Sungwoo; Kum, Yong-Hyun; Jeong, Sohee, Halide–Amine Co-Passivated Indium Phosphide Colloidal Quantum Dots in Tetrahedral Shape. *Angew. Chem. Int. Ed.* **2016**, *55*, 5.
39. Tessier, M. D.; De Nolf, K.; Dupont, D.; Sinnaeve, D.; De Roo, J.; Hens, Z., Aminophosphines: A Double Role in the Synthesis of Colloidal Indium Phosphide Quantum Dots. *J. Am. Chem. Soc.* **2016**, *138*, 5923-5929.
40. Das, A.; Shamirian, A.; Snee, P. T., Arsenic Silylamide: An Effective Precursor for Arsenide Semiconductor Nanocrystal Synthesis. *Chem. Mater.* **2016**, *28*, 4058-4064.
41. Harris, D. K.; Bawendi, M. G., Improved Precursor Chemistry for the Synthesis of Iii–V Quantum Dots. *J. Am. Chem. Soc.* **2012**, *134*, 20211-20213.
42. Chen, O., et al., Compact High-Quality Cdse–Cds Core–Shell Nanocrystals with Narrow Emission Linewidths and suppressed Blinking. *Nat. Mater.* **2013**, *12*, 445-451.
43. Cui, J.; Beyler, A. P.; Marshall, L. F.; Chen, O.; Harris, D. K.; Wanger, D. D.; Brokmann, X.; Bawendi, M. G., Direct Probe of Spectral Inhomogeneity Reveals Synthetic Tunability of Single-Nanocrystal Spectral Linewidths. *Nat. Chem.* **2013**, *5*, 602-606.
44. R. Heath, J., Covalency in Semiconductor Quantum Dots. *Chem. Soc. Rev.* **1998**, *27*, 65-71.
45. Peng, X.; Wickham, J.; Alivisatos, A. P., Kinetics of Ii-Vi and Iii-V Colloidal Semiconductor Nanocrystal Growth: "Focusing" of Size Distributions. *J. Am. Chem. Soc.* **1998**, *120*, 5343-5344.
46. Allen, P. M.; Walker, B. J.; Bawendi, M. G., Mechanistic Insights into the Formation of Inp Quantum Dots. *Anew. Chem. Int. Ed.* **2010**, *49*, 760-762.
47. Gary, D. C.; Terban, M. W.; Billinge, S. J. L.; Cossairt, B. M., Two-Step Nucleation and Growth of Inp Quantum Dots Via Magic-Sized Cluster Intermediates. *Chem. Mater.* **2015**, *27*, 1432-1441.
48. Xie, R. P., Xiaogang, Synthetic Scheme for High-Quality Inas Nanocrystals Based on Self-Focusing and One-Pot Synthesis of Inas-Based Core–Shell Nanocrystals. *Anew. Chem. Int. Ed.* **2008**, *47*, 4.
49. Gary, D. C.; Cossairt, B. M., Role of Acid in Precursor Conversion During Inp Quantum Dot Synthesis. *Chem. Mater.* **2013**, *25*, 2463-2469.
50. Cros-Gagneux, A.; Delpech, F.; Nayral, C.; Cornejo, A.; Coppel, Y.; Chaudret, B., Surface Chemistry of Inp Quantum Dots: A Comprehensive Study. *J. Am. Chem. Soc.* **2010**, *132*, 18147-18157.
51. Protiere, M.; Reiss, P., Amine-Induced Growth of an In2o3 Shell on Colloidal Inp Nanocrystals. *Chem. Comm.* **2007**, 2417-2419.

52. Franke, D.; Harris, D. K.; Xie, L.; Jensen, K. F.; Bawendi, M. G., The Unexpected Influence of Precursor Conversion Rate in the Synthesis of Iii–V Quantum Dots. *Angew. Chem.* **2015**, *127*, 14507-14511.
53. Baek, J. Microchemical Systems for the Synthesis of Nanostructures : Quantum Dots. Massachusetts Institute of Technology, Massachusetts Institute of Technology, 2012.
54. Nightingale, A. M. d. M., John. C., Controlled Synthesis of Iii–V Quantum Dots in Microfluidic Reactors. *ChemPhysChem* **2009**, *10*, 3.
55. Baek, J.; Allen, P. M.; Bawendi, M. G.; Jensen, K. F., Investigation of Indium Phosphide Nanocrystal Synthesis Using a High-Temperature and High-Pressure Continuous Flow Microreactor. *Anew. Chem. Int. Ed.* **2011**, *50*, 627-630.
56. Abolhasani, M.; Coley, C. W.; Xie, L.; Chen, O.; Bawendi, M. G.; Jensen, K. F., Oscillatory Microprocessor for Growth and in Situ Characterization of Semiconductor Nanocrystals. *Chem. Mater.* **2015**, *27*, 6131-6138.
57. Virieux, H.; Le Troedec, M.; Cros-Gagneux, A.; Ojo, W.-S.; Delpech, F.; Nayral, C.; Martinez, H.; Chaudret, B., Inp/Zns Nanocrystals: Coupling Nmr and Xps for Fine Surface and Interface Description. *J. Am. Chem. Soc.* **2012**, *134*, 19701-19708.
58. Eichkorn, K.; Ahlrichs, R., Cadmium Selenide Semiconductor Nanocrystals: A Theoretical Study. *Chem. Phys. Lett.* **1998**, *288*, 235-242.
59. Jose, R.; Zhanpeisov, N. U.; Fukumura, H.; Baba, Y.; Ishikawa, M., Structure–Property Correlation of Cdse Clusters Using Experimental Results and First-Principles Dft Calculations. *J. Am. Chem. Soc.* **2006**, *128*, 629-636.
60. Puzder, A.; Williamson, A. J.; Zaitseva, N.; Galli, G.; Manna, L.; Alivisatos, A. P., The Effect of Organic Ligand Binding on the Growth of Cdse Nanoparticles Probed by Ab Initio Calculations. *Nano Lett.* **2004**, *4*, 2361-2365.
61. Manna, L.; Wang; Cingolani, R.; Alivisatos, A. P., First-Principles Modeling of Unpassivated and Surfactant-Passivated Bulk Facets of Wurtzite Cdse: A Model System for Studying the Anisotropic Growth of Cdse Nanocrystals. *J. Phys. Chem. B* **2005**, *109*, 6183-6192.
62. Dengfeng, L.; Zhiguo, W.; Fei, G., First-Principles Study of the Electronic Properties of Wurtzite, Zinc-Blende, and Twinned Inp Nanowires. *Nanotechnology* **2010**, *21*, 505709.
63. Chandiramouli, R., Band Structure and Transport Studies on Inp Nanotube – a First-Principles Investigation. *Superlattices Microstruct.* **2015**, *83*, 193-209.
64. Hybertsen, M. S., Role of Interface Strain in a Lattice-Matched Heterostructure. *Phys. Rev. Lett.* **1990**, *64*, 4.
65. Wood, B. C.; Ogitsu, T.; Schwegler, E., Local Structural Models of Complex Oxygen- and Hydroxyl-Rich Gap/Inp(001) Surfaces. *J. Chem. Phys.* **2012**, *136*, 064705.
66. Wood, B. C.; Schwegler, E.; Choi, W. I.; Ogitsu, T., Hydrogen-Bond Dynamics of Water at the Interface with Inp/Gap(001) and the Implications for Photoelectrochemistry. *J. Am. Chem. Soc.* **2013**, *135*, 15774-15783.
67. Wood, B. C.; Schwegler, E.; Choi, W. I.; Ogitsu, T., Surface Chemistry of Gap(001) and Inp(001) in Contact with Water. *J. Phys. Chem. C* **2014**, *118*, 1062-1070.
68. Talapin, D. V.; Rogach, A. L.; Haase, M.; Weller, H., Evolution of an Ensemble of Nanoparticles in a Colloidal Solution: Theoretical Study. *J. Phys. Chem. B* **2001**, *105*, 12278-12285.
69. Mantzaris, N. V., Liquid-Phase Synthesis of Nanoparticles: Particle Size Distribution Dynamics and Control. *Chem. Eng. Sci.* **2005**, *60*, 4749-4770.

70. Robb, D. T.; Privman, V., Model of Nanocrystal Formation in Solution by Burst Nucleation and Diffusional Growth. *Langmuir* **2008**, *24*, 26-35.
71. Rempel, J. Y.; Bawendi, M. G.; Jensen, K. F., Insights into the Kinetics of Semiconductor Nanocrystal Nucleation and Growth. *J. Am. Chem. Soc.* **2009**, *131*, 4479-4489.
72. Jensen, K. F., Microreaction Engineering — Is Small Better? *Chem. Eng. Sci.* **2001**, *56*, 293-303.
73. Phillips, T. W.; Lignos, I. G.; Maceiczyk, R. M.; deMello, A. J.; deMello, J. C., Nanocrystal Synthesis in Microfluidic Reactors: Where Next? *Lab Chip* **2014**, *14*, 3172-3180.
74. Marre, S.; Jensen, K. F., Synthesis of Micro and Nanostructures in Microfluidic Systems. *Chem. Soc. Rev.* **2010**, *39*, 1183-1202.
75. Chan, E. M.; Mathies, R. A.; Alivisatos, A. P., Size-Controlled Growth of Cdse Nanocrystals in Microfluidic Reactors. *Nano Lett.* **2003**, *3*, 199-201.
76. Yen, B. K. H. G., Axel; Schmidt, Martin A.; Jensen, Klavs F.; Bawendi, Moungi G., A Microfabricated Gas–Liquid Segmented Flow Reactor for High-Temperature Synthesis: The Case of Cdse Quantum Dots. *Angew. Chem.* **2005**, *117*, 5.
77. Nightingale, A. M.; Bannock, J. H.; Krishnadasan, S. H.; O'Mahony, F. T. F.; Haque, S. A.; Sloan, J.; Drury, C.; McIntyre, R.; deMello, J. C., Large-Scale Synthesis of Nanocrystals in a Multichannel Droplet Reactor. *J. Mater. Chem. A* **2013**, *1*, 4067-4076.
78. Lignos, I.; Protesescu, L.; Stavrakis, S.; Piveteau, L.; Speirs, M. J.; Loi, M. A.; Kovalenko, M. V.; deMello, A. J., Facile Droplet-Based Microfluidic Synthesis of Monodisperse Iv–Vi Semiconductor Nanocrystals with Coupled in-Line Nir Fluorescence Detection. *Chem. Mater.* **2014**, *26*, 2975-2982.
79. Nightingale, A. M.; Phillips, T. W.; Bannock, J. H.; de Mello, J. C., Controlled Multistep Synthesis in a Three-Phase Droplet Reactor. *Nat. Commun.* **2014**, *5*.
80. Eckert, C. A.; Knutson, B. L.; Debenedetti, P. G., Supercritical Fluids as Solvents for Chemical and Materials Processing. *Nature* **1996**, *383*, 313-318.
81. Desmoulins-Krawiec, S.; Aymonier, C.; Loppinet-Serani, A.; Weill, F.; Gorsse, S.; Etourneau, J.; Cansell, F., Synthesis of Nanostructured Materials in Supercritical Ammonia: Nitrides, Metals and Oxides. *J. Mater. Chem.* **2004**, *14*, 228-232.
82. Marre, S.; Adamo, A.; Basak, S.; Aymonier, C.; Jensen, K. F., Design and Packaging of Microreactors for High Pressure and High Temperature Applications. *Ind. Eng. Chem. Res.* **2010**, *49*, 11310-11320.
83. Marre, S.; Roig, Y.; Aymonier, C., Supercritical Microfluidics: Opportunities in Flow-through Chemistry and Materials Science. *J. Supercrit. Fluids* **2012**, *66*, 251-264.
84. Marre, S. P., Jongnam; Rempel, Jane; Guan, Juan; Bawendi, Moungi G.; Jensen, Klavs F., Supercritical Continuous-Microflow Synthesis of Narrow Size Distribution Quantum Dots. *Adv. Mater.* **2008**, *20*, 5.
85. Marre, S.; Baek, J.; Park, J.; Bawendi, M. G.; Jensen, K. F., High-Pressure/High-Temperature Microreactors for Nanostructure Synthesis. *J. Assoc. Lab. Autom.* **2009**, *14*, 367-373.
86. Joung, S.; Yoon, S.; Han, C.-S.; Kim, Y.; Jeong, S., Facile Synthesis of Uniform Large-Sized Inp Nanocrystal Quantum Dots Using Tris(Tert-Butyldimethylsilyl)Phosphine. *Nanoscale Res. Lett.* **2012**, *7*, 1-8.
87. Gary, D. C.; Glassy, B. A.; Cossairt, B. M., Investigation of Indium Phosphide Quantum Dot Nucleation and Growth Utilizing Triarylsilylphosphine Precursors. *Chem. Mater.* **2014**, *26*, 1734-1744.

88. Gary, D. C.; Flowers, S. E.; Kaminsky, W.; Petrone, A.; Li, X.; Cossairt, B. M., Single-Crystal and Electronic Structure of a 1.3 Nm Indium Phosphide Nanocluster. *J. Am. Chem. Soc.* **2016**, *138*, 1510-1513.
89. Musiał, M., Coupled-Cluster Theory in Quantum Chemistry. *Rev. Mod. Phys.* **2007**, *79*, 62.
90. Møller, C. P., M. S., Note on an Approximation Treatment for Many-Electron Systems. *Phys. Rev.* **1934**, *46*, 5.
91. Hohenherg, P. K., W., Inhomogeneous Electron Gas. *Phys. Rev.* **1964**, *136*, 8.
92. Kohn, W. S., L. J., Self-Consistent Equations Including Exchange and Correlation Effects. *Phys. Rev.* **1965**, *140*, 6.
93. Perdew, J. P. C., J. A.; Vosko, S. H.; Jackson, Koblar A.; Pederson, Mark R.; Singh, D. J.; Fiolhais, Carlos, Atoms, Molecules, Solids, and Surfaces: Applications of the Generalized Gradient Approximation for Exchange and Correlation. *Phys. Rev. B* **1992**, *46*, 5.
94. Tao, J. P., John P.; Staroverov, Viktor N.; Scuseria, Gustavo E., Climbing the Density Functional Ladder: Nonempirical Meta-Generalized Gradient Approximation Designed for Molecules and Solids. *Phys. Rev. Lett.* **2003**, *91*, 4.
95. Becke, A. D., A New Mixing of Hartree–Fock and Local Density - Functional Theories. *J. Chem. Phys.* **1993**, *98*, 1372-1377.
96. Stephens, P. J.; Devlin, F. J.; Chabalowski, C. F.; Frisch, M. J., Ab Initio Calculation of Vibrational Absorption and Circular Dichroism Spectra Using Density Functional Force Fields. *J. Phys. Chem.* **1994**, *98*, 11623-11627.
97. Lee, C.; Yang, W.; Parr, R. G., Development of the Colle-Salvetti Correlation-Energy Formula into a Functional of the Electron Density. *Phys. Rev. B* **1988**, *37*, 785-789.
98. Becke, A. D., Density - Functional Thermochemistry. Iii. The Role of Exact Exchange. *J. Chem. Phys.* **1993**, *98*, 5648-5652.
99. Feynman, R. P., Forces in Molecules. *Phys. Rev.* **1939**, *56*, 4.
100. Sheppard, D.; Terrell, R.; Henkelman, G., Optimization Methods for Finding Minimum Energy Paths. *J. Chem. Phys.* **2008**, *128*, 134106.
101. E, W. R., Weiqing; Vanden-Eijnden, Eric, String Method for the Study of Rare Events. *Phys. Rev. B* **2002**, *66*, 4.
102. Peters, B.; Heyden, A.; Bell, A. T.; Chakraborty, A., A Growing String Method for Determining Transition States: Comparison to the Nudged Elastic Band and String Methods. *J. Chem. Phys.* **2004**, *120*, 7877-7886.
103. Behn, A.; Zimmerman, P. M.; Bell, A. T.; Head-Gordon, M., Efficient Exploration of Reaction Paths Via a Freezing String Method. *J. Chem. Phys.* **2011**, *135*, 224108.
104. Baker, J., An Algorithm for the Location of Transition States. *J. Comput. Chem.* **1986**, *7*, 11.
105. Henkelman, G.; Jónsson, H., A Dimer Method for Finding Saddle Points on High Dimensional Potential Surfaces Using Only First Derivatives. *J. Chem. Phys.* **1999**, *111*, 7010-7022.
106. Heyden, A.; Bell, A. T.; Keil, F. J., Efficient Methods for Finding Transition States in Chemical Reactions: Comparison of Improved Dimer Method and Partitioned Rational Function Optimization Method. *J. Chem. Phys.* **2005**, *123*, 224101.
107. Xie, L.; Zhao, Q.; Jensen, K. F.; Kulik, H. J., Direct Observation of Early-Stage Quantum Dot Growth Mechanisms with High-Temperature Ab Initio Molecular Dynamics. *J. Phys. Chem. C* **2016**, *120*, 2472-2483.

108. Raty, J.-Y.; Gygi, F.; Galli, G., Growth of Carbon Nanotubes on Metal Nanoparticles: A Microscopic Mechanism from Ab Initio Molecular Dynamics Simulations. *Phys. Rev. Lett.* **2005**, *95*, 096103.
109. Oguri, T.; Shimamura, K.; Shibuta, Y.; Shimojo, F.; Yamaguchi, S., Ab Initio Molecular Dynamics Simulation of the Dissociation of Ethanol on a Nickel Cluster: Understanding the Initial Stage of Metal-Catalyzed Growth of Carbon Nanotubes. *J. Phys. Chem. C* **2013**, *117*, 9983-9990.
110. Arifin, R.; Shibuta, Y.; Shimamura, K.; Shimojo, F.; Yamaguchi, S., Ab Initio Molecular Dynamics Simulation of Ethylene Reaction on Nickel (111) Surface. *J. Phys. Chem. C* **2015**, *119*, 3210-3216.
111. Wang, Y.-G.; Mei, D.; Glezakou, V.-A.; Li, J.; Rousseau, R., Dynamic Formation of Single-Atom Catalytic Active Sites on Ceria-Supported Gold Nanoparticles. *Nat. Comm.* **2015**, *6*, 6511.
112. Mattioli, G.; Giannozzi, P.; Amore Bonapasta, A.; Guidoni, L., Reaction Pathways for Oxygen Evolution Promoted by Cobalt Catalyst. *J. Am. Chem. Soc.* **2013**, *135*, 15353-15363.
113. Sterpone, F.; Bonella, S.; Meloni, S., Early Stage of the Dehydrogenation of Naalh4 by Ab Initio Rare Event Simulations. *J. Phys. Chem. C* **2012**, *116*, 19636-19643.
114. Buin, A.; Comin, R.; Ip, A. H.; Sargent, E. H., Perovskite Quantum Dots Modeled Using Ab Initio and Replica Exchange Molecular Dynamics. *J. Phys. Chem. C* **2015**, *119*, 13965-13971.
115. Alnemrat, S.; Hooper, J. P., Ab Initio Metadynamics Simulations of Oxygen/Ligand Interactions in Organoaluminum Clusters. *J. Chem. Phys.* **2014**, *141*, 144304.
116. Raymand, D.; Jacobsson, T. J.; Hermansson, K.; Edvinsson, T., Investigation of Vibrational Modes and Phonon Density of States in Zno Quantum Dots. *J. Phys. Chem. C* **2012**, *116*, 6893-6901.
117. Azpiroz, J. M.; Lopez, X.; Ugalde, J. M.; Infante, I., Modeling Surface Passivation of Zns Quantum Dots. *J. Phys. Chem. C* **2012**, *116*, 2740-2750.
118. Wang, L.-P.; Titov, A.; McGibbon, R.; Liu, F.; Pande, V. S.; Martínez, T. J., Discovering Chemistry with an Ab Initio Nanoreactor. *Nat. Chem.* **2014**, *6*, 1044-1048.
119. Ufimtsev, I. S.; Martinez, T. J., Quantum Chemistry on Graphical Processing Units. 3. Analytical Energy Gradients, Geometry Optimization, and First Principles Molecular Dynamics. *J. Chem. Theory Comput.* **2009**, *5*, 2619-2628.
120. Petachem. http://www.petachem.com (accessed Jul. 27, 2015).
121. Martínez, J. M.; Martínez, L., Packing Optimization for Automated Generation of Complex System's Initial Configurations for Molecular Dynamics and Docking. *J. Comput. Chem.* **2003**, *24*, 819-825.
122. Martínez, L.; Andrade, R.; Birgin, E. G.; Martínez, J. M., Packmol: A Package for Building Initial Configurations for Molecular Dynamics Simulations. *J. Comput. Chem.* **2009**, *30*, 2157-2164.
123. Binkley, J. S.; Pople, J. A.; Hehre, W. J., Self-Consistent Molecular-Orbital Methods .21. Small Split-Valence Basis-Sets for 1st-Row Elements. *J. Am. Chem. Soc.* **1980**, *102*, 939-947.
124. Pyykkö, P.; Atsumi, M., Molecular Single-Bond Covalent Radii for Elements 1–118. *Chem. Eur. J.* **2009**, *15*, 186-197.
125. Vosko, S. H.; Wilk, L.; Nusair, M., Accurate Spin-Dependent Electron Liquid Correlation Energies for Local Spin Density Calculations: A Critical Analysis. *Can. J. Phys.* **1980**, *58*, 1200-1211.

126. Kästner, J.; Carr, J. M.; Keal, T. W.; Thiel, W.; Wander, A.; Sherwood, P., Dl-Find: An Open-Source Geometry Optimizer for Atomistic Simulations†. *J. Phys. Chem. A* **2009**, *113*, 11856-11865.
127. NBO6.0., E. D. Glendening, J, K. Badenhoop, A. E. Reed, J. E. Carpenter, J. A. Bohmann, C. M. Morales, C. R. Landis, and F. Weinhold, Theoretical Chemistry Institute, University of Wisconsin, Madison. 2013.
128. Shao, Y., et al., Advances in Methods and Algorithms in a Modern Quantum Chemistry Program Package. *Phys. Chem. Chem. Phys.* **2006**, *8*, 3172-3191.
129. Behn, A.; Zimmerman, P. M.; Bell, A. T.; Head-Gordon, M., Efficient Exploration of Reaction Paths Via a Freezing String Method. *J. Chem. Phys.* **2011**, *135*, 224108.
130. Lange, A. W.; Herbert, J. M., A Smooth, Nonsingular, and Faithful Discretization Scheme for Polarizable Continuum Models: The Switching/Gaussian Approach. *J. Chem. Phys.* **2010**, *133*, 244111.
131. Lange, A. W.; Herbert, J. M., The Polarizable Continuum Model for Molecular Electrostatics: Basic Theory, Recent Advances, and Future Challenges. In *Many-Body Effects and Electrostatics in Multi-Scale Computations of Biomolecules*, Q. Cui, P. R., and M. Meuwly, Ed. 2014.
132. Boys, S. F.; Bernardi, F. d., The Calculation of Small Molecular Interactions by the Differences of Separate Total Energies. Some Procedures with Reduced Errors. *Mol. Phys.* **1970**, *19*, 553-566.
133. Xie, L.; Harris, D. K.; Bawendi, M. G.; Jensen, K. F., Effect of Trace Water on the Growth of Indium Phosphide Quantum Dots. *Chem. Mater.* **2015**, *27*, 5058-5063.
134. Xie, R.; Li, Z.; Peng, X., Nucleation Kinetics Vs Chemical Kinetics in the Initial Formation of Semiconductor Nanocrystals. *J. Am. Chem. Soc.* **2009**, *131*, 15457-15466.
135. Mordvinova, N.; Vinokurov, A.; Dorofeev, S.; Kuznetsova, T.; Znamenkov, K., Phosphine Synthetic Route Features and Postsynthetic Treatment of Inp Quantum Dots. *J. Alloys Compd.* **2014**, *582*, 43-49.
136. Margraf, J. T.; Ruland, A.; Sgobba, V.; Guldi, D. M.; Clark, T., Theoretical and Experimental Insights into the Surface Chemistry of Semiconductor Quantum Dots. *Langmuir* **2013**, *29*, 15450-15456.
137. Zherebetskyy, D.; Scheele, M.; Zhang, Y.; Bronstein, N.; Thompson, C.; Britt, D.; Salmeron, M.; Alivisatos, P.; Wang, L.-W., Hydroxylation of the Surface of Pbs Nanocrystals Passivated with Oleic Acid. *Science* **2014**, *344*, 1380-1384.
138. Allen, L. C., Electronegativity Is the Average One-Electron Energy of the Valence-Shell Electrons in Ground-State Free Atoms. *J. Am. Chem. Soc.* **1989**, *111*, 9003-9014.
139. Zhao, Q.; Xie, L.; Kulik, H. J., Discovering Amorphous Indium Phosphide Nanostructures with High-Temperature Ab Initio Molecular Dynamics. *J. Phys. Chem. C* **2015**, *119*, 23238-23249.
140. *Handbook Series on Semiconductor Parameters*; World Scientific, 1996; Vol. 1.
141. Glassy, B. A.; Cossairt, B. M., Ternary Synthesis of Colloidal Zn3p2 Quantum Dots. *Chem. Comm.* **2015**, *51*, 5283-5286.
142. Jasieniak, J.; Smith, L.; Embden, J. v.; Mulvaney, P.; Califano, M., Re-Examination of the Size-Dependent Absorption Properties of Cdse Quantum Dots. *J. Phys. Chem. C* **2009**, *113*, 19468-19474.
143. Leatherdale, C. A.; Woo, W. K.; Mikulec, F. V.; Bawendi, M. G., On the Absorption Cross Section of Cdse Nanocrystal Quantum Dots. *J. Phy. Chem. B* **2002**, *106*, 7619-7622.

144. Yu, W. W.; Qu, L.; Guo, W.; Peng, X., Experimental Determination of the Extinction Coefficient of Cdte, Cdse, and Cds Nanocrystals. *Chem. Mater.* **2003**, *15*, 2854-2860.
145. Levi-Kalisman, Y.; Jadzinsky, P. D.; Kalisman, N.; Tsunoyama, H.; Tsukuda, T.; Bushnell, D. A.; Kornberg, R. D., Synthesis and Characterization of Au102(P-Mba)44 Nanoparticles. *J. Am. Chem. Soc.* **2011**, *133*, 2976-2982.
146. Dass, A.; Stevenson, A.; Dubay, G. R.; Tracy, J. B.; Murray, R. W., Nanoparticle Maldi-Tof Mass Spectrometry without Fragmentation: Au25(Sch2ch2ph)18 and Mixed Monolayer Au25(Sch2ch2ph)18−X(L)X. *J. Am. Chem. Soc.* **2008**, *130*, 5940-5946.
147. Guan, B.; Lu, W.; Fang, J.; Cole, R. B., Characterization of Synthesized Titanium Oxide Nanoclusters by Maldi-Tof Mass Spectrometry. *J. Am. Soc. Mass Spec.* **2007**, *18*, 517-524.
148. Kim, B. H., et al., Sizing by Weighing: Characterizing Sizes of Ultrasmall-Sized Iron Oxide Nanocrystals Using Maldi-Tof Mass Spectrometry. *J. Am. Chem. Soc.* **2013**, *135*, 2407-2410.
149. Khitrov, G. A.; Strouse, G. F., Zns Nanomaterial Characterization by Maldi-Tof Mass Spectrometry. *J. Am. Chem. Soc.* **2003**, *125*, 10465-10469.
150. Aboulaich, A.; Billaud, D.; Abyan, M.; Balan, L.; Gaumet, J.-J.; Medjadhi, G.; Ghanbaja, J.; Schneider, R., One-Pot Noninjection Route to Cds Quantum Dots Via Hydrothermal Synthesis. *ACS Appl. Mater. Interfaces* **2012**, *4*, 2561-2569.
151. Li, J.; Yang, T.; Chan, W. H.; Choi, M. M. F.; Zhao, D., Synthesis of High-Quality N-Acetyl-L-Cysteine-Capped Cdte Quantum Dots by Hydrothermal Route and the Characterization through Maldi-Tof Mass Spectrometry. *J. Phys. Chem. C* **2013**, *117*, 19175-19181.
152. Wang, F.; Richards, V. N.; Shields, S. P.; Buhro, W. E., Kinetics and Mechanisms of Aggregative Nanocrystal Growth. *Chem. Mater.* **2014**, *26*, 5-21.
153. Lee, J.; Yang, J.; Kwon, S. G.; Hyeon, T., Nonclassical Nucleation and Growth of Inorganic Nanoparticles. *Nature Reviews Materials* **2016**, *1*, 16034.
154. Morris-Cohen, A. J.; Donakowski, M. D.; Knowles, K. E.; Weiss, E. A., The Effect of a Common Purification Procedure on the Chemical Composition of the Surfaces of Cdse Quantum Dots Synthesized with Trioctylphosphine Oxide. *J. Phys. Chem. C* **2010**, *114*, 897-906.
155. Shakeri, B.; Meulenberg, R. W., A Closer Look into the Traditional Purification Process of Cdse Semiconductor Quantum Dots. *Langmuir* **2015**, *31*, 13433-13440.
156. Anderson, N. C.; Hendricks, M. P.; Choi, J. J.; Owen, J. S., Ligand Exchange and the Stoichiometry of Metal Chalcogenide Nanocrystals: Spectroscopic Observation of Facile Metal-Carboxylate Displacement and Binding. *J. Am. Chem. Soc.* **2013**, *135*, 18536-18548.
157. Shen, Y.; Roberge, A.; Tan, R.; Gee, M. Y.; Gary, D.; Huang, Y.; Blom, D. A.; Benicewicz, B.; Cossairt, B.; Greytak, A., Gel Permeation Chromatography as a Multifunctional Processor for Nanocrystal Purification and on-Column Ligand Exchange Chemistry. *Chem. Sci.* **2016**, *Just Accepted.*
158. Shen, Y.; Gee, M. Y.; Tan, R.; Pellechia, P. J.; Greytak, A. B., Purification of Quantum Dots by Gel Permeation Chromatography and the Effect of Excess Ligands on Shell Growth and Ligand Exchange. *Chem. Mater.* **2013**, *25*, 2838-2848.
159. Hens, Z.; Martins, J. C., A Solution Nmr Toolbox for Characterizing the Surface Chemistry of Colloidal Nanocrystals. *Chem. Mater.* **2013**, *25*, 1211-1221.
160. Wang, Y. L., Yi-Hsin; Zhang, Ying; Wang, Fudong; Kowalski, Paul J.; Rohrs, Henry W.; Loomis, Richard A.; Gross, Michael L.; Buhro, William E., Isolation of the Magic-Size Cdse Nanoclusters [(Cdse)13(N-Octylamine)13] and [(Cdse)13(Oleylamine)13]. *Angew. Chem. Int. Ed.* **2012**, *51*, 4.

161. Beecher, A. N.; Yang, X.; Palmer, J. H.; LaGrassa, A. L.; Juhas, P.; Billinge, S. J. L.; Owen, J. S., Atomic Structures and Gram Scale Synthesis of Three Tetrahedral Quantum Dots. *J. Am. Chem. Soc.* **2014**, *136*, 10645-10653.
162. Narayanaswamy, A.; Xu, H.; Pradhan, N.; Kim, M.; Peng, X., Formation of Nearly Monodisperse In2o3 Nanodots and Oriented-Attached Nanoflowers: Hydrolysis and Alcoholysis Vs Pyrolysis. *J. Am. Chem. Soc.* **2006**, *128*, 10310-10319.
163. Senftle, T. P., et al., The Reaxff Reactive Force-Field: Development, Applications and Future Directions. *npj Comput. Mater.* **2016**, *2*, 15011.
164. http://webbook.nist.gov/chemistry/fluid/.
165. Fontes, N.; Partridge, J.; Halling, P. J.; Barreiros, S., Zeolite Molecular Sieves Have Dramatic Acid–Base Effects on Enzymes in Nonaqueous Media. *Biotechnol. Bioeng.* **2002**, *77*, 296-305.
166. Aspnes, D. E.; Studna, A. A., Dielectric Functions and Optical Parameters of Si, Ge, Gap, Gaas, Gasb, Inp, Inas, and Insb from 1.5 to 6.0 Ev. *Phys. Rev. B* **1983**, *27*, 985-1009.
167. Garcia-Rodriguez, R.; Liu, H., Solution Structure of Cadmium Carboxylate and Its Implications for the Synthesis of Cadmium Chalcogenide Nanocrystals. *Chem. Comm.* **2013**, *49*, 7857-7859.